Dissertation zur Erlangung des Doktorgrades
der Fakultät für Chemie und Pharmazie
der Ludwig–Maximilians–Universität München

Confocal and Antenna-Enhanced Microscopy and Spectroscopy of Graphene

von
Nicolás Coca López
aus
Madrid (Spanien)
2018

Dissertation zur Erlangung des Doktorgrades
der Fakultät für Chemie und Pharmazie
der Ludwig–Maximilians–Universität München

Confocal and Antenna-Enhanced Microscopy and Spectroscopy of Graphene

von
Nicolás Coca López
aus
Madrid (Spanien)
2018

Erklärung

Diese Dissertation wurde im Sinne von §7 der Promotionsordnung vom 28. November 2011 von Herrn Prof. Dr. Achim Hartschuh betreut.

Eidesstattliche Versicherung

Diese Dissertation wurde eigenständig und ohne unerlaubte Hilfe erarbeitet.

München, den 13. April 2018

.....
(Nicolás Coca López)

Dissertation eingereicht am: 16.04.2018
Erstgutachter: Prof. Dr. Achim Hartschuh
Zweitgutachter: Prof. Dr. Tim Liedl
Mündliche Prüfung am: 14.05.2018

To my family and friends,

Abstract

In the course of this thesis, confocal and antenna-enhanced spectroscopy and microscopy were employed for the study of graphene and graphene-based photodetectors. This work is divided in three parts: (i) the study of the angular radiation patterns of the G and 2D Raman scattering from graphene on glass, unveiling its point-dipolar emission nature. (ii) Simultaneous subdiffraction photocurrent, Raman scattering, and topographical tip-enhanced near-field microscopy (TENOM) studies of graphene-based photodetectors on glass. (iii) The demonstration of remote excitation and detection of surface-enhanced Raman scattering (SERS) from graphene using a silver nanowire (NW) as plasmonic waveguide.

In the first part, spectrally selective back focal plane (BFP) imaging, a Fourier space technique enabling the quantification of the angular distribution of light emitted or scattered by nanoscale objects, is applied to the study of Raman scattering from graphene on glass. Comparison between experimental and calculated Raman scattering BFP patterns showed that the G and 2D Raman band emission can be described by a superposition of two and three incoherent point dipoles oriented in the graphene plane. While the G scattering is confirmed to be nonpolarized, in the case of the 2D band, polarized scattering is observed. The polarization contrast is found to decrease substantially for increasing collection angle, due to polarization mixing caused by the air-dielectric interface. This also influences the 2D to G intensities ratio, I(2D)/I(G), a crucial quantity for estimating the doping in graphene.

In the second part, TENOM, a scanning probe technique which exploits the local field enhancement at the apex of a metallic tip to form high-resolution images of surfaces by raster scanning it, is applied to the study of graphene-based photodetectors on glass. The combination of TENOM with scanning photocurrent microscopy (SPCM) enabled the characterization of a graphene-based photodetector on glass with a spatial resolution of about 25 nm. In the case of the photocurrent signal, the near-field contribution allowed to observe a steeper slope at the electrodes edges, as well as several subdiffraction modulations in both photocurrent and Raman signals.

The third part is dedicated to the study of remote SERS. For the case of a nanowire completely covering the Raman scatterer, remote SERS is found to have two contributions: Remote excitation and detection. The remote excitation of SERS from graphene by propagating surface plasmon polaritons (SPPs) launched by a focused laser over distances on the order of 10 μm is shown by investigating a nanowire touching a graphene sheet only with one of its terminals. Remote detection of SERS is then demonstrated for the same nanowire by detecting light emission at the distal end of the nanowire that was launched by graphene Raman scattering and carried to the end of the nanowire by SPPs. Spatio-spectral imaging investigations showed these two contributions to be of comparable intensities. The transfer of the excitation and Raman scattered light along the nanowire can also be visualized through spectrally selective BFP imaging. BFP images detected upon focused laser excitation at one of the nanowire's tips reveal propagating SPPs at the

laser energy and at the energies of the most prominent Raman bands of graphene. With this approach the identification of remote excitation and detection of SERS for nanowires completely covering the Raman scatterer is achieved, which is typically not possible by direct imaging.

Contents

Chapter 1

Introduction

The field of plasmonics has seen rapid growth in both basic research and application over the last two decades [1] and is becoming of great interest to a wide spectrum of scientists in many different fields, ranging from physics, chemistry and materials science to biology and medicine [2, 3]. This device technology exploits the unique optical properties of surface plasmons (SPs), the collective oscillating modes of the conduction electrons at metal/dielectric interfaces, to manipulate and route light at the nanoscale [4, 5]. SPs are often separated into two categories: (i) propagating surface-plasmon polaritons (SPPs), in which the coherent electron oscillation propagates as a bound longitudinal wave along the metal surface and (ii) localized surface plasmons (LSP), in which the electrons coherently oscillate locally within a metallic nanostructure.

As an application example, propagating SPPs have the potential to play a unique and important role in enhancing the processing speed of future integrated circuits [6]. While the semiconductor industry has performed an incredible job in scaling electronic devices to nanoscale dimensions, interconnect delay time issues provide significant challenges toward the realization of purely electronic circuits operating above 10 GHz. On a different note, photonic devices possess an enormous data-carrying capacity, but unfortunately, dielectric photonic components are limited in their size by the laws of diffraction, preventing the same scaling as in electronics. Presenting the size of electronics and the speed of photonics, plasmonic devices might interface naturally with similar speed photonic devices and similar size electronic components, serving as the missing link between these two fields [7].

Some of the most acknowledged applications of the second category are in surface-enhanced Raman scattering (SERS) [8] and tip-enhanced near-field optical microscopy (TENOM) [9], for which the electromagnetic field enhancement by LSPs is the dominating contribution to the signal enhancement [10]. SERS is performed in-situ at noble metal surfaces or metallic nanoparticle aggregates, with signal enhancements of up to 10^{11} which enable the detection of Raman spectra at the single molecule level [11, 12, 13]. TENOM is a scanning probe technique which exploits the local field enhancement obtained in SERS to form high-resolution images of surfaces by raster scanning a metallic tip [14].

A remarkable application combining both localized and propagating SPs employs nanowires for the remote excitation and detection of SERS [15]. Metallic nanowires (NWs)

supporting propagating SPPs can function as waveguides to allow light guiding with field confinement beyond the diffraction limit of light [16]. This enables the excitation of a Raman scatterer positioned at one end of a metallic nanowire by the propagating SPPs generated by focused laser illumination at the other end of the nanowire [17, 18]. Conversely, Raman scattered light generated by local excitation in the vicinity of the nanowire's tip can also couple to propagating plasmonic modes and be detected at the remote terminal of a nanowire [19]. In both cases, the excitation and the coupling of Raman scattering to the NW can be expected to be enhanced by the NW's tips near-field generated by LSPs. This approach has already shown its practicability for remote excitation of surface catalytic reactions [20, 21, 22] and Raman detection of biomolecules in-vivo in cells [23, 24].

A model system to test the plasmonic applications just mentioned is, therefore, on demand. Graphene is a very popular, versatile and deeply studied nanomaterial very well suited for this task. This carbon allotrope, consisting of a single layer of carbon atoms arranged in an hexagonal lattice, has many unusual properties: It is the strongest material ever tested, efficiently conducts heat and electricity, and is nearly transparent. Its applications range from nanophotonics to thin-film transistors and optoelectronics, and it will potentially play an important role in technologies such as energy storage, wearable technology, electric sports cars, and lightweight planes.

1.1 Synopsis of the thesis

This work is dedicated to the investigation of how optical antennas, benefiting from plasmonic properties, can be used for microscopy and spectroscopy studies on graphene and graphene-based devices.

The thesis is structured as follows. After this introduction, chapter 2 discusses the basics of back focal plane (BFP) imaging. BFP imaging allows to quantify the angular distribution of light emitted or scattered by nanoscale objects, and it is specially suited for determining the orientation of dipolar emitters as well as to image the change of the radiation patterns in emitters/scatterers induced by optical antennas. The chapter begins with the description of the image formation process in the BFP of a microscope objective. It continues with the calculation of the radiation patterns from point-dipole emitters. The detection efficiency and the polarization contrast are then discussed in terms of the numerical aperture. Finally, the experimental setup used during the scope of this work is introduced.

Chapter 3 introduces the basic knowledge about Raman scattering in graphene. The angular distribution of the G and 2D Raman scattering from graphene on glass by detecting back focal plane patterns are reported. The G Raman emission can be described by a superposition of two incoherent orthogonal point dipoles oriented in the graphene plane. Due to double resonant Raman scattering, the 2D emission can be represented by the sum of either three incoherent dipoles oriented 120° with respect to each other, or two orthogonal incoherent ones with a 3:1 weight ratio. Phenomenological Raman tensors supporting this

fact are then introduced. Basic experiments on the polarization dependency of Raman scattering in graphene performed by Yoon and coworkers are verified, which confirms the validity of the proposed Raman tensors. This chapter also serves as a starting point to understand how the angular emission of Raman scattering in graphene will be redistributed by silver nanowires in chapter 6.

In chapter 4, the physical principle of optical antennas used in TENOM is first illustrated. Optical antennas are a powerful tool for manipulating light at the nanometer scale, while also providing efficient control of transduction in the far-field. The main concepts of optical antennas and the signal enhancement they provide for different processes such as Raman scattering, photoluminescence, photocurrent and electroluminescence are discussed. Metallic optical antennas can strongly benefit from plasmonic properties in the optical regime. Therefore, the chapter continues with the discussion of the fundamentals of plasmonics. Plasmonics is concerned primarily with the manipulation of light at the nanoscale, exploiting both localized SPs and propagating SPPs for sensing and waveguiding applications. In this section the fundamental properties of SPPs, their typical lengths, their dispersion relation and how can they be excited are presented. Also an introduction to LSPs and how they increase the absorption and scattering cross sections in metallic nanoparticles is provided. The chapter concludes with two examples of angular radiation pattern modification by two different plasmonic systems: silver nanowires supporting propagating SPPs and gold dimers supporting localized SPs.

Chapter 5 deals with graphene-based photodetectors, a great promise for a wide variety of applications. After an explanation on how to implement TENOM measurements in a typical confocal microscope setup, scanning photocurrent microscopy (SPCM), a popular tool used for the investigation of graphene devices as light detectors, is introduced. Typical confocal SPCM measurement on metal-graphene-metal photodetectors, the simplest class of graphene-based photodetectors, are shown. Tip-enhanced photocurrent and tip-enhanced Raman microscopy measurements enable the characterization of such devices at the nanoscale with a spatial resolution of about 25 nm. In the case of the photocurrent signal, the near-field contribution allows to observe a steeper slope at the electrode edges, as well as several subdiffraction modulations in both photocurrent and Raman signals. The chapter finishes with the proposition of using a technique based on near-field to far-field separation via tip-sample distance modulation, which promises to increase the image contrast in order to find correlations between Raman scattering, topography and photocurrent signals.

The experimental demonstration of the remote excitation and detection of SERS from graphene using a silver nanowire as plasmonic waveguide is shown in chapter 6. First, the remote excitation of SERS from graphene by propagating SPPs launched by a focused laser over distances on the order of 10 nm, is shown by investigating a nanowire touching a graphene sheet only with one of its terminal. Remote detection of SERS is then demonstrated for the same nanowire by detecting light emission at the distal end of the nanowire that was launched by graphene Raman scattering and carried to the end of the nanowire

by SPPs. The transfer of the excitation and Raman scattered light along the nanowire can also be visualized through spectrally selective back focal plane imaging. Back focal plane images detected upon focused laser excitation at one of the nanowire's tips reveal propagating SPPs at the laser energy and at the energies of the most prominent Raman bands of graphene. With this approach, the identification of remote excitation and detection of SERS for nanowires completely covering the Raman scatterer is achieved, which is typically not possible by direct imaging.

Chapter 2

Back focal plane (BFP) imaging: Where does the light go?

In optical microscopy, a microscope objective allows to determine information related to the position, size and emission wavelength of the investigated object with a resolution down to the diffraction limit of light. Furthermore, it is also possible to extract information in which angles the light from the object is emitted or scattered through this objective. This can be achieved by observing the Fourier plane of the imaging lens with a method called BFP imaging [25], in which radiation patterns are recorded [26]. BFP imaging allows to quantify the angular distribution of light emitted or scattered by nanoscale objects. It can be used to determine the orientation of dipolar emitters [27], and therefore to model the photoluminescence [28] and Raman scattering [29] from two dimensional materials, as well as to image the change of the radiation patterns in emitters/scatterers induced by optical antennas [30, 31, 32, 33, 34]. BFP imaging is particularly useful for observing SPPs that render characteristic patterns indicating the direction of SPP propagation and the SPP momentum [35, 36].The distribution of radiation in the BFP can also be used in the context of ellipsometry [37] and nanoscopic position sensing [38].

It should be noted that the nomenclature is not uniform across the literature, and sometimes what was introduced here as BFP imaging can be referred as Fourier space imaging, angular radiation pattern imaging, etc.

This chapter starts with the description of the image formation in the BFP in section 2.1, followed by the discussion of the typical patterns generated by point-dipolar emission in section 2.2. The detection efficiency and the polarization contrast are then discussed in terms of the numerical aperture in sections 2.3 and 2.4. Finally, the experimental setup used during the scope of this work is introduced in section 2.5.

2.1 Theoretical Description of Radiation Patterns in the BFP

The radiation generated by an emitter in a uniform medium depends only on the emitter properties, while the surrounding medium does not modify them. Therefore, the medium does not influence the angular distribution of the radiation and the radiation of a point-dipole in a uniform medium can be seen as the emission of a dipole in free space. The radiation pattern of a dipole in free space is radially symmetric with respect to the axis parallel to the dipole moment $\vec{p}$, with the highest intensity emitted into angles perpendicular to the dipole axis, following a $\sin^2\theta$ distribution, where θ is the angle between the dipole axis and the observation direction [39].

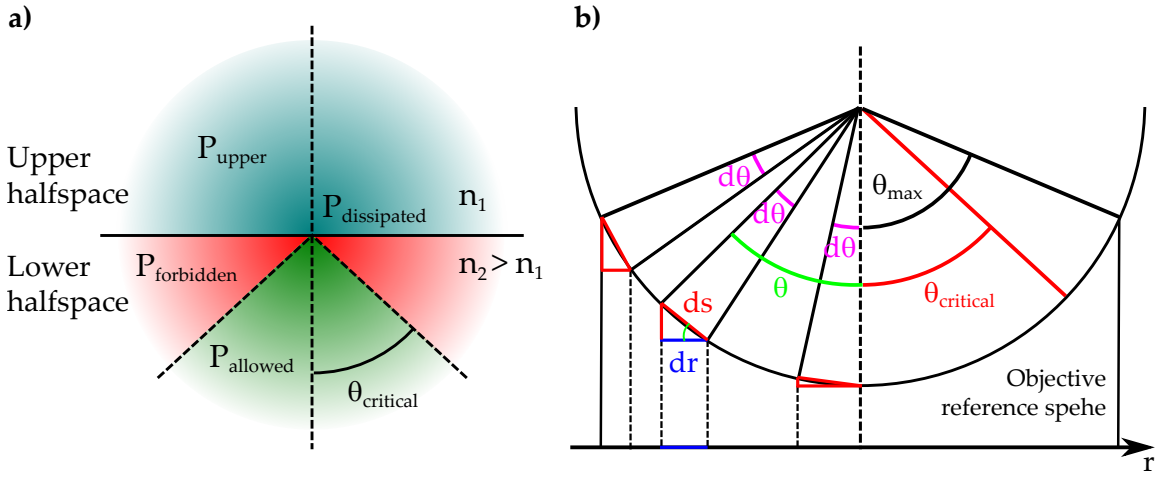

Figure 2.1: (a) Scheme of radiated power by an emitter on the interface between two dielectric media n_1 and n_2 with $n_1 < n_2$. The fractions of the total emitted power (P_{total}) which does not dissipate into the surface ($P_{dissipated}$) radiate into the upper half-space (P_{upper}), the allowed zone ($P_{allowed}$) for $\theta < \theta_{critical}$, or the forbidden zone ($P_{forbidden}$) for $\theta > \theta_{critical}$. Figure adapted from references 40 and 41. (b) Illustration of the projection of the angular emission in the allowed zone by an imaging lens onto its BFP. The maximal collection angle of the lens and the critical angle are also indicated. Figure adapted from reference 41.

However, the fractions of radiation emitting into different angular regions are different when the emitter is placed on a dielectric substrate of refractive index n_2 surrounded by a dielectric medium with $n_1 < n_2$. As sketchet in Figure 2.1(a), the overall radiated power P_{total} can be divided into emission into the upper half-space P_{upper}, the allowed zone $P_{allowed}$ for angles smaller than the critical angle $\theta_{critical} = \arcsin(n_1/n_2)$, the forbidden zone of the lower half-space $P_{forbidden}$ for angles larger than $\theta_{critical}$, and power dissipated into the surface $P_{dissipated}$, as $P_{total} = P_{upper} + P_{allowed} + P_{forbidden} + P_{dissipated}$ [42]. Allowed and forbidden zones are defined depending on the critical angle $\theta_{critical}$. Emission with an angle

$\theta < \theta_{critical}$ goes into the allowed zone, while radiated power fulfilling the condition for total internal reflection $\theta > \theta_{critical}$ goes into the forbidden zone. This model corresponds to the geometry of a typical inverted microscope with an oil-inmersion objective, as the one used during this thesis (see section 2.5). The emitter, situated on a microscope cover glass, is placed into the focus of a high NA oil immersion objective. Therefore, the light emitted into the lower half-space medium in the allowed zone $P_{allowed}$ and parts of the forbidden zone $P_{forbidden}$ can be collected by the objective. For the calculation of the intensity distribution in the BFP of an objective as a function of the emission angle θ, the Weyl representation can be applied. In this representation, the spherical wave launched by the emitter is decomposed into planar and evanescent waves [43]. Thus, the intensity distribution in the back focal plane of the microscope objective is related to the fields generated by the emitter $\vec{E}_{emitter}$:

$$I_{BFP} \propto \frac{1}{\cos\theta} |\vec{E}_{emitter}|^2 \tag{2.1}$$

Figure 2.1 (b) illustrates the projection of the emission onto the BFP of the microscope objective. Since the same angle $d\theta$ always corresponds to the same arc ds (knowing that $s = R \cdot \theta$), the same amount of power radiating from the emitter along each equally sized angular section $d\theta$ is addressed on ds. From the combination of this with the trigonometric relation $dr = ds\cos\theta$ inferred from the sketch, it follows that for increasing angles θ, equal amounts of power are projected onto a decreasing section dr. In order to correct for this, the apodization factor $1/\cos\theta$ is included in the formula, ensuring the conservation of energy [44]. The sketch also shows a maximum collection angle θ_{max}, which is given by the NA of the objective ($\theta_{max} = \arcsin(NA/n)$).

2.2 Calculation of point-dipolar radiation intensity distribution in the BFP

The radiation pattern of a dipole in free space is characterized by a $\sin^2\theta$, where θ is the angle between the dipole axis and the observation direction [39]. However, most experiments are performed near the dielectric interfaces, where the photons emitted by the dipole can scatter, altering the emission pattern of the emitter. This situation was theoretically approached already at the beginning of the twentieth century by Sommerfeld, Hoerschelmann and Weyl [45, 46, 47, 43]. The predictions were confirmed experimentally in 1984 for an ensemble of molecules by Fattinger and Lukosz [48]. In 2003 Lieb and coworkers showed that the orientation of the emission dipole is directly encoded in the spatial distribution of the emitted light and that it is possible to uniquely reconstruct the emission-dipole moment from a dipole's emission pattern. In the following, the calculation of radiation patterns formulated by Lieb et al., giving way to BFP pattern simulation are introduced.

The geometry of the model and the involved parameters for the theoretical calculation are shown in Figure 2.2 as published by Lieb et al. A point-dipole emitter $\vec{p}$ is considered to be placed on the surface of a glass substrate (coverslip) with an orientation given by

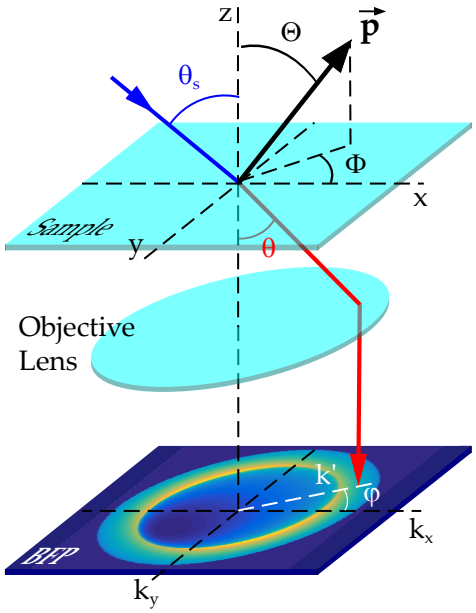

Figure 2.2: Scheme of the geometry used for the calculation of the back focal plane patterns from a emitter laying on an interface. Radiation emitted at θ from a dipole $\vec{p}$ oriented with angles Φ and Θ will be detected at position (k', ψ) in the Fourier space. Adapted from reference 41.

the angles Φ and Θ. θ_S denotes the incident angle complementary to the emission angle θ according to Snell's law:

$$\theta_S = arcsin\left(\frac{n_2 sin\theta}{n_1}\right) \tag{2.2}$$

Where complex values of the incident angle θ_S are allowed. The intensity collected for $\theta > \theta_{critical}$ originates from the conversion of the dipole's near field into propagating fields in the substrate [49]. After collection of the emitted light by the objective lens, the ray is projected onto its BFP. Its position in the BFP is described by the azimuthal angle ψ and the momentum k'. The relation between emission angle θ and the k-vector coordinate system in the BFP is related by:

$$|k'| = 2\,\pi\,\frac{n_2}{\lambda}\sin\theta = k_0\,n_2\sin\theta, \tag{2.3}$$

$$\begin{pmatrix} k'_x \\ k'_y \end{pmatrix} = \begin{pmatrix} \cos\psi \\ \sin\psi \end{pmatrix} \cdot |k'| \tag{2.4}$$

Following formula 2.1, the intensity distribution of a single dipole in the BFP can be given by:

$$I_{dipole}(\theta, \psi) \propto \frac{1}{\cos\theta}\left(E_p E_p^* + E_s E_s^*\right), \tag{2.5}$$

Where E_p and E_s are the parallel and perpendicular field components:

$$E_p = c_1(\theta)\cos\Theta\sin\theta + c_2(\theta)\sin\Theta\cos\theta\cos(\psi - \Phi), \tag{2.6}$$
$$E_s = c_3(\theta)\cos\Theta\sin(\psi - \Phi) \tag{2.7}$$

The c coefficients are

$$\begin{aligned} c_1(\theta) &= n^2\ \frac{\cos\theta}{cos\theta_S}\ t^p(\theta_S)\ \Pi(\theta_S), \\ c_2(\theta) &= n\ t^p(\theta_S)\ \Pi(\theta_S), \\ c_3(\theta) &= -n\ \frac{cos\theta}{cos\theta_S}\ t^s(\theta_S)\ \Pi(\theta_S) \end{aligned} \tag{2.8}$$

With

$$\Pi(\theta_S) = e^{-i\,k_0\,n_1\,\cos(\theta_S)\,\delta} \tag{2.9}$$

Here, $n = n_2/n_1$ is the relative refractive index, Π is the propagation factor for the light radiating through the upper halfspace and δ is the distance of the emitter from the substrate interface. t^p and t^s are the Fresnel transmission coefficients for p- and s-polarized light:

$$\begin{aligned} t^p &= \frac{2\,n_1\cos\theta_S}{n_1\cos\theta + n_2\cos\theta_S}, \\ t^s &= \frac{2\,n_1\cos\theta_S}{n_1\cos\theta_S + n_2\cos\theta} \end{aligned} \tag{2.10}$$

Figures 2.3 (a), (b) and (c) show the radiation patterns resulting from the calculation for dipoles oriented along the x-axis ($\Phi = 0°$, $\Theta = 90°$), y-axis ($\Phi = 90°$, $\Theta = 90°$) and z-axis ($\Phi = 0°$, $\Theta = 0°$), respectively, and emission wavelength at $\lambda = 702$ nm (as corresponding with the G Raman band from graphene (see chapter 3)). The radiation pattern of a randomly oriented point-dipole can be modeled as a sum of the three previously simulated dipole patterns (see figure 2.3 (d)). For the calculation it was assumed that the dipoles were place on a glass coverslip of refraction index $n_2 = 1.52$, surrounded by air with $n_1 = 1$ and in the focus of an oil immersion objective with NA = 1.4. The BFP patterns are scaled by the normalized wavevector components k_x/k_0 and k_y/k_0, where $k_0 = 2\pi/\lambda$. The area of signal detection is limited by the NA of the objective as $k_x^2/k_0^2 + k_y^2/k_0^2 \leq NA^2 = 1.4^2$. The strongest emission is seen for $k_x^2/k_0^2 + k_y^2/k_0^2 \geq 1$, corresponding to angles exceeding the critical angle of the glass-air interface. For dipolar emitters oriented parallel to the sample plane ($\Theta = 90°$), the radiation patterns exhibit two bright lobes located in the $k_x^2/k_0^2 + k_y^2/k_0^2 \geq 1$ region, with their maxima close to $\theta_{critical}$. The two bright lobes rotate according to the dipole orientation, as can be seem from figures 2.3(a),(b). For the case of

a dipole oriented parallel to the z-axis, no light is emitted to the center of the pattern. The strongest emission is also seen for $k_x^2/k_0^2+k_y^2/k_0^2 \geq 1$ close to $\theta_{critical}$. The randomly oriented radiation pattern also exhibits rotational symmetry, resembling the z-axis oriented pattern. However, the contribution of the two in-plane dipoles results in an increased intensity at the center and in a broader intensity distribution of the ring in the forbidden zone. Ultimately, it can be observed that the majority of the intensity is emitted in the outer ring regardless the dipole orientation. Consequently, using a high NA objective with $NA > 1$ is crucial for high collection efficiencies and it is especially important for the study of optical antennas [50].

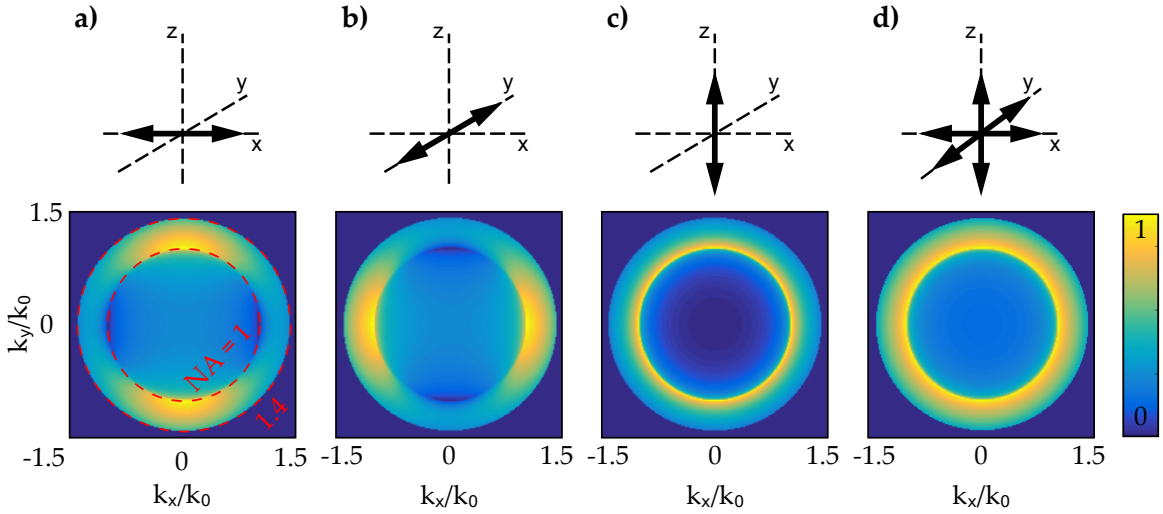

Figure 2.3: Calculated emission patterns for dipoled at an air-glass interface ($n_1 = 1$, $n_{glass} = 1.52$) in the back focal plane of a NA = 1.4 objective lens for orientations along the (a) x-axis ($\Phi = 0°$, $\Theta = 90°$), (b) y-axis ($\Phi = 90°$, $\Theta = 90°$) and (c) z-axis ($\Phi = 0°$, $\Theta = 0°$). (d) Calculated emission pattern for a random orientation of emitters represented by the incoherent sum of three dipoles oriented along the x, y and z-direction, respectively. The sketches on top of the patterns mark the dipole orientation in the real space, while the red dashed lines indicated the numerical aperture NA = 1 and 1.4, respectively. Adapted from references 27 and 50.

2.3 Detection efficiency

The previous section shows how the fraction of emission radiation into the different angular zones changes with the dipole orientation. As a consequence, the collected fraction might be higher for a vertical or a horizontal dipole depending on the numerical aperture of the objective, and therefore on its collection angle. This makes possible the distinction between contributions from differently oriented dipoles.

In order to visualize this, Figure 2.4 plots the detection efficiencies of a vertical $\gamma_{\parallel}$ and an in-plane $\gamma_{\perp}$ dipole as a function of the maximum collection angle θ_{max}. The detection efficiency $\gamma = P_{detected}/P_{total}$ is defined as the detected power in the allowed zone $P_{detected}$, plus a part of the forbidden zone, divided by total radiated power by the emitter P_{total} at a emission wavelength of $\lambda = 702$ nm. The blue vertical dashed line indicates the detection efficiencies $\gamma_{\perp} = 0.83$ and $\gamma_{\parallel} = 0.65$ for an objective of refraction index n = 1.52 and with an NA = 1.4 ($\theta_{max} = 67.3°$) as for all experiments presented in this work. For the sake of comparison, the detection efficiencies calculated for a common air objective with NA = 0.95 ($\theta_{max} = 38.7°$) are $\gamma_{\perp} = 0.15$ and $\gamma_{\parallel} = 0.29$, as indicated by the green dashed line.

In conclusion, the fraction γ of the total power radiated by a dipole into the angular detection range depends on the orientation of the dipole. Regardless dipole orientation, a higher numerical aperture results in an increased detection efficiency, making the use of high NA objectives an advantageous configuration.

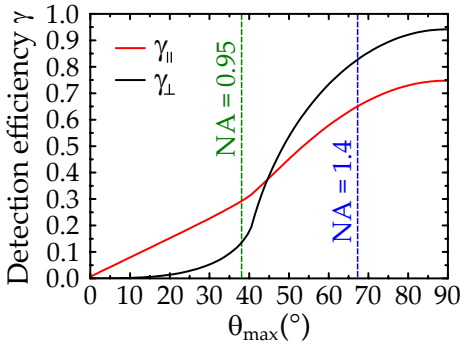

Figure 2.4: Detection efficiency for a vertical $\gamma_{\perp}$ and an in-plane $\gamma_{\parallel}$ dipoles on a glass substrate ($n_2 = 1.518$) as a function of the maximum detected angle θ_{max}. The data is normalized to the total radiated power by the emitter P_{total}. The dashed vertical lines indicates the maximum collected angle for an objective with numerical aperture NA = 1.4 (in blue) and NA = 0.95 (in green). Adapted from references 33 and 41.

2.4 Depolarization

An important feature to be considered when working with high NA objectives is the depolarization of the light due to focusing and the influence of the interface. For high NA and samples on an air-dielectric interface, the polarization reaching the sample after the objective does not correspond to the excitation polarization sent in before the objective. The same occurs with the polarization of the light emitted from the sample and the detected polarization of light after collection by the objective. The use of the objective results in polarization mixing and depolarization occurs for both excitation and emission light. The NA dependent depolarization shown in figure 2.5 was calculated as detailed in references 29, 51. For the excitation field, depolarization can be quantified by the ratio between the intensity component perpendicular to the polarization of a strongly focused linearly

polarized Gaussian laser beam $I(L)_{\perp}$ and the parallel one $I(L)_{\parallel}$ as $p_L = I(L)_{\parallel}/I(L)_{\perp}$. For emission, depolarization is quantified by the ratio between the detected intensity for parallel $I(S)_{\parallel}$ and perpendicular $I(L)_{\perp}$ polarization with respect to an emitting dipole as $p_L = I(S)_{\perp}/I(S)_{\parallel}$. Details on the calculations can be found in references 29, 51. Both effects are NA-dependent, whereas the depolarization has a larger influence on the emission than on the excitation light. The blue vertical dashed line indicates the depolarization ratios for excitation $p_L \approx 0.026$ and emission $p_S \approx 0.139$ for an objective of refraction index n = 1.518 and with an NA = 1.4 as for all experiments presented in this work. For the sake of comparison, the depolarization ratios calculated for a common air objective with NA = 0.95 are $p_L \approx 0.003$ and $p_S \approx 0.018$ as indicated by the green dashed line. In summary, this implies that the polarization contrast substantially decreases for increasing collection angle, due to polarization mixing caused by the air-dielectric interface. This is important for the quantitative analysis of polarization dependent intensities in confocal microscopy with high numerical aperture, as for example the I(2D)/I(G) ratio (see chapter 3), a crucial quantity for estimating the doping in graphene [29].

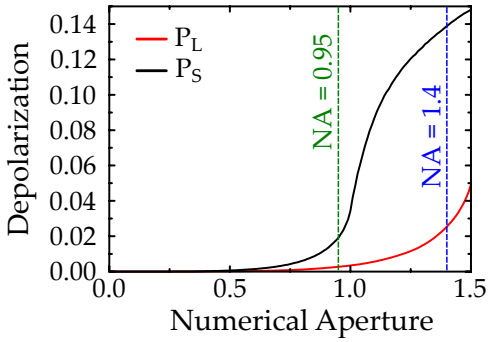

Figure 2.5: Depolarization of excitation p_L and emission p_S at the glass-air interface as a function of the focusing angle θ expressed by $NA = n \sin\theta$. Adapted from references 29 and 51.

2.5 Implementation of the experimental setup

The experimental setup for real space and Fourier space (BFP) imaging used for most measurements throughout this work is shown in Figure 2.6. An inverted confocal microscope (Nikon Eclipse TE 2000-S) with a 60X oil immersion objective ($NA = 1.4$) was used. Laser excitation at 632.8 nm was provided by a linearly polarized HeNe laser (Thorlabs Model HNL 210L). The laser light was spatially filtered and the beam expanded in order to fully fill the objective. The objective was used in epi-configuration to both focus the laser beam onto the sample and to collect the emitted light in backscattering geometry. The out-coming light was collimated and focused onto an avalanche photodiode (APD) or onto the entrance slit of a spectrometer equipped with a charge-coupled device (CCD) camera (Andor). Spectra were recorded by the spectrometer-CCD camera, after passing a laser

long pass filter. Narrow band pass filters (10 nm spectral window) centered at for example 700 and 760 nm, in combination with the laser long pass filter, were used to spectrally select the G and 2D Raman band signals of graphene, respectively. The transmitted Raman signal is then detected by the APD while raster-scanning the sample through the focus in order to obtain a Raman map. All polarized intensity data were also corrected for the polarization sensitive transmission of all optical elements in the beam path. The CCD camera could also be positioned in the focus of the collimating lens in the detection beam path in order to record BFP images. A flip mirror allows switching between real space and Fourier space. A more detailed exposition of the setup, together with an in-depth explanation of the BFP imaging implementation can be found in reference 51.

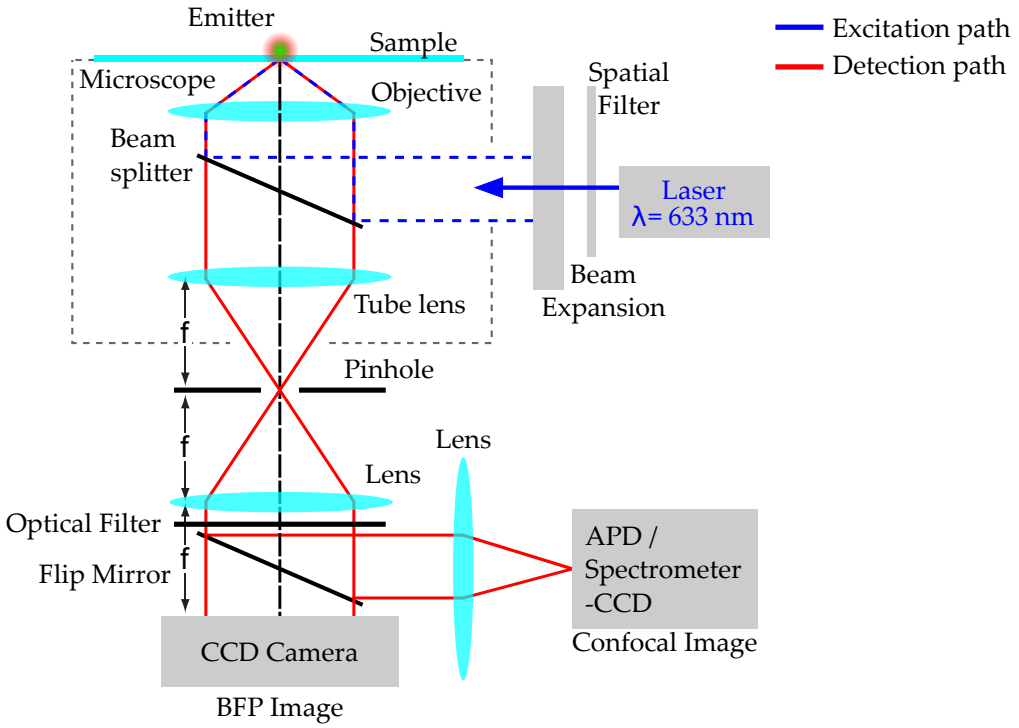

Figure 2.6: Confocal real space and BFP imaging setup.

Chapter 3

Raman spectroscopy of graphene

After the recent discovery of an easy method to fabricate and identify it [52], the interest in studying the fundamental properties of graphene has grown enormously due to the many unique properties of this two-dimensional material. Historically, Raman spectroscopy has played an important role in the structural characterization of carbon materials [53, 54, 55, 56, 57] and it is nowadays a very powerful tool for understanding the behavior of electrons and phonons in graphene [58, 59].

After introducing the basics of Raman scattering, section 3.1 gives a brief overview of this process in graphene, discussing the main Raman lines and giving an example of application: Raman microscopy and spectroscopy characterization of laser ablated patterns in graphene. The angular distribution of the G and 2D Raman scattering from graphene on glass is reported in section 3.2 by detecting back focal plane patterns. While the G scattering is confirmed to be nonpolarized, polarized scattering is observed in case of the 2D band. Parameter-free calculations show that both G and 2D Raman emission can be described by the superposition of incoherent point dipoles oriented in the graphene plane. The Raman tensors corresponding to these point dipoles are introduced in section 3.3. Here, depolarization effects are included in order to account for the decrease of polarization contrast due to polarization mixing caused by the air-dielectric interface. This influences the polarization ratio of 2D, and therefore the ratio I(2D)/I(G), a crucial quantity for estimating the doping in graphene. Moreover, the strong polarization dependence of the 2D peak intensity can also be shown spectroscopically. The experimental replication of Yoon's experiment [60] is presented in section 3.4, in order to show this dependence and further prove the validity of the tensors introduced in the section before.

3.1 Raman spectroscopy of graphene

Raman spectroscopy [61, 62] is a commonly used technique to provide a structural fingerprint by which molecules and solids can be characterized. This non-destructive technique offers high resolution, gives structural and electronic information, and it is applicable at both laboratory and mass-production scales, having applications in many different fields as

physics, chemistry, biology, medicine or industry [63]. Since the first record of the Raman spectrum of graphite [64] more than 40 years ago, Raman spectroscopy became one of the most popular characterization methods in carbon science and technology [65, 66, 59, 67, 68]. Raman techniques are particularly useful for graphene because the absence of a band gap makes all wavelengths of incident radiation resonant [69], thus the Raman spectrum contains information about both atomic structure and electronic properties [59].

Raman scattering is defined as inelastic scattering of photons by phonons. A photon impinging on a sample creates a time-dependent perturbation of the Hamiltonian of the system. Due to the fast changing electric field associated with the photon, only electrons respond to the perturbation. The perturbation introduced by a photon of energy $\hbar\omega_L$ increases the total energy to $E_{GS} + \hbar\omega_L$, where E_{GS} is the ground state energy. In general $E_{GS} + \hbar\omega_L$ does not correspond to a stationary state, therefore the system is said to be in a virtual level (i.e. a forced oscillation of the electrons with a frequency ω). Once the system relaxes, we can consider the photon as being emitted by the perturbed system, which jumps back to one of its stationary states. Depending on the final state of the system, the scattering process can be classified (see Figure 3.1).

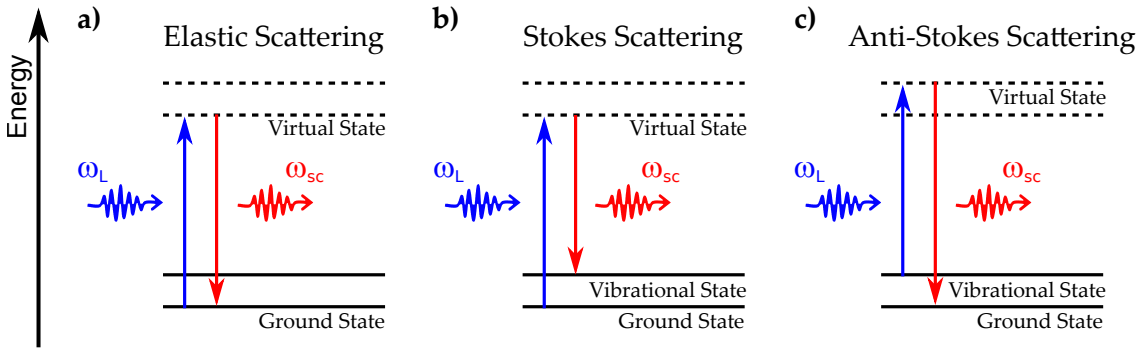

Figure 3.1: Energy level diagrams of (a) elastic and (b,c) Raman scatterings. Illumination of the system with a laser source of frequency ω_L can result in different processes. (a) Elastic scattering happens when there is no exchange of energy, so incident and scattered photons have the same energy $\hbar\omega_{sc} = \hbar\omega_L$. (b) Stokes Raman scattering occurs when the system absorbs part of the energy of the incident photon, resulting in the creation of a phonon of energy $\hbar\omega_{\mathbf{q}} = \hbar\omega_L - \hbar\omega_{sc}$. (c) Anti-Stokes takes place when the system loses energy because of the annihilation of a phonon of energy $\hbar\omega_{\mathbf{q}} = \hbar\omega_{sc} - \hbar\omega_L$.

Elastic scattering, also known as Rayleigh scattering, takes place when the system returns to its initial state, and the frequency of the emitted photon remains the same as the incident one, as it happens to the vast majority of the scattered photons. All that can happen to the photon is a change in its propagation direction (see Figure 3.1(a)). As an example of application, elastic scattering is commonly used to image graphene flakes and derive the number of layers [70, 71, 72], enabling to see even a single graphene layer by simply using an optical microscope [73].

Raman scattering happens when, with a much lower probability than Rayleigh scattering, the photon can lose part of its energy in the interaction process, thus exiting the sample with a lower energy $\hbar\omega_{sc}$. Since the sample has to return to a stationary state, the energy loss must correspond to a phonon energy $\hbar\omega_L - \hbar\omega_{sc} = \hbar\omega_q$. This corresponds to creation of a phonon, and the process is known as Stokes (S) scattering (see Figure 3.1(b)). If the incoming photon finds the system in an excited vibrational state, and after the interaction the system returns to a lower level, e.g. its ground level, the photon can leave the crystal with a an increased energy $\hbar\omega_{sc} = \hbar\omega_L + \hbar\omega_q$. This corresponds to the absorption of a preexisting phonon, and the process is known as Anti-Stokes (AS) scattering (see Figure 3.1(c)). Both processes occur almost instantaneously on the femtosecond timescale. If $\mathbf{k_L}$ and $\omega_L = c\mathbf{k_L}$ are the wave vector and the frequency of the incoming photon, $\mathbf{k_{sc}}$ and $\omega_{sc} = c\mathbf{k_{sc}}$ those of the scattered photon (c being the speed of light), and $\mathbf{q}$ and $\omega_\mathbf{q}$ those of a phonon, then energy and momentum conservation give:

$$\hbar\omega_L = \hbar\omega_{sc} \pm \hbar\omega_\mathbf{q} \tag{3.1}$$

$$\mathbf{k}_L = \mathbf{k}_{sc} \pm \mathbf{q} \tag{3.2}$$

The $\pm$ indicates Stokes and Anti-Stokes scattering. Given that the Stokes process is the most probable because of the higher probability of finding the system in the vibrational ground state, the immense majority of Raman spectra in literature are Stokes measurements. In this thesis, only Stokes processes were investigated. More information about Rayleigh and Raman scattering can be found in reference [74].

Worth noticing is that when the $E_{GS} + \hbar\omega_L$ does not correspond to a stationary state, as is indeed the case for most materials, the Raman process is called non resonant. However, if the excitation is selected to match a specific energy level, then the process is resonant. As a result, the output intensity is strongly enhanced, as a consequence of the greater perturbation efficiency. In the case of graphene, the absence of a band gap makes all wavelengths of incident radiation resonant, making Raman spectroscopy a particular useful tool to study graphene [69].

Raman scattering on phonons is to a large extent determined by electrons. Therefore, any variation of the graphene electronic properties due to defects, edges, doping or magnetic fields affects the positions, widts and intensities of the Raman peaks, enabling one to probe electrons via phonons [75, 76]. Hence, Raman spectroscopy is used to determine the number and orientation of layers [77], the quality and types of edge [78], and the effects of perturbations such as electric and magnetic fields, strain [79, 80, 81, 82], doping [83], disorder, functional groups, etc [59]. As a result, Raman spectroscopy is not only an interesting method to study fundamental physics in graphene, but also an invaluable tool for characterization and quality control, making it an integral part of graphene research.

Figure 3.2 shows a typical spectrum of a single layer graphene flake. The main Raman peaks, visible in the spectrum, and the processes underlying them, as sketched in figure 3.3, will be discussed in the following. In a first order process, only one phonon is involved.

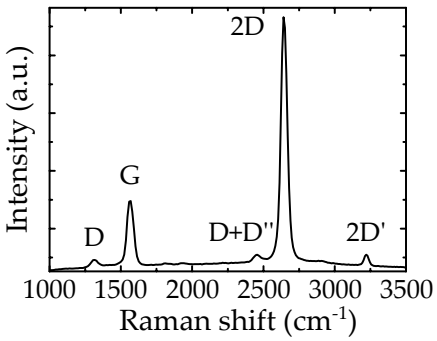

Figure 3.2: Example of single layer graphene flake Raman spectrum showing the main Raman peaks.

For incident light in the visible range, and considering that the lattice parameter of a solid is typically in the order of a few angstroms, due to momentum conservation (Eq. 3.1), only phonons with $q \approx 0$ are observed (fundamental Raman selection rule). This corresponds to perpendicular transitions in the band dispersion (see Figure 3.3(a)), meaning that phonons involved in first order processes have therefore very little momentum (i.e. the process is at the Γ point).

The most prominent first order peak is the G band, appearing at about $1580cm^{-1}$ (see figure 3.2). The G band is common to all sp2 carbon systems, including amorphous carbon, carbon nanotubes, and graphite, and is related to the in-plane C=C stretching mode [64]. The mechanism giving rise to the G band starts with an incident photon that resonantly excites a virtual electron-hole pair in the graphene. The electron or the hole is scattered by either an in-plane transverse optical (iTO) or in-plane longitudinal optical (iLO) zone-center phonon. The electron-hole pair then radiatively recombines and emits a photon that is red shifted by the amount of energy given to the phonon, as shown in Figure 3.3(a). For graphene and graphite these two modes are degenerate, but the degeneracy can be lifted by rolling the graphene sheet into a carbon nanotube, which splits the G band into the G+ and G- bands [84]. In this way, the width of the G band can also be used to measure the deformation and strain on a sample [79].

Unlike in a first order process, in higher order scattering processes the phonon vector q is not restricted to zero. A second order process can either involve two phonons (see figure 3.3(b),(c)), or one phonon combined with an elastic scattering event (see fig 3.3(d)). The strongest peak in single layer graphene is the 2D (also known as G' band), appearing at about $2700cm^{-1}$ (see figure 3.2). The 2D peak is a second order Raman process originating from the in-plane breathing-like mode of the carbon rings. Figure 3.3(b),(c) shows a diagram of the Raman 2D processes. Figure 3.3(b) shows the double resonance process in which an electron-hole pair is created by an incident photon **q** near the K point. The electron is inelastically scattered by a iTO phonon to the K' point. Before recombining with the hole, the electron is back-scattered to K by a second iTO phonon **-q** with the same energy but opposite momentum as the previous one, in order for the Raman process to fulfill energy and momentum conservation. The same process can also occur for the hole

instead of the electron. This process is known as double resonant, because the incident or scattered photon and the first or second phonon scattering are resonant with electronic levels in the graphene. Alternatively, the 2D band process can also be triple resonant, which is shown in the lower panel of figure Figure 3.3(c). In this case, both carriers are scattered by iTO phonons from near the K point to the K' point and recombine by emitting a photon. Experimentally the 2D band can be used to determine the number of graphene layers in a flake [77] (by looking at the peak shape/width and its ratio with respect to the G peak). For single layer graphene, the 2D band is a single Lorentzian and the 2D/G ratio is ~ 4 [77]. For bilayer graphene, the 2D band splits into four peaks, making the peak slightly broader[77, 85] and also reducing the 2D/G ratio.

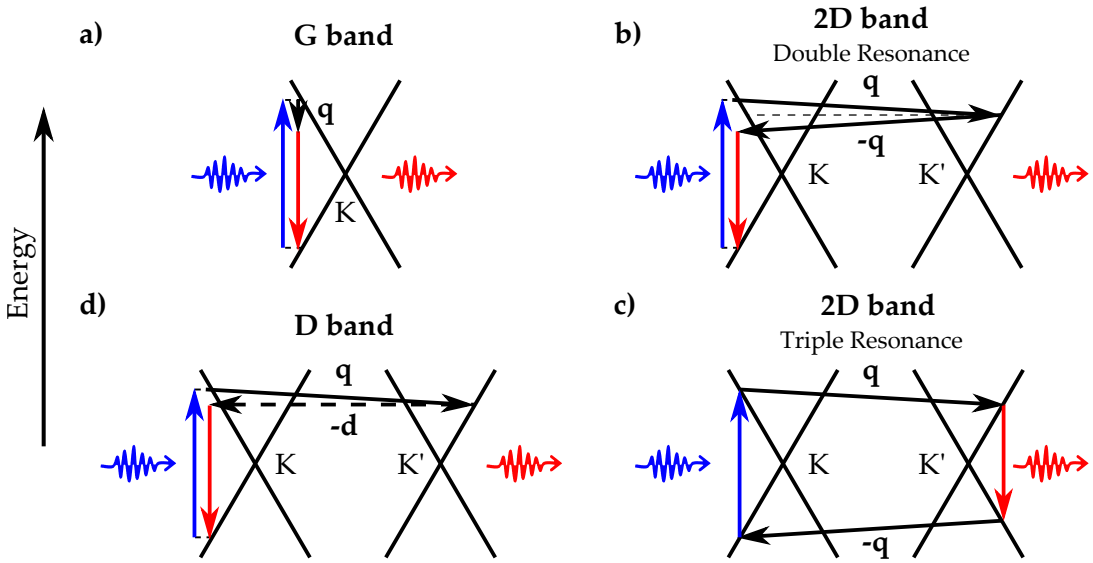

Figure 3.3: Sketch of the main Raman processes in graphene, giving rise to the most characteristic Raman bands: (a) G band process involving one phonon (black arrow), (b,c) second-order 2D band process, involving two phonons, which is either double (b) or triple (c) resonant, and (d) double-resonant D band process involving scattering at a defect (horizontal dashed line). The scattering processes are pictured within the electronic bands, the characteristic cone band structure of graphene. The blue and red arrows represent the incoming and outgoing light, respectively. Figure adapted from reference [78].

Another important band, resulting from a different second order Raman process, is the disorder-induced D band, which occurs at about $1350cm^{-1}$ [64]. In this case, an electron-hole pair is created by an incident photon near the K point. Similarly to the 2D process, the electron is inelastically scattered by an iTO phonon **q** from the K point to the K' point. However, in this case, the electron is elastically back-scattered to the K point by a defect **-d** [86, 87, 88]. The defect is required in order to fulfill momentum conservation. More specifically, a defect is any breaking of the symmetry of the graphene lattice, such as sp3 defects [89], a vacancy sites [90, 91], grain boundaries [92], or even an edge [93, 94, 95]. Since only one phonon is involved in the process, the energy shift for the D band is half of

the one for the 2D band (the 2D band is the overtone of the D band).

Besides the described Raman bands there are several other Raman modes in graphene, such as the D', D+D', 2D' modes, still due to in-plane vibrations. But for few-layer graphene there exist also shear modes [96] and layer breathing modes [97, 98], due to relative motions of the planes themselves, either perpendicular or parallel to their normal. A more detailed discussion about Raman spectroscopy in graphene can be found in references [58, 59].

3.1.1 Application: Characterization of laser ablated patterns in graphene

An example of a possible application of Raman scattering microscopy and spectroscopy is the characterization of patterned nanoscale structures of graphene. Laser ablation of structures in graphene is of particular interest for the flexibility that it affords in fabricating graphene based devices [99]. In order to guarantee the complete ablation and the quality of the patterning, as for example checking that there are no graphene leftovers or there was not formation of amorphous carbon during the ablation, Raman scattering investigations proved to be very useful [100, 101].

The characterization of a hole ablated in graphene is presented in Figure 3.4. The hole was ablated by G. Piredda and co-workers at the Josef Ressel Center for material processing with ultrashort pulsed lasers in the Vorarlberg University of Applied Sciences. A single monolayer graphene on glas used for this experiment was purchased from Graphenea (San Sebastian, Spain). Single pulses from the frequency-doubled output of a Spectra-Physics Spirit laser with pulse duration of sub-400 fs were used to ablate graphene. The pattern consists of an array of single-laser shot ablation spots of diameter $\sim 20\mu m$. A detailed elastic scattering map of an ablation spot is shown in figure 3.4(a). The ablated area in the center of the map shows higher intensities than the areas where graphene is still present, since the graphene sheet absorbs the light [102]. The same area is covered by a 2D Raman band map and shown in figure 3.4(b). In contraposition to Figure3.4(a), here the laser ablated area shows weaker signal (background signal) than the surroundings, and the positions were there is more carbon material (rolled-up graphene, amorphous carbon, etc.) presents higher intensity while the elastic scattering map is showing light absorption. The spectrum taken in the laser irradiated spot (black dot in Figure 3.4(b)) corroborates that there is no remaining graphene at this position (see Figure 3.4c, black line), while the surroundings (red dot in Figure 3.4(b)) presents a typical graphene spectrum (see Figure 3.4c, red line). The lower background signal on the former case is due to light absorption from graphene. Spectra acquired along the gray dashed line in figure 3.4(b) are presented in a two dimensional map in figure 3.4(d) for wavenumbers from 1000 to 2900 cm^{-1}. Figure 3.4(e) shows the integrated intensity for the three different Raman lines. While the intensity for the G and 2D bands stays constant in bare graphene, their intensity decays when reaching the edge, diluting into noise for the ablated area, and therefore proving that there are no graphene leftovers. An increase of the D peak, an indicator of structural

defects[94], can be observed to be localized at the edge (see inset of figure 3.4(e)).

In conclusion, elastic scattering and Raman scattering maps in combination with a spectral line scan verifies ultrashort laser single-shot ablation of monolayer graphene on glass in a clean way (no sign of amorphous carbon formation), and with minimal damage next to the edge.

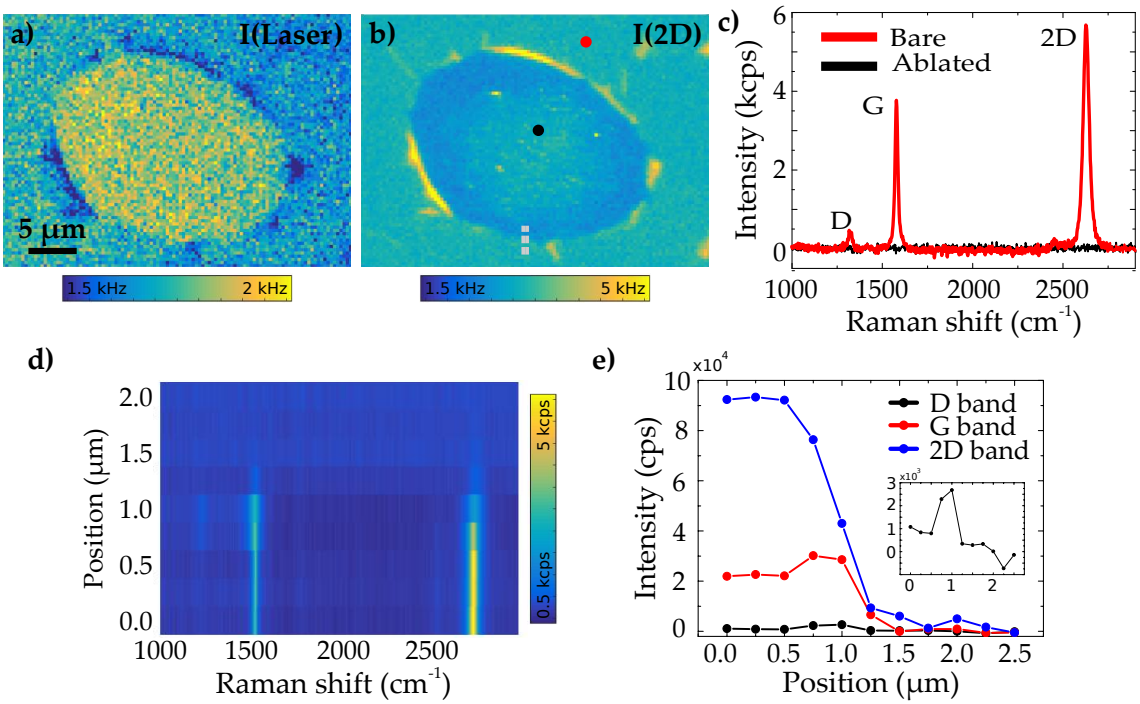

Figure 3.4: (a) Elastic and (b) Raman scattering maps of an ultrashort laser single-shot ablated hole in graphene. (c) Spectra taken from the ablated area (black dot in panel b) and from the non ablated graphene area, in black and red lines, respectively. (d) Spectra acquired along the gray dashed line in panel b as function of the position and (e) the integrated intensity for the three different Raman lines show clean ablation of graphene. Inset: Maginified intensity profile of the D band.

3.2 Radiation patterns of Raman scattering from graphene

This section is based on the publication "*Raman radiation patterns of graphene*" by Harald Budde, Nicolás Coca-López, Xian Shi, Richard Ciesielski, Antonio Lombardo, Duhee Yoon, Andrea C. Ferrari, and Achim Hartschuh. ACS Nano, vol. 10, no. 2, pp. 1756-1763, 2016.

In this section the angular distribution of the G and 2D Raman scattering from graphene on glass is presented. The angular distribution of the emission carries important

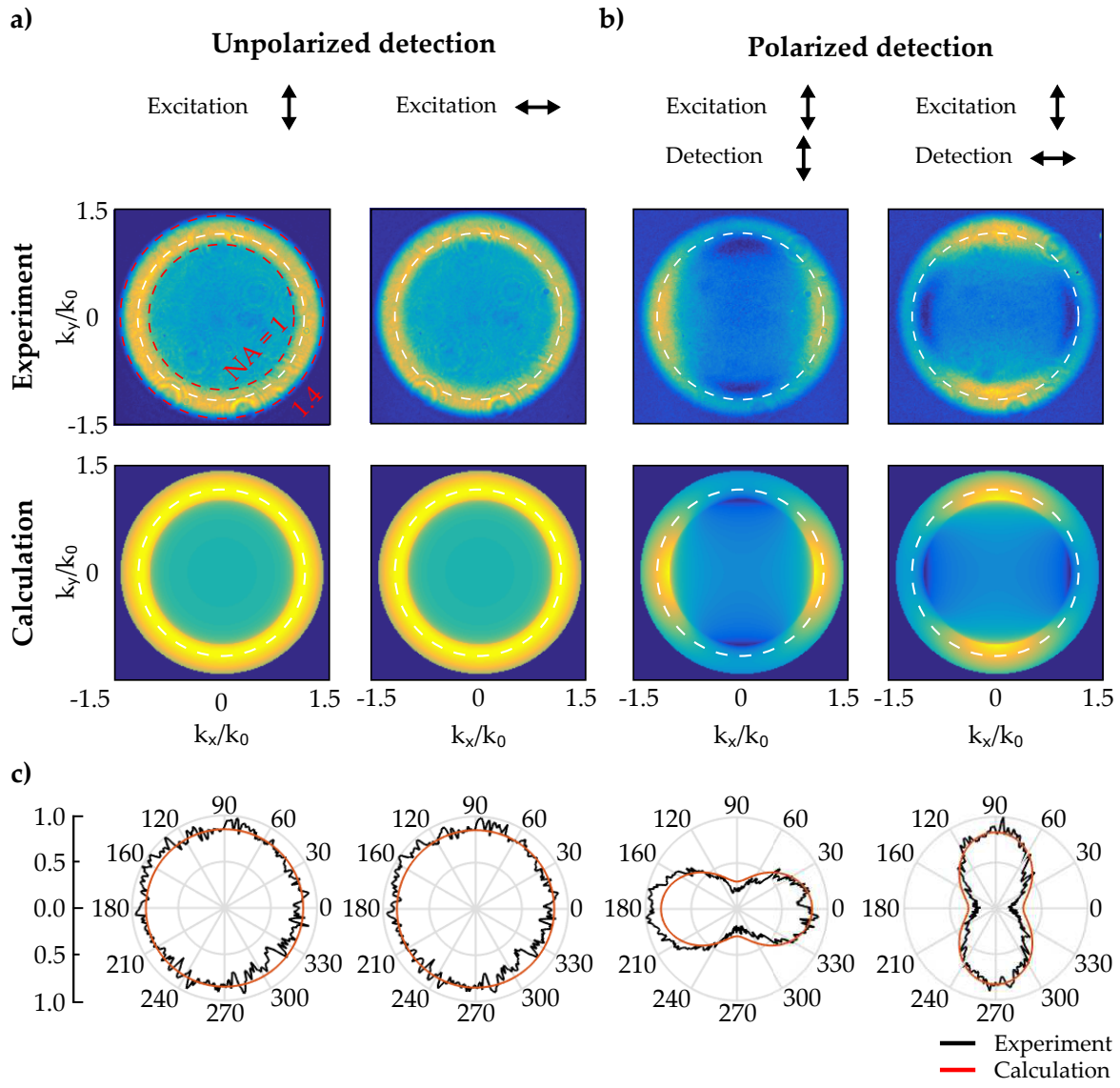

Figure 3.5: (a) Experimental and calculated G peak back focal plane images with and without analyzer. The same scaling is used in each row for the experimental and theoretical data. The black arrows indicate the direction of the polarization. (b) Cross sections taken following the withe dashed lines in the patterns shown in (a), corresponding to a $NA = 1.15$.

information on the nature of the emissive state, such as its dipolar [27] or multipolar [103] character, its polarization state [104, 44] and its coupling to the environment [27, 44]. From a practical perspective, the angular distribution of emission determines the detection yield (ratio of detected to emitted light) achieved in an optical measurement, thus being crucial for the quantitative analysis of the observed emission intensities and polarization [105].

Here, the angular distribution of Raman scattering from graphene on a glass substrate is studied by detecting the patterns originated at the BFP of the collecting microscope objective. Figure 3.5(a) shows a collection of experimental (panels i-iv) and calculated (panels v-viii) BFP images of the G peak, with and without analyzer in the detection beam path, and its corresponding cross sections (Figure 3.5(b)). Without analyzer in the detection beam path, the pattern features a ring of uniform intensity (Figure 3.5(a,i)). The strongest emission is seen for $k_x^2/k_0^2 + k_y^2/k_0^2 \geq 1$, corresponding to angles exceeding the critical angle of the glass-air interface $\theta_{crit} = \arcsin(n_{air}/n_{glass})$, giving $NA = n_{glass} \sin\theta_{crit} = 1$. This is expected due to the increased photon density of states in this angular range and the connected enhancement of spontaneous emission [4]. In order to exclude possible imaging artefacts, the excitation polarization is rotated by 90°, leading to an identical pattern (Figure 3.5(a,ii)), as expected due to SLG symmetry properties. For polarized detection, two bright lobes in the direction orthogonal to the detection polarization are seen (Figure 3.5(a,iii)). Rotating the analyzer by 90° rotates the resulting pattern, retaining its intensity (Figure 3.5(a,iv)). Because the same intensity is seen for parallel and perpendicular detection polarization, isotropy of the G band emission polarization can be inferred, consistent with previous reports [60, 106]. The comparison between the G peak experimental BFP patterns with analyzer in Figures 3.5 (a,iii-iv) with the calculated pattern of a point-dipole in Figure 2.3 indicates that the G Raman scattering in SLG can be modeled by the incoherent sum of two orthogonal in-plane point dipoles. This is confirmed by the corresponding series of parameter-free calculated patterns for the respective excitation and detection conditions, presented in the lower row of Figure 3.5(a,v-viii). The quantitative agreement between experimental and theoretical emission distribution can also be seen from the comparison of the corresponding normalized cross sections in Figure 3.5(b) obtained at the position of the white dashed line (NA = 1.15) in panels 3.5(i-viii).

Figure 3.6 plots the experimental (Figure 3.6(a), panels i-iv) and calculated (Figure 3.6(a), panels v-viii) BFP patterns of the 2D band, with and without analyzer in the detection beam path, and its corresponding cross sections (Figure 3.6(b)). Unlike those of the G band, the patterns with unpolarized detection do not exhibit radial symmetry, indicating polarized Raman scattering. The patterns recorded for polarized detection (Figure 3.6(a,iii-iv)) also resemble a superposition of two orthogonal dipoles, although with weaker intensity for the cross-polarized case (Figure 3.6(a,iv)). The ratio of parallel to cross-polarized 2D intensities $r_{2D} = I(2D)_{\parallel}/I(2D)_{\perp}$ was previously reported to be ~ 3 [60, 107]. Thus the BFP patterns in Figure 3.6(a,v-viii) were calculated as the incoherent sum of two orthogonal dipoles with an intensity ratio of 1 : 3. Both patterns and corresponding cross sections (Figure 3.6(b)) are in good agreement with experiments.

On the other hand, due to the threefold symmetry of the double resonant Raman process around K and K', the 2D emission can also be considered to result from three

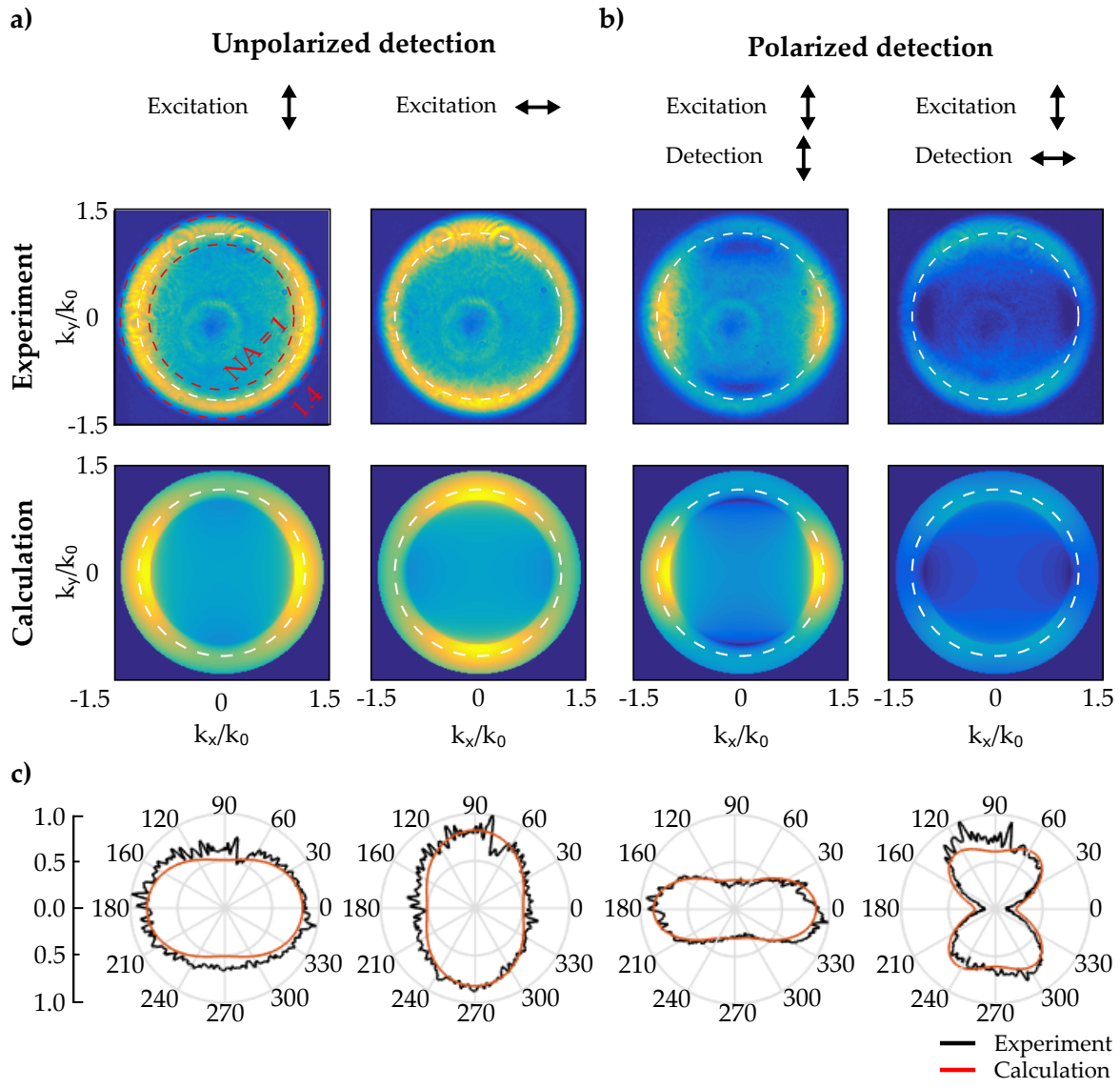

Figure 3.6: (a) Experimental and calculated 2D peak back focal plane images with and without analyzer. The same scaling is used in each row for the experimental and theoretical data. The black arrows indicate the direction of the polarization. (b) Cross sections taken following the withe dashed lines in the patterns shown in (a), corresponding to a $NA = 1.15$.

dipoles each rotated in-plane by 120°, as discussed below. For linearly polarized light, the excitation efficiency of the three dipoles scales with the angle δ between the incident field $\vec{E}$ and the dipole axis $\vec{p}$ as $|\vec{p}\cdot\vec{E}|^2 \sim \cos^2(\delta)$. Without loss of generality, we consider one dipole to be parallel to the laser polarization, and the other two rotated by 120° and 240°, thus excited with a lower efficiency of $cos^2(120°) = cos^2(240°) = 1/4$. The BFP patterns calculated with three dipoles weighted $1 : 1/4 : 1/4$ are in good agreement with the experimental patterns as well as with results obtained by the 2-dipole model.

3.3 Phenomenological Raman tensors

Using group theory, the G and 2D Raman scattering intensities can be calculated as ([60, 108, 109, 59]):

$$I(G;2D) \propto \sum_{i}^{m} \mid \hat{e}_S \cdot R_i \ \cdot \hat{e}_L \mid^2 \tag{3.3}$$

where $\hat{e}_L$ and $\hat{e}_S$ are the unit polarization vectors of the incident and scattered light at the focus of the microscope objective. R_i stands for the Raman polarizability tensors for either the G or the 2D bands with $i = 1$, and $m = 2$ $m = 3$, respectively. Given that the G mode in graphene exhibits E_{2g} symmetry [110, 111], it can be represented by the Raman tensors

$$R_1(G) = \begin{pmatrix} 1 & 0 \\ 0 & -1 \end{pmatrix};\ R_2(G) = \begin{pmatrix} 0 & 1 \\ 1 & 0 \end{pmatrix}, \tag{3.4}$$

as suggested by Yoon and coworkers in reference [60]. In this case, Equation 3.3 can also be understood as the sum of two orthogonal incoherent point dipoles. The dot products $R_i \cdot \hat{e}_S$ in Equation 3.4 correspond to the oscillation direction of the two orthogonal point dipoles, while the sum of the modulus square accounts for an incoherent superposition. If the unit polarization vectors are define as $\hat{e}_L = (\cos\theta_L, \sin\theta_L)$ and $\hat{e}_S = (\cos\theta_S, \sin\theta_S)$, the Raman intensity is found to be $I(G) = 1$, meaning that the Raman intensity of the G band does not depend on the polarization direction of either the incident or scattered light. This explains the uniform angular emission for the unpolarized patterns in Figure 3.5(a,i-ii) and the same total intensity emission for two different analyzer angles in the patterns shown in Figure 3.5(a,iii-iv).

It occurs differently for the 2D band case, where the double resonant process [112, 86] and the interplay of photon-electron and electron-phonon coupling [64, 68, 86, 67] need to be taken into account [105]. Inter-valley scattering between **K** and **K'** with six possible **K-K'** and **K'-K** combinations [60] also needs to be considered. Due to symmetry, the discussion can be limited to three **K-K'** combinations [60]. Double resonant inter-valley scattering results in distinct electronic populations around the three different **K'** points neighboring the **K** point, each rotated by 120° [60]. Thus the 2D band can be described as a sum of three incoherent dipoles corresponding to the following three Raman tensors:

$$R_1(2D) = \begin{pmatrix} 1 & 0 \\ 0 & 1 \end{pmatrix};\ R_2(2D) = \frac{1}{4}\begin{pmatrix} -1 & -\sqrt{3} \\ \sqrt{3} & -1 \end{pmatrix};$$
$$R_3(2D) = \frac{1}{4}\begin{pmatrix} -1 & \sqrt{3} \\ -\sqrt{3} & -1 \end{pmatrix} \tag{3.5}$$

Tensors R_2 and R_3 are obtained *via* rotation of R_1 by 120° and 240°, correcting the excitation efficiency of the dipoles by the scaling ratio $1 : 1/\cos^2(120°) : 1/\cos^2(240°) = 1 : 1/4 : 1/4$.

The Raman intensity is then found to be $I(2D) = f(\beta)$, where β is the angle difference between the direction of the incident light polarization and the scattered light polarization, $\beta = \theta_S - \theta_L$. This means that the Raman intensity of the 2D band does not depend on the polarization direction of the incident light or the polarization direction of the scattered light, but rather in the difference between them, as experimentally demonstrated by Yoon et al. [60].

Importantly, because the excitation field is coherent within the focal area, the modulus square in equation 3.3 would need to include the spatial integral of the induced Raman polarization in case of fully coherent scattering. In general, spatially coherent Raman scattering could influence the observed far-field radiation patterns if the coherence length is $\sim \lambda/4$, in which case retardation effects start playing a role [108, 113, 114]. Since all the experimentally recorded BFP patterns can be quantitatively described using point dipoles located at the same position, the coherence length is expected to be substantially smaller [113, 114]. References [113, 114] reported that spatially coherent Raman scattering influences the near-field optical response with coherence length ~ 30 nm. Since this length is $< \lambda/4$, our treatment of SLG Raman scattering as spatially incoherent is justified.

For $NA > 1$ and for samples on an air-dielectric interface, the polarization directions entering in Eq.3.3 do not correspond to the polarization directions outside the focus. Due to its symmetry properties with $|R_1 \cdot \hat{e}_x| = |R_2 \cdot \hat{e}_y|$ the effect of polarization mixing cancels out in the case of the G peak, but not for 2D. This polarization mixing that becomes visible for $NA = n_{glass} \sin\theta > 1$ thus influences the experimentally observed ratio r_{2D} as it will be discussed in the following. The quantification of the depolarization for excitation and emission light for the used setup can be found in reference [105]. Considering depolarization, equation 3.3 can then be reformulated into a more general expression for both G and 2D:

$$I(G;2D) \propto \sum_{i,j,k} \mid \hat{e}_S \cdot P_S^j \cdot R_i \ \cdot P_L^k \cdot \hat{e}_L \mid^2 \tag{3.6}$$

with i = 1,2 and i=1,2,3 in case of G and 2D, respectively and j,k=$\parallel$, $\perp$. The depolarization matrices are developed considering the depolarization of the excitation and emission p_L and p_S calculated in reference [29]:

$$P_{S,L}^{\perp} = \begin{pmatrix} 0 & \sqrt{p_{S,L}} \\ -\sqrt{p_{S,L}} & 0 \end{pmatrix};\ P_{S,L}^{\parallel} = \begin{pmatrix} \sqrt{1-p_{S,L}} & 0 \\ 0 & \sqrt{1-p_{S,L}} \end{pmatrix} \tag{3.7}$$

For $NA = 1$, $p_S \approx 0.035$ and $p_L \approx 0.003$, while for $NA = 1.4$ $p_S \approx 0.14$ and $p_L \approx 0.025$. Therefore, for $NA < 1$ the influence of the depolarization matrices can be neglected and Eq.3.6 simplifies to Eq.3.3.

Unlike the G peak, the 2D peak intensity depends on polarization and is thus influenced by the depolarization of excitation and emission. Because depolarization depends on NA, r_{2D} becomes NA-dependent as well. This dependence can be calculated using the Equations 3.6, 3.7 and 3.5 as:

$$r_{2D}(NA) = \frac{I(2D)_{\parallel}}{I(2D)_{\perp}} = \frac{3 - 2p_S - 2p_L + 4p_S p_L}{1 + 2p_S + 2p_L - 4p_S p_L} \tag{3.8}$$

Figure 3.7 compares the ratio obtained from equation 3.8 with the experimental ones for increasing NA. Both experimental and theoretical data show a substantial decrease of ~30% towards larger NA. Deviations of the experimental data from the predicted curve are presumably due to the background correction for laser scattered light for small collection angles and reduced objective transmittance for large ones [44, 115, 116].

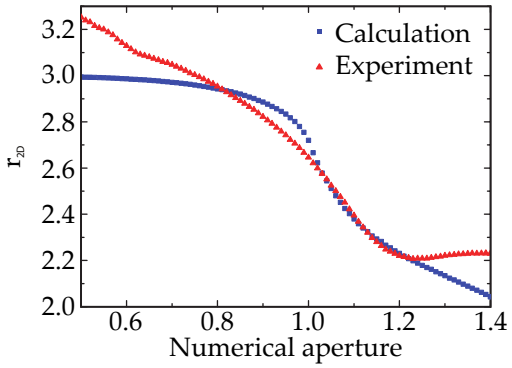

Figure 3.7: Experimental (red triangles) and calculated (blue squares) 2D intensity ratio for parallel and perpendicular polarized light $r_{2D} = I(2D)_{\parallel}/I(2D)_{\perp}$. The calculation is a plot of equation 3.8. Adapted from reference [105].

The intensity ratio $I(2D)/I(G)$ is crucial to derive the doping of graphene [59, 75, 83, 117]. Polarization mixing caused by the air-glass interface with different effects on I(2D) and I(G) would thus change I(2D)/I(G). Importantly, this ratio is dependent on the r_{2D} ratio, as calculated in [105], implying that $I(2D)/I(G)$ is also depending on the NA. Therefore, the influence of the NA can not be longer neglected in quantitative analysis of Raman intensities in confocal microscopy with high numerical aperture.

3.4 Polarization dependence of Raman Intensities in graphene

The strong polarization dependence of the 2D peak intensity can also be shown spectroscopically [106, 60]. Here, the experimental replication of Yoon's experiment [60] is presented,

in order to spectroscopically show this dependence and further prove the validity of the tensors introduced to describe the 2D peak (see matrices 3.5). Figure 3.8(a) represents the orientation of the incident polarization ($\hat{e}_L$) and the scattered polarization filtered by an analyzer ($\hat{e}_S$), both being in the graphene plane. These are described by the angles θ_L and θ_S, respectively. Figure 3.8(b) is a collection of Raman spectra at the center of a single layer graphene sample for different incident light polarizations ($\theta_L = 0°, 30°, 60°, 90°$), while keeping the analyzer fixed at $\theta_S = 0$. In order to eliminate experimental fluctuations between different measurements, the spectra is normalized to the intensity of the G band, since the intensity of the G band must be independent of the polarizations of the incident or scattered photons [60]. The integrated area under the 2D peak is plotted in figure 3.8(c) (black dots), where the points and error bars were obtained by averaging the four different spectra obtained for every θ_L. The normalized intensity is maximum when the scattered polarization is parallel to the incident polarization and minimum when the two polarizations are perpendicular to teach other. The largest normalized intensity of the 2D band is about 2.69 times the smallest ($r_{2D} = 2.69$). As expected, the same oscillating behavior shifted by 90° is observed when the analyzer is fixed at $\theta_S = 90°$ (Figure 3.8(c, red dots)). The experimental trend can be fitted making use of equation 3.3 and the Raman tensors 3.4 and 3.5 (see black and red lines in figure3.8 (c) for $\theta_S = 0°$ and 90°, respectively). Without considering depolarization, the suggested Raman tensors yield a ratio $r_{2D} = 3$. If depolarization of the scattered light is taken into account, the contrast is reduced and the ratio is observed to be $r_{2D} = 2.03$, considering an $NA = 1.4$ (see black and red dashed lines in figure 3.8(c), for $\theta_S = 0°$ and 90°, respectively). The discrepancies between calculation and theory can be attributed to several reasons. On one hand, choosing the value to which curves are to be normalized becomes challenging due to a limited signal to noise ratio. On the other hand, the 2D Raman tensors were developed according to a ratio $r_2D = 3$, while other researchers have measured and calculated this value to be up to $r_2D = 3.4$ [107].

Nevertheless, the oscillatory behavior is well captured by the suggested model and, as mentioned before, the 2D peak intensity does not depend on θ_S or θ_L individually, but on their difference $\beta = \theta_S - \theta_L$. This is captured in figure 3.8(d), where the normalized intensity of I_{2D}/I_G is calculated as a function of θ_S and θ_L, according to equation 3.3. As experimentally observed, this intensity is maximum when the scattered polarization is parallel to the incident polarization and minimum when the two polarizations are perpendicular to teach other, independently of the incident polarization.

This strong polarization dependence observed for the 2D peak is a direct consequence of inhomogeneous optical absorption and emission mediated by electron-phonon interactions in the double-resonant Raman scattering processes [60]. On one hand, it is known that for a given polarization vector $\vec{P}$ of a linearly polarized incident (scattered) light, the light absorption or emission probability per unit time in graphene is proportional to $\mid \vec{P} \times \vec{k} \mid^2$, where $\vec{k}$ is the wave vector of the electron (measured from the K or K' point) [118]. It implies that the absorption or emission of polarized light is absent when the direction of momentum of electron is parallel to the polarization vector while it is maximized when they are perpendicular to each other. On the other hand, the electron-phonon interactions

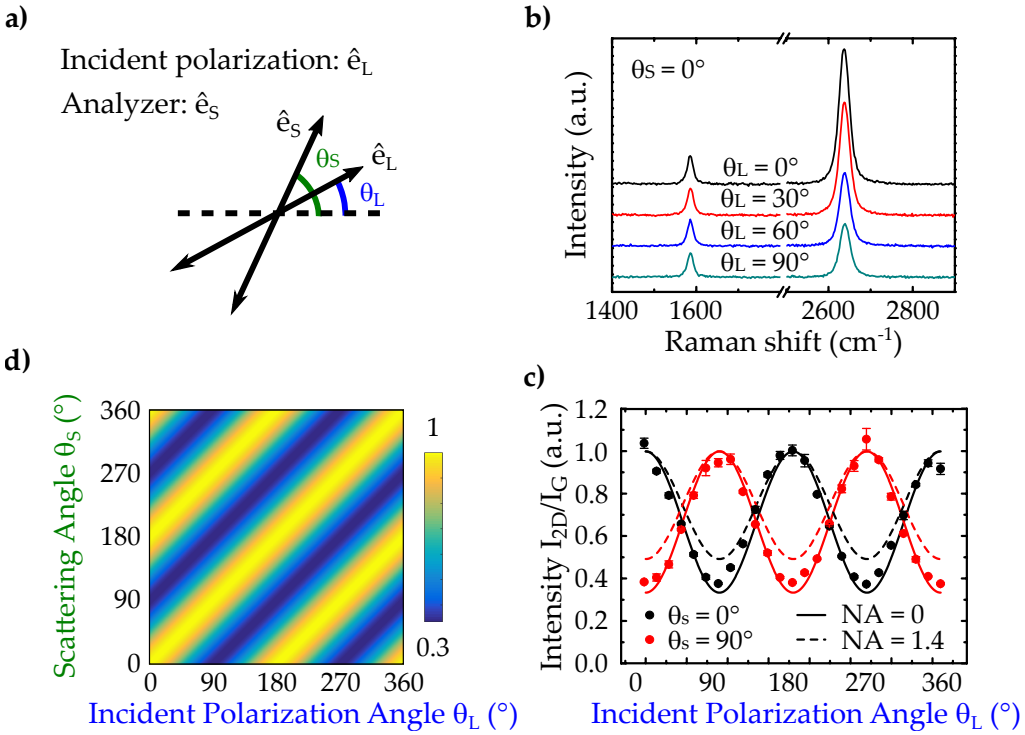

Figure 3.8: Polarization dependence of Raman scattering in graphene. (a) Sketch showing the orientation of the incident ($\hat{e}_L$) and scattered polarization filtered by an analyzer ($\hat{e}_S$), both being in the graphene plane. (b) Raman spectra of a single layer graphene sample for different incident light polarizations θ_L and a fixed analyzer angle $\theta_S = 0$. (c) Normalized integrated area under the 2D peak for different incident laser polarization with the analyzer fixed at $\theta_S = 0^{\cdot}$ (black dots) and $\theta_S = 90^{\cdot}$ (red dots). The black and red lines are the calculations according to the equation 3.3 and the Raman tensors 3.4 and 3.5. (d) normalized intensity of I_{2D}/I_G is calculated as a function of θ_S and θ_L, according to equation 3.3.

in the 2D band are strong functions of the relative angle between the momenta of electron and the phonon involved [119]. Therefore, if one uses a specific polarization of the incident laser, electrons with a specific momentum will excite first. Then, after this electron-phonon scattering process, electrons with another specific momentum scatter off and emit photons with specific polarization due to the nodal structures of optical transition matrix of graphene. Hence, the Raman intensity at the 2D band frequency change significantly when the angle between the polarizations of incoming and outgoing light are varied.

3.5 Conclusions

After a brief introduction, the angular distribution of the G and 2D Raman scattering from graphene on glass were experimentally obtained by detecting back focal plane patterns. Calculations showed that the G Raman emission can be described by a superposition of two incoherent orthogonal point dipoles oriented in the graphene plane. Due to double resonant Raman scattering, the 2D emission can be represented by the sum of either three incoherent dipoles oriented 120° with respect to each other. While the G scattering is confirmed to be nonpolarized, in the case of the 2D band polarized scattering is observed. The polarization contrast is found to decrease substantially for increasing collection angle, due to polarization mixing caused by the air-dielectric interface. This also influences I(2D)/I(G), a crucial quantity for estimating the doping in graphene.

The treatment of the depolarization and the corresponding expression derived for calculating the polarized Raman scattering intensities in equation 3.7 is expected to be applicable to a wide range of samples including other layered materials, carbon nanotubes, or nanowires [120].

These results are thus important for the quantitative analysis of the Raman intensities in confocal microscopy, where the influence of the objective's numerical aperture can not be longer neglected. In addition, they are relevant for understanding the influence of signal enhancing plasmonic antenna structures, which typically modify the sample's radiation pattern, as will be shown in the next chapters.

Chapter 4

Tuning emission characteristics with optical antennas

Optical antennas allow to manipulate and control optical radiation at the nanoscale [121]. This technology holds promise for enhancing the performance and efficiency of photodetection [122, 123], light emission [124, 125], sensing and biosensing [126, 127, 128], spectroscopy [129] and microscopy [130, 131], among other applications. For metallic antennas particularly strong local fields can result in the optical regime from localized surface plasmon (LSP) resonances. After a review on optical antennas, with a special focus on tip-enhanced near-field microscopy (TENOM) in section 4.1, an introduction to the field of plasmonics is provided in section 4.2. Plasmonics is concerned primarily with the manipulation of light at the nanoscale, exploiting both localized and SPPs for sensing and waveguiding applications [132]. Examples of the ability of antennas to redirect radiation by employing propagating and localized surface plasmon, supported by gold dimer antennas and silver nanowires, are shown in section 4.3.

4.1 Optical antennas

The present section is based on the publication "*Advances in Tip-Enhanced Near-Field Raman Microscopy Using Nanoantennas*" by Xian Shi*, Nicolás Coca-López*, Julia Janik, and Achim Hartschuh. Chemical Reviews, 117 (7), pp 4945-4960, 2017. [1]

This section provides an account of the basic concept and parameters associated with optical antennas with a special emphasis on the context of tip-enhanced near-field microscopy. While all definitions hold for optical antennas in general, the discussion is centered on the out-of-plane optical antennas used in TENOM, in contrast to in-plane antennas [133].

[1] * X.S. and N.C.L. contributed equally to the manuscript.

4.1.1 Introduction: Tip-enhanced Near-Field Optical Microscopy

Since the first reports about almost 20 years ago, tip-enhanced near-field optical microscopy (TENOM) continuously developed and is now a powerful technique capable of producing high-spatial resolution optical images combined with strong signal enhancement. This development has been followed by a number of review articles [129, 134, 14, 135, 136, 137, 138, 139, 140, 141, 142]. Tip-enhanced near-field optical microscopy exploits the local signal enhancement obtained at the apex of a metallic tip to form high-resolution images of surfaces by raster-scanning it over a sample.

Due to its direct connection to tip-enhanced Raman scattering (TERS), surface enhanced Raman spectroscopy (SERS) and plasmonics in general, TENOM has benefited strongly from the enormous developments in these areas. Examples include the development of the concept of optical antennas, the design and application of novel antenna structures and the theoretical modeling of the resulting plasmonic near-fields. In addition, the greatly improved nano-fabrication capabilities enable the realization of new nanoantenna designs usable in a scanning-probe approach [143, 144, 145]. These developments were accompanied by the improving understanding of the nano-optical fields at very short length scales and different signal enhancement mechanisms.

The present section begins with the discussion of the physical principle of optical nanoantennas. It continues discussing the antennas' electric near-field distribution, which is commonly understood to determine the spatial resolution in TENOM. The quantum plasmonic and atomistic effects presumably behind the unexplained subnanometer resolution obtained in recent TERS experiments are reviewed. Finally, the mechanisms contributing to the signal enhancement of different optical sample responses including Raman scattering, fluorescence, generation of photocurrent and electroluminescence, are discussed.

4.1.2 Principles of optical antennas

Characteristics of an optical antenna

An optical antenna is defined as an object that converts free-propagating optical radiation to localized energy and vice versa [143, 144, 145, 146] (see Figure 4.1(a)). This localized energy can be used to optically excite a receiving object that is in the near-field of the antenna's feed point leading to enhanced absorption of radiation. Conversely, energy released by a transmitting object can be radiated more efficiently. More concretely, the antenna's function is to efficiently couple its near-field to the far-field, in which the laser source and the detector are located. Tip-enhanced near-field microscopy exploits this extremely short-ranged near-field interaction between its tip, which acts as an optical antenna, and the sample (see Figure 4.1(b)). For a comprehensive characterization of an optical antenna, classical antenna theory can be used. To simplify the description of the antenna parameters, a dipole-like behavior of receiver and transmitter is typically assumed.

Two antenna enhanced processes, namely absorption and emission of light, have to be considered in order to get a complete description of the optical antenna function. Enhanced absorption can be quantified in terms of the antenna aperture A, which corresponds to the

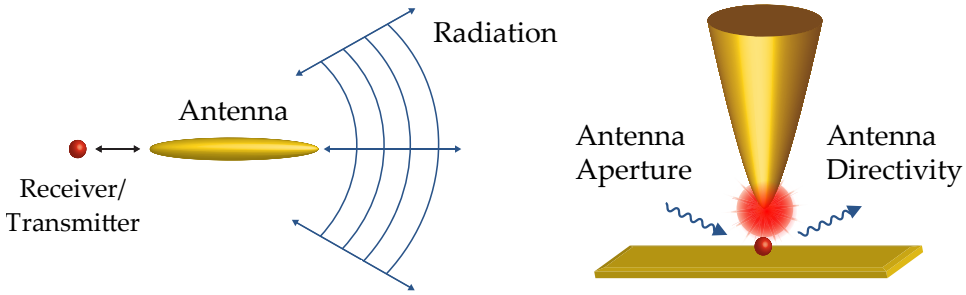

Figure 4.1: Left: Optical antennas convert free propagating electromagnetic radiation in the far-field to strongly localized near-fields and vice versa. Right: The optical antenna can be described by its functional parameters aperture and directivity. Both parameters typically depend on the frequency of the incident and the scattered light. From a functional perspective, the antenna is formed by both the scanning probe and the sample substrate. Adapted from reference 129.

absorption cross section σ in presence of the antenna. It describes the efficiency with which the incident radiation is captured to excite the receiver with the power P_{exc}, where I is the intensity of the radiation with the polarization $\mathbf{n}_{pol}$ incident from the direction (θ, ϕ) corresponding to $A(\theta, \phi, \mathbf{n}_{pol}) = {}^{P_{exc}}/_{I} = \sigma_A(\theta, \phi, \mathbf{n}_{pol})$. The antenna enhances the field at the absorber, and by defining the field in its absence as $\mathbf{E}_0$ and in its presence with $\mathbf{E}$ the absorption cross section then becomes

$$\sigma = \sigma_0 \frac{|\mathbf{n}_p \cdot \mathbf{E}|^2}{|\mathbf{n}_p \cdot \mathbf{E}_0|^2} \tag{4.1}$$

Here $\mathbf{n}_p$ is the orientation of the absorption dipole and the subscript '0' indicates the absence of the antenna. Equation 4.1 shows that the absorption process depends on the incident direction and polarization of light. Neglecting their vectorial character or assuming the same direction of enhanced and non-enhanced fields, the absorption enhancement can then be expressed by the local field enhancement factor $f = E/E_0$ as $\sigma/\sigma_0 = f^2$. For metallic nanoantennas, particularly strong local fields can result in the optical regime from localized surface plasmon resonances, collective electron oscillations that are controlled by their shape and their material composition (see section 4.2.2).

A practical way to characterize the enhanced emission is the antenna efficiency, which is defined in equation 4.2. It describes the ratio between the total power dissipated by the antenna P and the radiative power P_{rad}. The total power P is composed of P_{rad} and the power dissipated through other channels, for example heat, P_{loss} [145].

$$\epsilon_{rad} = \frac{P_{rad}}{P} = \frac{P_{rad}}{P_{rad} + P_{loss}} \tag{4.2}$$

The antenna's ability to emit the radiated power into a certain direction can be measured by the directivity D. It considers the angular power density $p(\theta, \phi)$ with θ and ϕ as

the angles of the direction of observation following $D(\theta,\phi) = (4\pi/P_{rad})\, p(\theta,\phi)$. By taking the polarization into account one can define the partial directivities as

$$D_\theta(\theta,\phi) = \frac{4\pi}{P_{rad}} p_\theta(\theta,\phi), \quad D_\phi(\theta,\phi) = \frac{4\pi}{P_{rad}} p_\phi(\theta,\phi) \tag{4.3}$$

with p_θ and p_ϕ as normalized angular powers.

The antenna gain G combines the efficiency and directivity of an antenna to yield the radiation relative to the total power as $G(\theta,\phi) = \epsilon_{rad} D(\theta,\phi)$.

Absorption and emission at the same optical frequency can be connected following the reciprocity theorem. This leads to a connection between the excitation rate Γ_{exc} and its spontaneous emission rate Γ_{rad}.

$$\frac{\Gamma_{exc,\theta}(\theta,\phi)}{\Gamma^0_{exc,\theta}(\theta,\phi)} = \frac{\Gamma_{rad}}{\Gamma^0_{rad}} \frac{D_\theta(\theta,\phi)}{D^0_\theta(\theta,\phi)} \tag{4.4}$$

The index θ refers to one polarization state, but can also be denoted by ϕ, which corresponds to a rotation of the polarization by 90°. Neglecting the vectorial character, the spontaneous emission rate enhancement can be expressed by the local field enhancement factor $f = E/E_0$ as $f^2 = \Gamma_{rad}/\Gamma^0_{rad}$, corresponding to the relation for the absorption rate enhancement $f^2 = \Gamma_{exc}/\Gamma^0_{exc}$. Various studies have investigated the field enhancement factor for different antennas and configurations, and values ranging from $f = 2-5$ for single spherical particles up to 1000 for optimized antennas have been reported [147, 148, 149, 150].

Importantly, the discussed antenna parameters will show a pronounced frequency dependence in most cases, that can vary substantially between the incident and the emitted frequencies. Examples include resonant antenna structures that feature distinct spectral modes such as metallic nanospheres, nanorods, dimers, bowtie antennas, etc.

In general, three different contributions to the local field enhancement provided by an optical antenna are currently being discussed. First, the lightning rod effect which is due to the geometrical singularity represented by the tip and leads to the spatial confinement of the surface charge density at the apex of a tip or tip-like structure [151]. This process is essentially non-resonant and will depend primarily on the electrical conductivity of the tip material at the frequency of light used in the experiment. Second, the excitation of localized surface plasmon resonances (LSPRs) in metallic nanostructures such as nanospheres and nanorods which depends on the frequency of incident and Stokes-scattered light (see section 4.2.2). And third, length related antenna resonances that occur if the length of the antenna is a multiple of half the wavelength of light. At optical frequencies metals are not perfect conductors and therefore, an effective scaling relation has to be used to connect the effective wavelength λ_{eff} with the incident wavelength λ. The effective wavelength shows a linear behavior with the plasma wavelength of the metal λ_p and $n_{1,2}$ as constants that depend on geometry and dielectric properties $\lambda_{eff} = n_1 + n_2\,(\lambda/\lambda_p)$ [152].

Near-field of optical antennas

The antenna's near-field distribution determines the signal enhancement, and in TENOM experiments, also the spatial resolution and the observed image contrast. In general, the enhanced fields of the optical antenna are highly dependent on the shape, material composition and structure of the used antenna-substrate system. In most cases, the resulting near-field distribution is strongly non-uniform regarding magnitude and polarization as well as phase. Numerous theoretical studies have been performed to characterize the field distribution and the corresponding enhancement for different conditions [153, 154, 155, 156, 157].

The parameters in the aforementioned subsection show that the field enhancement factor depends on the directivity D and the polarization of the incoming light. For semi-infinite cone-like tip structures, as the typical structure used for antennas in TENOM (see figure 4.2(a)), the field enhancement is highest when the polarization is parallel to the long axis of the cone [153, 158, 155]. But the tip also modifies the polarization with respect to the incoming field. Figure 4.2 shows the simulated distribution of the z and x components of the field enhancement in the (xy) plane. Here, the heterogeneity of the near-field becomes visible. While the z component (figure 4.2(c)) is highly localized beneath the tip, the x component (Figure 4.2(b)) shows two weaker lobes. Especially the in-plane modes result in a spatially heterogeneous polarization which can complicate the contrast formation.

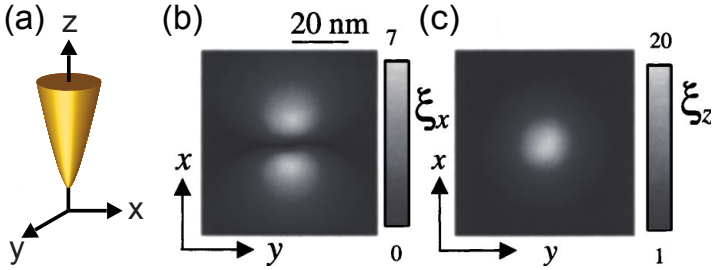

Figure 4.2: (a) System of reference for the x (b) and z (c) component of the field enhancement $\xi_{x,z} = |E_{x,z}|/|E_0|$ on the substrate plane ($z = 0$) for a silver tip with resonant excitation ($\lambda = 505$ nm) and a tip-substrate distance of 2 nm calculated by Demming et al. [154].

For dielectric sample substrates, the confinement of the local fields reflects the geometrical size of the tip. Since the Raman enhancement scales approximately with the fourth power of the field enhancement (see subsection 4.1.3), the spatial resolution obtained in a TERS experiment on dielectric substrates is typically somewhat smaller than the topographic resolution [130, 138]. Given that the tip's near-field decays exponentially with the distance between tip and substrate, this separation has to be taken into account and should be as short as possible. An increase in tip-substrate distance will lead to weaker fields and a loss in resolution and enhancement [159, 156]. As an example, Raman signal enhancement factors for samples on dielectric surfaces are in the range of $10^2 - 10^7$ [136].

The situation is different for other tip-enhanced signals. Non-radiative transfer of energy from the electronically excited molecule to the metallic antenna followed by non-

radiative dissipation in the metal has to be taken into account when the separation between the emitter and the metallic antenna is small [160, 161]. This is typically the case for TENOM experiments, in which this separation is below 10 nm. This additional non-radiative relaxation channel reduces the number of detected fluorescence photons. So, in contrast to the classical understanding of TERS, smaller separation between emitter and antenna does not result in higher performance. Rather, there is a distance dependent interplay between competing enhancement and quenching processes [162, 147, 163, 143, 164, 165, 166].

The role of the substrate and Gap mode configurations for TERS experiments

For dielectric sample substrates, the spatial resolution observed in TENOM is mostly determined by the geometrical size of the tip and the tip-sample distance, which defines the lateral extent of the enhanced fields (10 - 20 nm) [130, 167, 168, 169]. From a functional perspective, on the other hand, the concept of an antenna as a (metal) structure that converts free-propagating optical radiation into localized energy and vice versa, can directly be extended to include also the sample substrate. Of particular importance for TERS are the so-called gap mode configurations (for example, see references 170, 171, 172, 173, 174), in which the tip is placed above a metallic sample substrate separated by an extremely small gap distance on the order of one nanometer. Upon illumination of the tip with a focused laser beam, a surface charge density is induced in the tip apex which can be approximated by a point dipole. Because of the proximity of tip and metal substrate, mirror charges are accumulated at the surface of the metal substrate that can be described by an image dipole [175]. Upon approaching the tip, both the tip apex plasmon mode and the surface plasmon modes cease to exist independently, and a new hybrid mode forms, the so-called gap plasmon mode [174] (see Figure 4.3).

Compared to dielectric substrates that do not support the formation of a gap mode, far stronger confinement of the field is obtained in the case of metallic substrates, leading to substantially improved spatial resolution [157, 176, 136, 174](see Figure 4.3). At the same time, far higher field enhancement factors can be achieved, which relates to the well known observation in SERS that large enhancements are observed for interstitial sites and small nanogaps, for instance, in metal particle dimers [177, 178, 179]. As a result, gap mode configurations can be used to confine light to dimensions which are not limited by the diameter of the tip.

The lateral confinement of gap plasmons was estimated for tunnel junctions between taper probes and flat surfaces [180]. According to this rule, the lateral confinement w= $A\sqrt{Rd}$ is proportional to the square root of both the probe's apex radius of curvature R and the gap separation d (see Figure 4.3). Therefore, for $d = 0.5$ nm (at the limits of the classical electrodynamics regime, see below), a lateral optical resolution of better than 2.5 nm appears feasible, since tapers with $R \leq 5$ nm are now achievable [174]. For smaller distances, the onset of quantum tunneling sets a lower limit on w, reaching a minimum at about $d \approx 0.3$ nm (see below) [181].

While the gap mode configuration is clearly advantageous with respect to optimum spatial resolution and detection sensitivity, its applicability is expected to be limited to

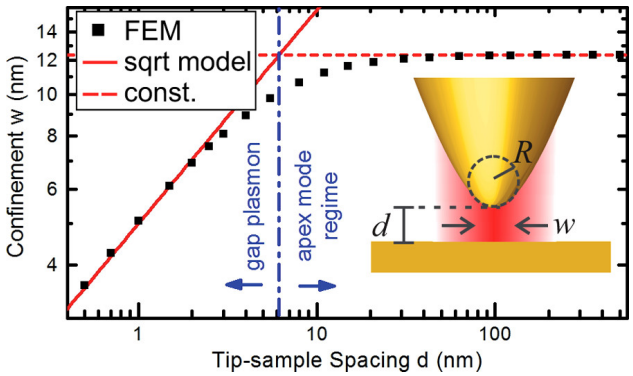

Figure 4.3: Lateral confinement w of the intensity $|E|^2$ obtained as full width at half-maximum from cross-sections through simulated field patterns 0.2 nm away from the apex for different tip-sample spacings d. Asquare root model for the gap plasmon extent, w= $A\sqrt{Rd}$, was fitted to the data with tip - sample spacing $d \leq 2$ nm, shown as the solid red line. For $R = 10$ nm an optimum value of $A = 1.57$ is found. The red dashed line represents a constant fit to the data with tip - sample spacing $d \geq 100$ nm. Adapted from references 174 and 129.

extremely thin sample materials with thickness below 10 nm that allow for substantial coupling between tip and substrate plasmons.

Quantum and atomistic effects

A major question in TERS yet to be solved is, whether there is a physical limit to the spatial confinement and the enhancement of the electromagnetic field generated by the nanoantenna. From the classical electrodynamic description of TERS, both electrical field enhancement and confinement are predicted to continuously increase upon decreasing the tip-sample distance. This would suggest the simple rule that for improving spatial resolution and signal enhancement the distance needs to be reduced. However, as the distance enters the nanometer and then the subnanometer range, the quantum nature of the electrons will become important, which can significantly alter the plasmonic response of the system [182].

Specifically, quantum mechanical treatments, such as the jellium model, show that the probability density of electrons extends outside of metal surfaces decaying exponentially with distance [183, 184]. This spill-out of electrons allows for electron tunneling across junctions at separations smaller than ≈ 1 nm thereby quenching the local field enhancement provided by the gap plasmon [182]. At the same time, a charge transfer plasmon can form with different spectral characteristics.

Another quantum phenomenon that could influence the plasmon resonance is the nonlocal screening of electric fields. Nonlocal screening [185] refers to the fact that, because of electron - electron interactions, the motion of the conduction band electrons at a given point in space depends not only on the field applied at that position but also on fields at

other locations [182]. The nonlocal screening prevents sharp charge localization at interfaces, thus reducing the field enhancements even further, relative to classical results. This effect is important for small particles [186] and narrow gaps [187].

In the case of gap configurations, electron spill-out and the associated non-local screening will create an "effective" gap distance that also differs from the geometrical value (see reference 182 and references therein). For gap distances of less than 1 nm, electron tunneling across the gap at optical frequencies will further modify the plasmonic response of the system with respect to the classical description. Due to the screening of localized surface charges by quantum tunneling and a consequent reduction in the plasmonic coupling, the resonances shift towards blue. This phenomenon explains the observed smooth transition of the plasmonic response upon variation of the geometry from a subnanometer gap to touching metal surfaces and has been extensively studied for the case of plasmonic dimers [182]. Electron tunneling provides an effective "charge transfer" channel, neutralizing the bonding-plasmon-induced charges of opposite signs across the gap and thus quenching the field enhancement [188]. Moreover, such electron tunneling implies a resistance that broadens the plasmon resonances. As the bonding modes vanish, charge transfer plasmons (CTPs) are established because the two nanoparticles forming the plasmonic dimer are conductively connected through electron tunneling [189, 181]. This has important consequences for TERS because electron tunneling at the optical frequency is expected to efficiently quench the plasmonic near-field enhancement for extremely small distances, thus limiting the achievable signal enhancement [190].

Besides the quantum nature of electrons, also the detailed atomistic structure of the tip and the sample substrate will become relevant on nanometer and sub-nanometer length scales. Using Sodium clusters as example, Barbry et al. presented TDDFT calculations, in which atomic-scale features are taken into account together with the nonlocal screening of conduction electrons [191]. The authors found that atomic features such as protruding atoms do localize electromagnetic fields down to atomic-scale dimensions, showing resonant (plasmonic) and nonresonant (lightning rod effect) field enhancement and beating the typical plasmonic confinement imposed by the nanoparticle size. Trautmann and coworkers suggested that these protrusions, when appearing on a bigger and smoother structure, might act as probing tips [192]. However, in large plasmonic systems, the presence of these subnanometric extremely localized 'hot spots' may only weakly affect the effective localization area, since this will be dominated by the overall plasmonic field structure in the gap [191].

In summary, both quantum and atomistic effects are expected to determine the plasmonic response, i.e. field confinement and enhancement, at extremely small distances. While the quantum phenomena discussed above are expected to limit the field enhancement and confinement and thus the observed Raman enhancement in general, atomic-scale features appear to have the potential to reverse this effect. Atomistic features at both the tip and the substrate surface will have limited stability in particular at room temperature such that subtle morphological changes could give rise to substantial variations of the plasmonic properties of the antenna over time [193]. The same could be expected for the short ranged quantum phenomena. At present, the details of the interplay between quantum

and atomistic effects and their actual contribution to the spatial resolution and signal enhancement observed in the experiment is not fully clear yet.

4.1.3 Signal enhancement

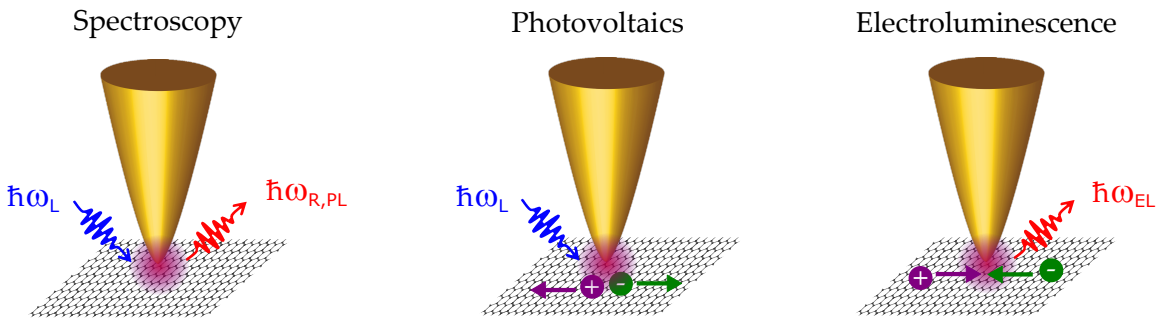

Figure 4.4: Optical antennas formed by metal nanostructures efficiently convert propagating radiation into localized energy in a nearby object. Conversely, localized energy is coupled to propagating radiation. Applications of antenna enhancement: (a) optical spectroscopy, (b) photovoltaics and (c) electroluminescence. Adapted from references 143, 9, 194.

As discussed in the previous subsection, it is the antenna function of a tip that enhances the optical response of the sample by increasing both the excitation and the spontaneous emission rate. The following discussion shows how distinct photo-physical sample responses, including photo-induced light emission (e.g. Raman, photoluminescence), photovoltaic responses (e.g. photocurrent) and electrically driven light emission (e.g. electroluminescence), can be enhanced using optical antennas (see figure 4.4) [9]. During the scope of this thesis, the first two processes were investigated.

Antenna-enhanced Raman Scattering: SERS and TERS

In the case of spontaneous Raman scattering, the detected signal depends on the product of the transition rates $\Gamma_{exc,\theta}(\theta,\phi)\,\Gamma_{rad}$, the directivity $D_\theta(\theta,\phi)$ and the detection efficiency $\eta_\theta(\theta,\phi)$ of the experimental setup. Furthermore, all these quantities will be wavelength dependent. The total signal at a given wavelength then results from angular integration

$$S_{Raman,\theta} = 1/(4\pi) \int_0^{2\pi} \int_0^{\pi} \Gamma_{exc,\theta}\,\Gamma_{rad}\,D_\theta\,\eta_\theta\,\sin\theta\,d\theta\,d\phi. \tag{4.5}$$

The ϕ integration can be limited to the maximum collection / detection angle $\phi_m = \arcsin(NA/n)$ determined by the numerical aperture NA of the microscope objective and the refractive index n of the enclosing medium. In the experiment the excitation profile and the angular detection range of the optical microscope should match the antenna aperture and directivity [138, 195].

Antenna-enhanced Raman spectra can differ substantially from their far-field counterparts. In both cases, the emission spectrum reflects the spectrally varying spontaneous emission rates Γ_{rad} connecting the same virtual state to different final vibrational states. Following the discussion in sec. 4.1.2 and noting the frequency dependence of the antenna gain G, the antenna can thus substantially modify the spectral shape of emission. In case of sharp antenna resonances and emission with large spectral bandwidth this will become particularly relevant.

Often, the angular and polarization dependence in equation 4.5 is neglected together with the vectorial character of the electric fields (equation 4.1). As a consequence, the total signal enhancement M is found to scale approximately with the fourth power of the field enhancement for small differences between the excitation and emission wavelength, assuming that the field enhancement at the tip does not depend sensitively on the wavelength.

$$M_{Raman} \approx \Gamma_{exc}/\Gamma^0_{exc}\,\Gamma_{rad}/\Gamma^0_{rad} \approx f^4 \tag{4.6}$$

For the general case of surfaced enhanced Raman scattering (SERS), Raman enhancement factors are reported reaching up to 12 orders of magnitude for colloidal particles, rough metal films and particular multiple particle configurations involving interstitial sites between particles or outside sharp surface protrusions [177, 178, 179]. Since the signal scales approximately with the fourth power, even a moderate local field enhancement, predicted for a single spherical particle to be in the range of $f \approx 2-5$ [177, 4] depending on its size and composition, is sufficient for significant signal enhancement. Overviews about the reported field enhancement and signal enhancement factors for different TERS configurations are given in references 138, 136, 172.

A semiquantitative analysis of the signal levels that can be expected in TERS from different sample materials and in different experimental geometries was given in reference 195. The authors discussed how high a signal level could actually be expected within the physical limitations set by field enhancement, damage threshold, tip scattering efficiency, collection and detection efficiency, and the Raman scattering cross section of the sample material for different experimental configurations.

More recently, the signal enhancement in TERS and SERS again became a topic of great interest presumably because of the improved theoretical understanding of the electric fields on very short length scales in the context of quantum plasmonics (see subsection 4.1.2) and triggered by the ground-breaking results achieved in reference 173. Here, both the achieved sub-nanometer spatial resolution and the observed non-linear power dependence of the Raman signal could not be directly explained by conventional electromagnetic models. This fact triggered the theoretical study of new developments that go beyond the f^4-rule. Some of this newly proposed mechanisms are:

- Optomechanical coupling [196, 197], in which the antenna and the Raman scatterer are no longer treated as two independent entities, but rather emphazising the coupling between them.

- Electric field gradient [198, 199, 200], in which the ultra-high spatial resolution of TERS can be partially attributed to the influence of an electric field gradient associated with strongly localized fields on the Raman response.

- Self-interaction [201, 202], in which the authors attributed the subnanometer resoluion achieved in Raman mapping to the strong optical coupling of the molecule with its plasmonic nanogap environment via multiple elastic scattering.

At present, the origin of the subnanometer spatial resolution in TERS is still under discussion and the relevance of quantum plasmonic and atomistic effects as well as of the newly proposed mechanisms for the signal enhancement has yet to be clarified.

Antenna-enhanced fluorescence

In contrast to antenna-enhanced Raman scattering, the antenna-enhanced fluorescence is determined by the excitation rate Γ_{exc} and the quantum yield q denoting the probability of a radiative decay, expressed in terms of the radiative rate and the non-radiative rate as $q = \Gamma_{rad}/(\Gamma_{rad} + \Gamma_{nonrad})$. As in Raman scattering, the excitation rate enhancement scales with f^2. The total signal enhancement can be expressed as:

$$M_{flu} \approx \frac{\Gamma_{exc}}{\Gamma^0_{exc}} \frac{q}{q^0} \approx f^2 \frac{q}{q^0} \tag{4.7}$$

Again, this simplified form neglects the orientation and polarization dependence of the transition rates and of the detection sensitivity together with the vectorial character of the electric field.

From equation 4.7 it is clear that antennas work most efficiently for samples with small intrinsic fluorescence quantum yield q^0 such as e.g. semiconducting single-walled carbon nanotubes and fullerenes [203, 204]. If $q << 1$, as is the case for very low quantum yield emitters, the radiative rate can be neglected compared to the non-radiative rate, so $q = \Gamma_{rad}/\Gamma_{nonrad}$ and

$$M_{flu} \approx \frac{\Gamma_{exc}}{\Gamma^0_{exc}} \frac{\Gamma_{rad}}{\Gamma^0_{rad}} \approx f^4 \tag{4.8}$$

as in the case of Raman scattering. For highly fluorescent samples, such as dye molecules, on the other hand, the quantum yield is already close to its maximum $q^0 \approx 1$ and cannot be enhanced further. In this case, the fluorescence enhancement will only reflect the excitation rate enhancement as

$$M_{flu} \leq \frac{\Gamma_{exc}}{\Gamma^0_{exc}} \tag{4.9}$$

where the sign $\leq$ accounts for possible quenching.

As discussed for TERS, the spectral dependence of the antenna gain can lead to a significant modification of the shape of the emission spectrum [163]. The influence of the

antenna directivity and the resulting spatial redirection of emission, as well as the influence of the dielectric substrate, has been studied for different antenna types [163, 31, 33]. To these regards, back focal plane imaging has proved to be a very useful tool (see section 4.3.2)[50].

Antenna-enhanced photocurrent and electroluminescence

Photocurrent and electroluminescence microscopy provide insight into the optoelectronic properties of materials by probing correlated optical and charge carrier transport phenomena. Photocurrent and electroluminescence responses are expected to benefit only from excitation rate and emission rate enhancements, respectively (see sketch in figure 4.4), and should thus scale with the square of the local field enhancement factor f:

$$M_{PC} \approx \frac{\Gamma_{exc}}{\Gamma^0_{exc}} \approx f^2, \; M_{EL} \approx \frac{\Gamma_{rad}}{\Gamma^0_{rad}} \approx f^2 \tag{4.10}$$

Compared to antenna-enhanced Raman scattering and photoluminescence, this should lead to weaker enhancement and lower spatial resolution [205] for the cases of tip-enhanced photocurrent and electroluminescence.

The field enhancement factor f is not constant, but actually depends on the position with respect to the tip end. If f_0 is the maximum field enhancement factor given by a tip, and this tip is assumed to be radially symmetric, the distance dependence of f can be approximately described by a Gaussian function:

$$f(r) = f_0 \cdot e^{-\frac{r^2}{2w^2}} \tag{4.11}$$

where r is the distance and w is the peak width, fixed for given tip-sample configurations. When the signal enhancement scales with $M \approx f^4$, as in the case of Raman scattering or photoluminescence, the intensity is $I_{Raman/PL} \propto f^4$ and therefore $I_{Raman/PL} \propto e^{-4\,r^2/2w^2}$. This means that the Raman/PL signal peak width is $w_{Raman/PL} = 1/2\,w$. When the signal enhancement scales with $M \approx f^2$, as in the case of photocurrent or electroluminescence, the intensity is $I_{PC/EL} \propto f^2$ and therefore $I_{PC/EL} \propto e^{-2\,r^2/2w^2}$. In this case, the PC/EL signal peak width is $w_{PC/EL} = 1/\sqrt{2}\,w$. It then turns out that $w_{PC} = \sqrt{2}\,w_{Raman}$, meaning that the spatial resolution of the Raman signal is $\sqrt{2}$ times better than that of the photocurrent signal, as experimentally shown by Nina Mauser and colleagues [194, 205, 138].

4.2 Plasmonics

The field of plasmonics studies the optical phenomena related to the electromagnetic response of metals and it is mostly concerned with the control of optical radiation on the subwavelength scale [4]. This section is dedicated to the fundamental of plasmonics. After an introduction about propagating surface plasmons polaritons (SPPs), its dispersion relation and excitation techniques are presented. Finally, localized surface plasmons (LSPs) are introduced.

4.2.1 Propagating surface plasmon polaritons

Fundamental properties of propagating SPPs

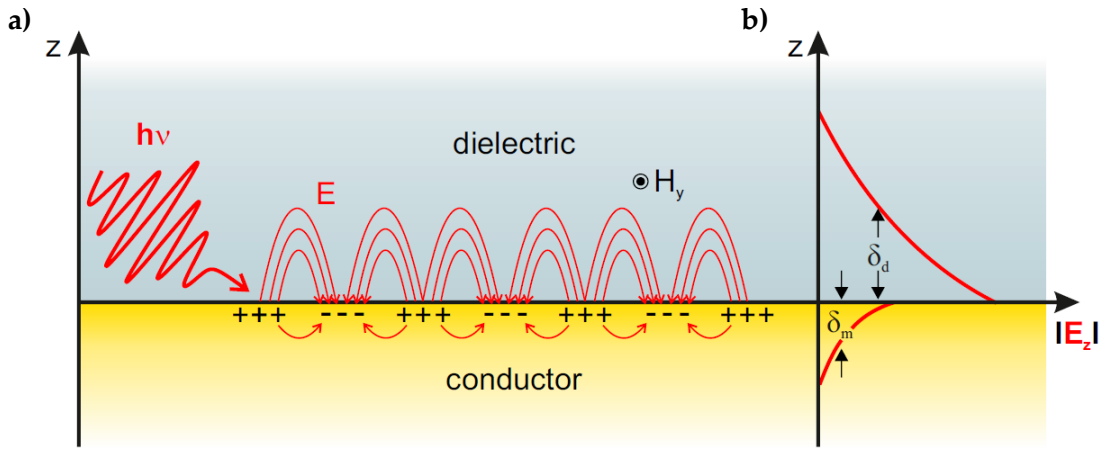

Figure 4.5: Surface plasmons propagating along a metal-dielectric interface. (a) Propagating plasmons as a combination of longitudinal charge oscillations and an electromagnetic wave. (b) Absolute value of the z component of the electric field as a function of z. The red lines depict the extent of the electric field into the dielectric and conductor. Adapted from reference 206.

Propagating surface plasmon polaritons (SPPs) are electromagnetic waves coupled to the surface oscillations of free-electrons in a metal, which travel along a metal-dielectric interface. Figure 4.5(a) presents a schematic representation of a SPP wave propagating in the x direction at the interface between a metal ($z < 0$) and a dielectric ($z < 0$). A photon with energy $E = \hbar\omega$ induces a collective oscillation of the free electrons in the metal, represented by the charge symbols. The originated electromagnetic field is transverse magnetic in character (H is parallel to the y direction) and requires an electric field normal to the surface (pictured as red lines) [5].

Because plasmons are bound to the interface, the z component of the electric field decays evanescently with increasing distance to the interface. SPPs propagating at the metal-dielectric interface travel mainly in the dielectric, as schematically indicated by the

number and height of the electric field lines in figure 4.5(a). This is also illustrated in figure 4.5(b), where the exponential dependence of the field amplitude $|\vec{E}_z|$ in the direction of z into the two different media is shown, together with the skin depths for the dielectric, δ_d, and the metal, δ_m, with $\delta_d >> \delta_m$ (see below).

The dispersion relation of propagating SPPs can be derived from Maxwell's equations for the system described above [5]: An electromagnetic wave propagating along a metal half-space with a complex dielectric function $\epsilon_m = \epsilon'_m + i\,\epsilon''_m$ adjacent to a dielectric medium with a real dielectric function ϵ_d, and with maximum electric field $|\vec{E}_z|$ at the interface, $z = 0$, and $|\vec{E}_z| = 0$ when $z \to \infty$. The dispersion relation for the x and z components are then given by:

$$k_x = \sqrt{\frac{\epsilon_m\,\epsilon_d}{\epsilon_m\,+\,\epsilon_d}}\;k_0 = \sqrt{\frac{\epsilon_m\,\epsilon_d}{\epsilon_m\,+\,\epsilon_d}}\;\frac{\omega}{c}, \tag{4.12}$$

$$k_{z,i} = \sqrt{\frac{\epsilon_i^2}{\epsilon_m\,+\,\epsilon_d}}\;k_0 = \sqrt{\frac{\epsilon_i^2}{\epsilon_m\,+\,\epsilon_d}}\;\frac{\omega}{c} \tag{4.13}$$

where $k_0 = \omega^2/c^2$ is the free-space wavevector and the i-subindex accounts for i = m, d, the metal and dielectric frequency-dependent permitivities, respectively.

From equations 4.12 and 4.13 follows that in order to obtain a solution propagating in the x direction and bound to the z direction, certain conditions must be fulfilled: $k_{z,i}$ has to be purely imaginary to ensure the evanescent, surface bound character of the wave in the z-direction and k_x needs to contain a real part, which allows propagation in the x-direction. The imaginary part of k_x describes the damping of the wave, due to ohmic losses in the metal [207]. For $k_{z,i}$ to be purely imaginary, the sum in the denominator of equation 4.13 must be negative ($\epsilon_m + \epsilon_d < 0$). For k_x to be real, it is implied from equation 4.12 that the multiplication of both dielectric constants must be negative ($\epsilon_m \cdot \epsilon_d < 0$). These conditions are, therefore, satisfied for the case of an interface between a dielectric and a metal. From here, it follows that the dielectric constant of one half space has to be positive and the other negative in order to fulfill both conditions simultaneously. This are exactly the conditions that are fulfilled for most metal-dielectric interfaces.

Figures of merit of the plasmonic fields

Following the previous results, some characteristic properties of SPPs can be discussed. Considering the metal's dielectric function as a complex number $\epsilon_m = \epsilon'_m + i\epsilon''_m$, losses associated with electron scattering (ohmic losses) can be accommodated. The adjacent medium is assumed to be a good dielectric with negligible losses, i.e. ϵ_d is a real number. Then, it naturally follows that the wavenumber is a complex number $k_x = k'_x + k''_x$. Under the assumption that $|\epsilon''_m| << |\epsilon'_d|$, the SPP wavelength can be calculated as $\lambda_{SPP} = 2\pi/k'_x \approx \lambda\sqrt{(\epsilon'_m + \epsilon_d)/\epsilon'_m\,\epsilon_d}$ [4], where λ is the wavelength of the excitation light in vacuum. Under the same assumption, the propagation length of the SPP along the interface can be determined by k''_m, which is responsible for an exponential damping of the electric field

amplitude. The $1/e$ decay length of the electric field is $1/k''_m$ or $1/(2k''_m)$ for the intensity. This damping comes from ohmic losses of the electrons participating in the SPP and finally results in a heating of the metal. Typical values of the propagation length are $L_{SPP} \approx 60\mu m$ for a silver/air interface and $L_{SPP} \approx 10\mu m$ a gold/air interface [4].

Since the wave-vector components of the SPP wave perpendicular to the surface are purely imaginary, the field amplitude in the z-direction decreases exponentially with an exponent $k_{z,i} = 1/\delta_i$. Where $i = m$, d and δ_i is the skin depth after which length the field is reduced to $1/e$, expressed as [207]:

$$\delta_i = \frac{1}{|k_{z,i}|} = \frac{\lambda}{2\pi}\sqrt{\frac{\epsilon'_m + \epsilon_d}{\epsilon_i^2}} \tag{4.14}$$

Given the dielectric function for a noble metal and a typical dielectric, it can be calculated that the field penetrates deeper into the dielectric than into the metal, as sketched in figure 4.5. Typical values for the penetration depths into the metal at visible wavelengths are $\delta_m \approx 24$ nm for silver and $\delta_m \approx 31$ nm for gold, further decreasing with increasing wavelength [207], while it is in the order of $\delta_d \approx 380$ nm in the dielectric region [207].

Dispersion relation

Energy and momentum conservation have to be fulfilled in order to excite propagating SPPs. Therefore, to see how this can be done, the dispersion relation of the surface waves, i.e. the relation between energy in terms of the angular frequency ω and the momentum in terms of the wave vector in the propagation direction k_x given by equation 4.12, must be analyzed.

Figure 4.6 shows the dispersion relation 4.12 of a SPP wave propagating in the x direction at the interface between a metal and a dielectric (red line), as sketched in figure 4.5, together with the light line in air $\omega = ck_x$ (blue line). The dielectric permittivity constant is assumed to be real, positive, and independent of ω, which is true for e.g. air ($\epsilon_d = 1$). Here, the dielectric function of the metal will be discussed in the context of the free-electron or Drude model [208]:

$$\epsilon_m(\omega) = 1 - \frac{\Omega_p^2}{\omega(\omega - i\Gamma_0)} \tag{4.15}$$

where $\Omega_p = \omega_p\sqrt{f_0}$ is the plasma frequency associated with intraband transitions with oscillator strenght f_0 and damping constant Γ_0. For silver, the plasma frequency $\omega_p = 9.01/\hbar$ eV, $f_0 = 0.845$ eV, and $\Gamma_0 = 0.048$ eV [208]. For a model with a more realistic dielectric function, including interband transitions, see references [4, 5, 209].

The dispersion relation shows three branches. The high energy branch, called Brewster mode, does not describe true surface waves, since according to 4.13 the z-component of the wave vector in the metal is no longer purely imaginary, and therefore no bound solutions exist [4]. The low energy branch corresponds to a true interface wave, the surface plasmon polariton (SPP). The word polariton intents to highlight the intimate coupling between

the charge density wave on the metal surface (surface plasmon) with the light field in the dielectric medium (photon).

There is a continuous transition from the surface plasmon dispersion into the upper high energy branch (dashed line). If the dispersion curve is followed starting from $\omega = 0$, it continuously moves from the light line towards the horizontal line determined by the surface plasmon resonance ω_{SP}. As the dispersion curve approaches this line the losses start to increase drastically. As a consequence, as ω is further increased the dispersion curve bends back and connects to the upper branch. In the connecting region the energy of the mode is strongly localized inside the metal which explains the high losses [4]. This experimentally verified [210] back-bending effect poses a limit to the maximum wave-number that can be achieved as $k_x \lesssim 2\omega/c$.

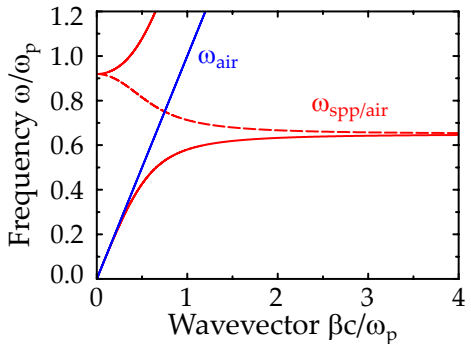

Figure 4.6: Dispersion relation of surface plasmon polaritons propagating along silver-air interface (red line) and the light line in air (blue line).

A very important feature of SPPs can be derived from the dispersion relation. Equation 4.12 implies that the momentum of the surface plasmon mode $\hbar k_x$ is always larger than that of a free-space photon of the same frequency, $\hbar k_0$. The light line asymptotically approaches the SPP dispersion relation at lower frequencies, but never intersects with it. For example, for a silver-air interface in the red part of the visible spectrum, the surface plasmon wave-vector is $k_x = 1.03\, k_0$, as calculated using equation 4.12 [211]. This increase in momentum of the SPP is associated with the strong coupling between light and surface charges [4]: The light field has to 'drag' the electrons along the metal surface. Therefore, a SPP on a plane interface can never be directly excited by light of any frequency that propagates in free space. Excitation of a SPP by light is only possible if the wave-vector of the exciting light can be increased over its free-space value.

Excitation techniques

In order to excite propagating SPPs, energy and momentum conservation have to be fulfilled. There exist several ways to bridge the momentum mismatch between light and surface plasmons of the same frequency. However, only the mechanisms related the work in this thesis will be introduced here.

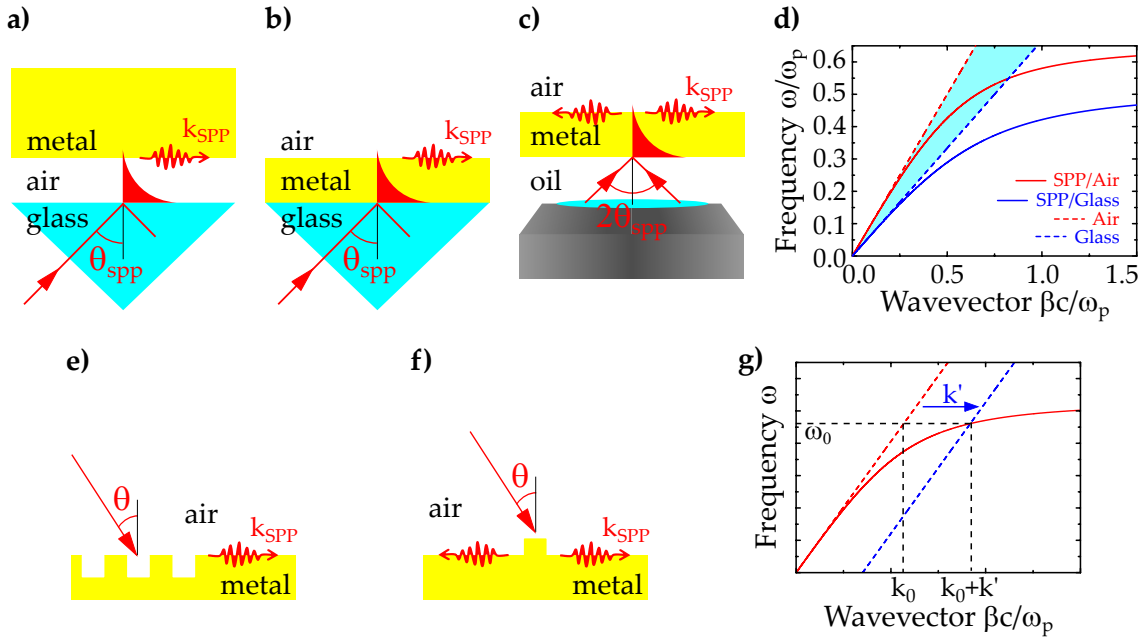

Figure 4.7: Overcoming the k-mismatch: Different approaches for SPP excitation. (a) Otto configuration. (b) Kretschmann configuration. (c) Kretschmann-like excitation with a high NA microscope oil immersion objective. (d) Dispersion relation of the SPPs involved in the configurations (a), (b) and (c). (e) Excitation via a grating coupler and a (f) localized scatterer. (g) Shifting of the light line by adding an extra momentum.

A possible solution involving freely propagating waves consist on illuminate through a medium with refractive index $n > n_{air}$, for example, a glass prism. A sketch of the possible experimental arrangements realizing this approach is shown in figures 4.7(a) and (b). The light line is then tilted by a factor of n since $\omega = ck/n$. Surface plasmons are then excite by means of the evanescent waves created at the interface between either glass and air or glass and metal. This situation is presented in figure 4.7(c), which shows the surface plasmon dispersion for a silver-air interface (red line) and a glass-silver interface (blue line), together with the free-space light lines on air and the tilted light line in glass (red and blue dashed lines, respectively).

In the Otto configuration [212] the tail of an evanescent wave formed at a glass prism-air interface in a total internal reflection geometry is brought into contact with a metal-air interface that supports SPPs (see sketch 4.7)(a). By adjusting the angle of incidence of the totally reflected beam inside the prism, the resonance condition for excitation of SPPs, i.e. the matching of the parallel wave vector component,

$$k_{SPP} = k_{glass}(\theta_{SPP}), \tag{4.16}$$

can be fulfilled, where $k_{glass}(\theta) = (\omega/c)\, n_{glass} \sin\theta$ and θ is the incident angle. The tuning region goes from the maximum dispersion $k_{glass}(\theta = 90^{\cdot})$ (blue dashed line) towards the light line $k_0(\theta = 0^{\cdot})$, as indicated by the blue light colored area in figure 4.7)(d). The SPPs with a dispersion within this region are referred as leaky modes, since they radiate into the higher refraction index substrate, coupling to a free propagating wave, whereas the modes with a dispersion with higher k_{SPP} values are referred to as bound modes [213].

For a small gap width between the glass prism and the metal, the SPPs rapidly decay radiatively by transforming the evanescent SPP field into a propagating field in the glass. On the other hand, for a too large gap width, the SPP can no longer be efficiently excited.

The Otto configuration proved to be experimentally very challenging, due to the need of controlling the tiny dielectric gap between interfaces. A more convenient experimental configuration was introduced in 1971 by E. Kretschmann, in which a thin metal film is directly deposited on top of the prism [214]. The geometry is sketched in figure 4.7(b). An evanescent wave created at the glass-metal interface penetrates through the thin metal layer, exciting a propagating surface plasmon at the metal-air interface. Here, similar arguments as for the Otto configuration apply. For a too thin metal film, the SPP will be strongly damped because of radiation damping into the glass. For a too thick metal film, the SPP can no longer be efficiently excited due to absorption in the metal.

For both the Otto and the Kretschmann configurations, the excitation of SPPs can be monitored by measuring the intensity of reflected light while tuning the angle of incidence into the glass prism. The SPP resonance condition, $\theta = \theta_{SPP}$, appears as a minimum in the reflection. In literature, this reflection measurement is often referred as attenuated total reflection (ATR) method [215]. Typical ATR measurement results can be in references [4, 5].

Two physical interpretations can be given for the occurrence of the minimum in the reflectivity curves [4]. First, the minimum can be explained as the result of destructive

interference between the totally reflected light and the light emitted by the SPP due to radiation damping. Second, the missing light can be assumed to have been totally converted to a bound plasmonic mode, carrying away the energy along the interface such that it cannot reach the detector anymore, appearing as a reduction of the reflection signal.

Excitation of SPPs can be also achieved by using a high numerical oil immersion objective as a substitute for the prism in the Kretschmann configuration [216, 5] (see figure 4.7(c)). The localized fields generating propagating SPPs are in this case originating from the tight focusing of a laser beam. The incident angles supplied in this way range up to the maximum collection angle θ_{max} given by the NA of the objective, and include the resonant angles responsible for SPP excitation at a metal-air interface. For a given wavelength, a resonant wave vector will be responsible for SPP excitation, while the others will be reflected or transmitted through the film [217]. The excitation of SPPs acts as a spatial filter by selecting two sets of diametrically opposed plane waves at incident angles $\theta = \pm\theta_{SPP}$ fulfilling the SPP dispersion relation [216, 218]. The SPP waves corresponding to $+k_{SPP}$ and $-k_{SPP}$ are excited everywhere due to the very nature of the plane waves. A standing wave dominates the SPP intensity distribution as a result of the interference between two counter propagating SPP waves [218, 219]. Since any sample fabricated on a microscope glass coverslip can be measure, this method proves to be more flexible than previous configurations. Its mainly limitation, when compared to the Kretschmann configuration, is the smaller range of accessible angles due to the limited NA of the objective.

In order to use a photon with momentum k_0, and energy $E = \hbar\omega$, for the generation of a SPP with the same energy, an extra momentum k' is needed, so the relation $k_{spp} = k_0 + k'$ is fulfilled, as sketched in figure 4.7(g). An alternative approach to excite SPPs supplying this k' is the use of a grating coupler [207, 220] or a localized scatterer [207, 221]. In the case of a grating coupler, the momentum mismatch between the free-space photon and the SPP is overcome by adding a reciprocal lattice vector of the grating to the free space wave-vector, as follows: $k_{SPP} = k_0 \sin\theta \pm ng$, where $g = 2\pi/a$ is the reciprocal lattice vector of the grating, a is the grating periodicity, and $n = 1, 2, 3, ...$ is the order of refraction (see figure 4.7(e)). Suitable values for the angle of incidence θ and the other listed parameters need to be chosen for each excitation wavelength in order to achieve the resonance condition with the SPP and the grating coupler [4]. Grating couplers have been used to launch SPPs on metallic tips for TERS applications [222, 223] or on plasmonic waveguides [224].

More generally, random surface roughness [207] or fabricated localized scatterers [221] on metallic films can also be used to provide the extra momentum needed for SPP excitation. Momentum components Δk are provided via scattering, so that the phase-matching condition $k_{SPP} = k_0 \sin\theta \pm \Delta k$ can be fulfilled. It must be noted that this condition implies that random surface roughness also constitutes an additional loss channel for SPP propagation via coupling to radiation [5].

Information about other approaches for SPP excitation can be found in, for example, references 4 and 5.

4.2.2 Localized surface plasmons (LSPs)

In contrast to propagating SPPs, localized SPs are non-propagating excitations of the conduction electrons of metallic nanostructures coupled to the electromagnetic field. These modes arise naturally from the scattering problem of a small, sub-wavelength metallic particle in an oscillating electromagnetic field. The curved surface of the particle puts an effective restoring force on the driven electrons, so that the resonance arising leads to amplification of the field in the near-field zone and inside the particle [5]. This resonance is called the localized surface plasmon resonance and depends on the electron density, effective mass, size and shape of the particle [225].

This resonance also affects the efficiency with which a metal nanoparticle scatters and absorbs light. The corresponding cross sections for scattering and absorption $\sigma_{scattering}$ and $\sigma_{absoprtion}$ can be calculated for a spherical particle [226] to

$$\sigma_{scattering} = \frac{8\pi}{3} k^4 a^6 \left| \frac{\epsilon_m - \epsilon_d}{\epsilon_m + 2\epsilon_d} \right|^2, \tag{4.17}$$

$$\sigma_{absorption} = 4\pi k a^3 Im \left[\frac{\epsilon_m - \epsilon_d}{\epsilon_m + 2\epsilon_d} \right] \tag{4.18}$$

where $k = 2\pi/\lambda$ is the wavevector of the surrounding medium and a is the radius of the particle. The sum of absorption and scattering is called extinction, an account for the power removed from the incident beam due to the presence of the particle. While $\sigma_{absorption}$ scales with a^3, $\sigma_{scattering}$ scales with a^6. Therefore, for large particles extinction is dominated by scattering whereas for small particles it is associated with absorption. Equations 4.17 and 4.18 show that for metal nanoparticles both absorption, scattering and consequently extinction, are resonantly enhanced when $Re(\epsilon_m) = -2\epsilon_m$ (Fröhlich condition) [226, 227]. In a different note, it is interesting to know that in a quasi monochromatic isotropic random light field, the Fröhlich condition leads to existence of Mock-Gravity forces between two identical nanoparticles [228]. Summarizing, the strong dependence of the resonance frequency on the dielectric environment results in a red-shift as ϵ_m is increased. It is for this reason that metal nanoparticles are ideal platforms for optical sensing of changes in refractive index. For gold and silver nanoparticles, the resonance falls into the visible region of the electromagnetic spectrum. Finally, a second consequence of the curved surface is that plasmon resonances can be excited by direct light illumination, so in contrast to propagating SPPs, no phase-matching techniques need to be employed.

4.3 Redirecting light with metallic nanoparticles

Apart from converting near-field to far-field radiation, optical antennas also have a strong directionality in their emission characteristics. Control of the emission direction of individual emitters can then be achieved by reversible coupling to an optical antenna. For maximum coupling, the angular emission of the coupled system is dominated by the dominant antenna mode regardless of the emitter orientation or its polarization emission

properties [31, 33, 34]. The resulting radiation pattern can be described by the radiation of the superposition of point dipole emitters. For TENOM configurations [129, 9] the radiating tip can then be modeled as a vertical dipole positioned on the long axis of the tip which usually coincides with the optical axis of the microscope [50, 33]. For in-plane configurations [133], the antenna radiation can then be modeled as an in-plane dipole [31, 34].

Because of the reciprocity principle [39], the radiating properties of the antenna reflect the optimum excitation conditions. In consequence, the optical antenna will be excited most efficiently when the polarization of the exciting laser matches the polarization of the emission of the antenna [50]. Therefore, the detection efficiency γ, as defined in chapter 2, also depends on the particular orientation of the antenna. Worth noticing is that the quantity $4\pi\gamma$ corresponds to the angular integral of the antenna directivity divided [33].

Back focal plane (BFP) imaging (see chapter 2) allows to quantify the angular distribution of emitted or scattered light by nanoscale objects by direct imaging of the radiation patterns in the back focal plane of a high-numerical-aperture objective lens. Besides determining the orientation of dipolar emitters [27], and therefore to model the photoluminescence [44, 28] and Raman scattering [29] from nanomaterials, BFP imaging also allows to image the change of the radiation patterns in emitters/scatterers induced by optical antennas [31, 33, 34] or plasmonic waveguides [229].

This section starts by giving an introduction to propagating SPPs in Ag nanowires and continues with the investigation of the angular elastic scattering radiation patterns from Ag NWs. Finally, the angular radiation emission patterns from quantum dot - gold dimers systems are compared with the ones from a quantum dot ensemble.

4.3.1 Redirecting elastic scattered light with Ag nanowires

Propagating SPPs in metallic nanowires

Single crystal silver nanowires (Ag NWs) on a dielectric interface behave similar to broadband unidirectional antennas for visible light, where the degree of directionality can be controlled through the nanowire radius and its dielectric environment [230]. Furthermore, metal nanowires are particularly interesting as fundamental building blocks for developing integrated subwavelength optical routing [231, 232], since SPP modes propagate in one direction while being strongly confined in the other two [233, 234]. By using chemically synthesized metal nanowires, the typically high propagation losses of plasmonic waveguides can be mitigated [235, 236], achieving propagation distances of tens of micrometers. Different routing functionalities based on stochastic complex arrangements [233, 237] or nanowire welding [238, 239, 240] have been recently developed. In addition, the possibility of simultaneously carrying electrons, as a normal conducting wire, and plasmons [241] enables the realization of complex architectures.

Considering a cylindrical shape of the nanowire, an approximate dispersion relation for a given nanowire can be reconstructed based on the Fabry-Perot resonator model and by comparing with theoretical dispersion relations for infinite cylinders [242, 134, 230].

The surface modes of an infinite metallic cylinder, below the plasmon frequency, are very similar to those of the planar interface [242]. For low ω they asymptotically approach the light line which describes propagation of light in free space. For ω close to the plasmon frequency $\omega_p/\sqrt{2}$, the surface modes become strongly localized at the interface.

Regarding the supported plasmonic modes, in reference 230 Shegai and colleagues observed different outcome for thin and thick nanowires. According to the study, typical diameters for both cases would be 80 and 320 nm. They assumed the nanowires to be situated in homogeneous environments characterized by a refractive index that is the average between the substrate and the actual immersing medium. Their prediction was that the dispersion curves for the thin wire are expected to fall below the light line for the glass substrate, so the plasmons momenta are too large to allow for plasmon decay into far field photons (bound mode). For a thick wire, in contrast, their calculations predicted that the plasmon dispersion should fall well above the light line in glass (leaky mode) [36, 243, 244]. Thus, the thick wire plasmons are lossy and will have a short decay length, thereby enabling unidirectional emission into the substrate which can be visualized by leakage radiation microscopy [35]. For more detailed information on the modes supported by cylindrical and pentagonal nanowires see references [245, 246, 230, 36]. As an example, for rectangular gold nanowires, the size dependence of the supported modes was shown by means of quantum dot photoluminescence imaging in reference 247.

Excitation of propagating SPPs in a Ag nanowire

Figure 4.8 proves the propagation of SPPs in metallic nanowires (NWs) excited by focused laser illumination. The sample used for this section consisted on commercially available silver nanowires of average diameter 100 ± 20 nm wrapped on PVP polymer (PlasmaChem GmbH) and dropcasted onto a glass coverslip.

In general, elastic scattering confocal scans of the sample were recorded, in order to find suitable NWs. For this purpose an avalanche photodiode (APD) was used for signal detection (see setup sketch in figure 2.6), since this allows for scan areas up to $100\,\mu m^2$. A detail of a $\sim 10\,\mu m$ long nanowire is shown in figure 4.8(a). In the next step, the nanowire was imaged onto the CDD camera of the spectrometer using wide-field illumination, so it is possible to allocate the geometry of the nanowire pixel by pixel (see figure 4.8(b)). The wide-field illumination is then switched off and the laser beam is focused at the 'upper' extremity of the nanowire. This is the simplest, most convenient and widespread approach to excite SPPs in a metallic nanowire [248, 249, 22]. Light scattering by the sharp discontinuity provides a broad spectrum of in-plane momenta covering the wavevectors of the plasmon modes sustained by the nanowire [250].

The excitation of SPPs is then verified by the optical image shown in figure 4.8(c) (first panel). Besides light scattering at the focus position, also scattering at point-defects along the nanowire and at the end of it are present, which confirm the propagation of surface plasmons. The intensity is normalize to the maximum intensity (at the laser focus position). The incident linear laser polarization is aligned parallel to the long axis of the nanowire ($\theta = 0°$).

For a detailed analysis of the in-coupling properties, the polarization dependence of the excitation was investigated. Optical images for different incident polarizations are also shown in the next panels of figure 4.8(c) for $\theta = 30°$, $60°$ and $90°$ (second, third and fourth panels, respectively). As the incident polarization goes from 0 to 90, the intensity of the light emission at the remote termination (lower extremity) of the nanowire becomes dimmer. This becomes even more evident when plotting the intensity along the long axis of the nanowire and summed up over all the pixels perpendicular to the propagation direction, as shown in figure 4.8(d). The intensity is normalized to its maximum for every different incident angle, which corresponds to the laser focus position. In these logarithmic scaled intensity cross sections, three features can be identified. Two peaks, one resulting from scattering at the laser focus position, and the other at the remote termination of the nanowire, both diffraction limited and therefore fiteable with a Gaussian peak (see dashed pink line). The third feature is the exponentially decaying intensity of the scattered light along the nanowire, associated with the characteristic exponential attenuation of propagating modes, due to ohmic losses in the metal and leakage radiation [251].

Am about two times stronger light emission can be observed at the remote (lower) termination of the waveguide for a parallel compared to a perpendicular orientation of the excitation polarization, as expected from the transverse magnetic character of the propagating surface plasmon polaritons [5]. A polar plot of the spatially integrated intensity for the laser excitation position (upper termination of the nanowire) (black squares) and remote termination (the lower termination of the nanowire) (red dots) are shown in figure 4.8(e), together with $\sin^2$-fit, as suggested by reference 209. This specific nanowire presents a degree of polarization [247] $DoP = (I_{0°} - I_{90°})/(I_{0°} + I_{90°}) = 0.74$ for the light emitted at the remote termination.

The plasmon generation efficiency, defined as the integrated intensity at the remote position of the nanowire divided by the integrated intensity scattered at the excitation position is shown in figure 4.8(f). The most efficient in-coupling is achieved when the polarization of the excitation is aligned parallel to the nanowire axis, as already demonstrated in previous reports [221, 252, 253, 254, 255]. It should be mentioned here that this is not necessarily always the case, and the optimal polarization condition strongly depends on the precise positioning of the nanowire in the focal spot [250]. It is worth to notice also that the efficiency strongly depends on the nanowire cross-section [256] and the specific shape of its termination [252].

Elastic scattering radiation pattern modification by a Ag NW

Here, the modification of the elastic scattering radiation pattern of laser light at the glass/air interface by a silver nanowire is presented. Figure 4.9(a) displays a wide-field optical transmission image of a $\sim 9.5\,\mu m$ long nanowire. The same nanowire locally excited by the laser beam focused on its left termination is shown in figure 4.9(b). The polarization is oriented parallel to the long axis of the nanowire. Again, light emitted from the other termination, as well as the presence of luminous scattering defects distributed along the nanowire confirm the excitation and the propagation of a surface plasmon in this

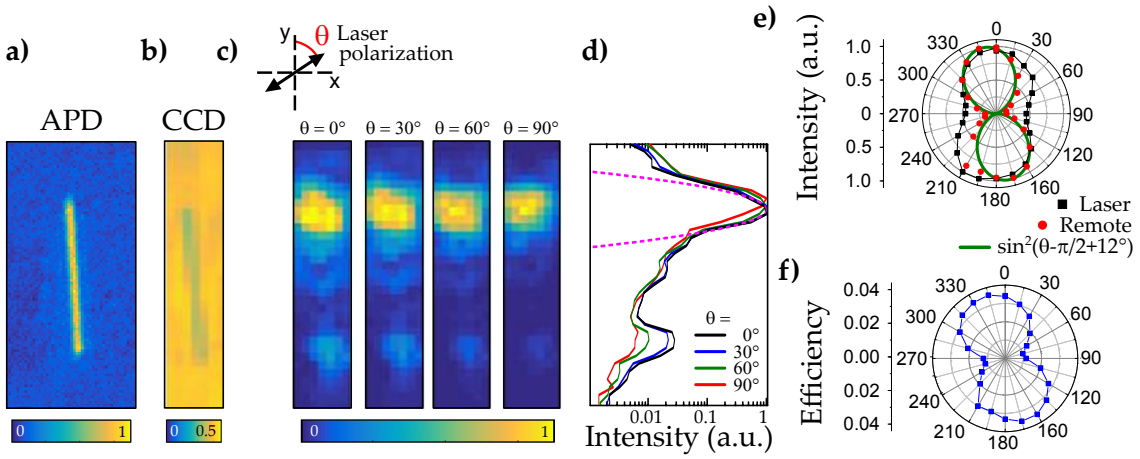

Figure 4.8: (a) Elastic scattering scan of a Ag nanowire on a glass substrate. (b) Wide-field illumination image of the same nanowire. (c) Optical images when the upper termination is illuminated with a linearly polarized strongly focused $\lambda = 633nm$ laser for different polarizations angles θ. (d) Integrated intensity plot along the nanowire showing the coupling efficiency for different polarization angles. The curves are normalized to their maxima. (e) Polarization dependence of the scattered light at the upper (black squares) and lower (red dots) terminations of the nanowire. The latter being fit with a sin^2-function. (f) Polarization dependence of the plasmon generation efficiency.

nanowire.

The corresponding back focal plane image, shown in figure 4.9(c), exhibits the typical signature of a leaky mode: A vertical bright line perpendicular to the propagation direction [250]. The vertical fringe pattern originates from the bound mode sustained by the nanowire, with its maximum intensity line laying outside the detectable wavevector range of the microscope objective [229]. Following the reasoning presented in reference 250, the lack of the signature of a back-reflected mode at negative k_x/k_0 suggests that the reflection coefficient at the extremity is small [257]. According to their work, a standing wave pattern is thus unlikely to explain this Fourier distribution. The oscillations in Fourier space originates from the finite length L_{NW} of the waveguide [258]. The signal recorded in the Fourier plane can be approximated by the truncated Fourier transform of a guided mode propagating along the x-direction [250].

While the BFP pattern of scattered laser light from bare glass appears very symmetric (see figure 4.9(d)), the BFP pattern of scattered laser light by the nanowire is quite asymmetric, revealing a highly unidirectional light emission from supported plasmonic modes. This can be explained by modeling the scattering at the nanowire as the emission from a chain of dipoles with appropriate relative phase retardation, situated above an interface, as describe by Shegai and coworkers [230]. This theoretical description can be achieved by multiplying a single dipole pattern with a structure factor $S(\theta, \psi)$, which contains the phase correlation between the different dipoles [41]:

$$I_{NW} = I_{dipole}|S(\theta,\psi)|, \tag{4.19}$$

with

$$S(\theta,\psi) = \sum_{m=1}^{N} e^{(k_{SPP} - n_2\, k_0\, \sin\theta\, \cos\psi)\, x_m} \tag{4.20}$$

where k_SPP is the plasmon wave-vector, k_0 the vacum wave-vector, n_2 the refractive index of the glass coverslip and objective, N the number of dipoles and x_m is the spatial coordinate of each dipole along the nanowire length L_NW. The origin of directionality here is, following Segai et al.'s publication, similar to that in a phased array or Yagi-Uda antenna, although retardation in the present case is dictated by the dielectric environment and nanowire diameter according to the plasmon dispersion relation [230].

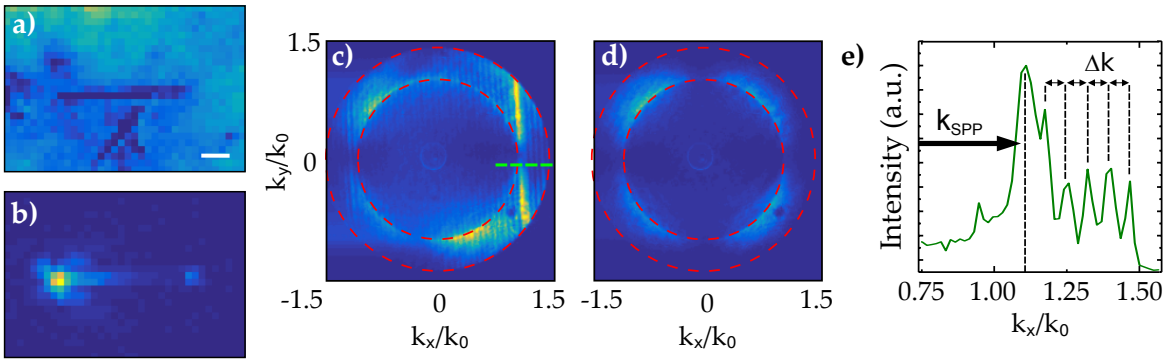

Figure 4.9: (a) Wide-field illumination image of a Ag nanowire on a glass substrate. The white scale bar is 2 μm. (b) Optical image when the left termination is illuminated with a linearly polarized strongly focused $\lambda = 633\ nm$ laser. The incident polarization is parallel to the nanowire. (c) Back focal plane images showing the wavevector distributions for scattered light when the laser is focused on the left termination of the nanowire (c) and bare glass (d). The vertical brightest line is recognized as the signature of the leaky SSP mode. (e) Cross section following the green dashed line in figure (c). The brightest line indicates the plasmon momentum $\vec{k}_{SPP}$ and the fringes separation the length of the nanowire $L_{nw} = 2\pi/\Delta k$.

Useful quantitative information can be extracted from such BFP patterns. The position of the maximum line in the Fourier space determines $k_{SPP} = 1.1\, k_0$, as sketched in the cross section taken from the green dashed line in figure 4.9(c) and plotted in 4.9(e). The fringe pattern observed are also known as Gibbs oscillations, and occur when the nanowire length L_{NW} is smaller or close to the mode propagation length L_{SPP} [258]. The oscillation period is therefore $\Delta k = 2\pi/L_{NW}$ or $\Delta n = \lambda/L_{NW}$ [241]. In the case of the nanowire studied in figure 4.9, Δn is evaluated at 0.059 corresponding to a nanowire length $L_{NW} = 10.6\ \mu m$. Considering the experimental errors and the limited resolution of the optical microscope

this value coincides with the length $L_{NW} = 9.8\ \mu m$ measured from the optical image in figure 4.9(a).

Interestingly, similar to what happens with photoluminescence [33, 44] and Raman scattering (see chapter 6 and reference 259) emission, radiation pattern from this system appear to be described by two contributions: elastic scattered light at the glass/air interface (see figure 4.9(d)) and laser light re-radiated through the NW after being carried by propagating SPPs.

4.3.2 Redirecting quantum dot emission with dimer antennas

A recent and successful approach to create advanced plasmonic architectures relies in employing self-assembled DNA nanostructures as scaffolds [260]. Fabrication of DNA-assembled plasmonic nano-structures can be achieved, for example, by functionalization of gold nanoparticles (AuNPs) with thiol-modified single-stranded DNA (ssDNA) as programmable linkers [261, 262]. AuNPs dimers can then form through Watson-Crick base pairing of complementary ssDNA-modified AuNPs.

In this subsection, the antenna function of Au dimers when a quantum dot is placed in between the Au particles is demonstrated by Fourier space imaging. The QD-dimer particles were provided by F. Nicoli and M. Pilo-Pias, from the group of Prof. Tim Liedl (LMU Munich) and consist of Au particles of 30 nm in diameter and core shell QDs with photoluminescence emission centered at 630 nm. Figure 4.10(a,b) show the emission spectra from QD-dimer antennas in comparison to emission spectrum of a QD ensemble. The emitted radiation from this QD-dimer system is nominally composed not only by quantum dot photoluminescence (PL), but also possibly by gold PL from the dimer, and, as an important contribution, DNA surface-enhanced Raman scattering.

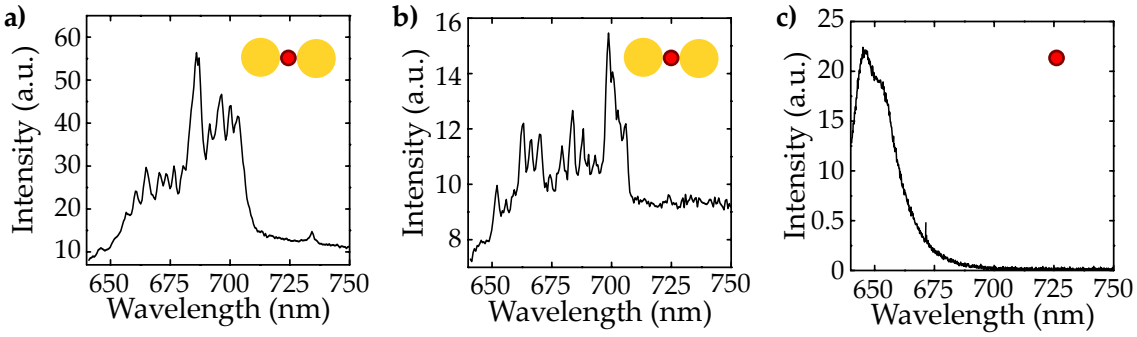

Figure 4.10: Spectral characteristics from two QD-dimer particles (a,b) and a QD ensemble (c). The emitted radiation from this QD-dimer particles is nominally composed by quantum dot photoluminescence, by gold photoluminescence from the dimer, and DNA surface-enhanced Raman scattering.

Figure 4.11 presents the radiation patterns observed for two different QD-Dimer particles (a,b, second column), along with the calculated radiation patterns (third column) for

point-dipolar emitters in the x-y plane oriented at $\Phi = 50°$, and $-15°$ with respect to the x axis, respectively. The fourth column shows the emission intensity profile through the experimental (red line) and calculated (blue line) patterns for a radius corresponding to a numerical aperture of 1.05. The comparison between the experimental radiation patterns with the calculated pattern of a point-dipole in figure 4.11(a,b, second column) indicates that the emission from the QD-Dimer system can be modeled by an in-plane point dipole. This is confirmed by the corresponding series of parameter-free calculated patterns for the respective particles, presented in the second column of figure 4.11. The quantitative agreement between experimental and theoretical emission distribution can also be seen from the comparison of the corresponding cross sections in the third column of figure 4.11. For comparison, figure 4.11(c) presents the unpolarized radiation emission pattern observed for a QD cluster. In this case, the radiation pattern of QD can be modeled as the incoherent sum of three orthogonal point-dipole emitters (one along the x axis, one along the y axis and one along the z axis). The cross section of the experimental pattern shows that there is no privileged emission direction and its cross section agrees with the calculated one.

In principle, radiation patterns from this system are expected to be described by two contributions: direct unpolarized emission from the QD and emission radiated through the antenna (dipolar emission). However, it can be observed that the radiation patterns from QD-dimers coincide with the calculated radiation patterns from single point-dipole emitters. First, this demonstrates the antenna function of the dimer structure, and second, suggests that the emission enhancement is strong enough so the direct unpolarized emission from the QD can be neglected.

4.4 Conclusions

Optical antennas, as introduced in section 4.1, are a powerful tool for manipulating light at the nanometer scale, while also providing optimal control of transduction in the far-field. While some concepts, like antenna gain and antenna directivity, derive from classical antenna theory, the direct downscaling of antenna designs into the optical regime is not possible because radiation penetrates into metals and gives rise to plasma oscillations. Furthermore, the quantum and atomistic effects become relevant for specific configurations. In general, an optical antenna is designed to increase the interaction area of a local absorber or emitter with freely propagating radiation, thereby making the light-matter interaction more efficient. This applies to distinct photo-physical sample responses, including photo-induced light emission, photovoltaic responses and electrically driven light emission.

Based on the optical antenna concept, Tip-enhanced near-field optical microscopy (TENOM) is a highly versatile tool for the spectroscopic investigation of nanoscale materials on surfaces. Besides a broad range of purely optical information, TENOM can also provide spatially correlated optoelectronic information, as will be shown in chapter 5. With this tool details of the optical-to-electrical and electrical-to-optical transduction in nanoscale devices can be investigated on relevant nanometer length scales.

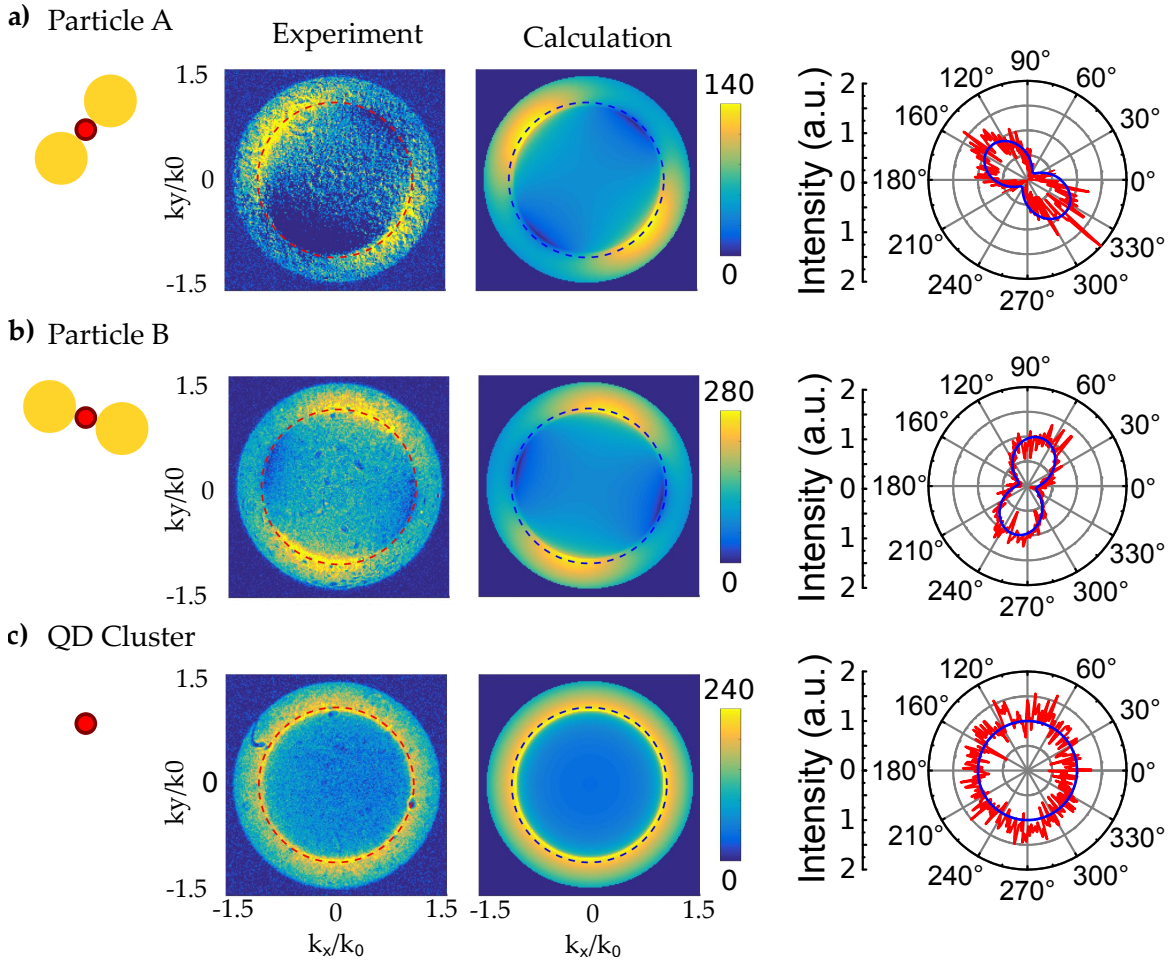

Figure 4.11: Antenna function of QD-dimer particles: Radiation characteristics from two QD-dimer particles (a,b) and a QD ensemble (c). First column: Sketch of the particle under study. Second column: Experimental radiation patterns. Third column: calculated radiation patterns for point-dipolar emitters in the x-y plane oriented at $\Phi = 50°$, and $-15°$ with respect to the x axis, in the case of (a), and the incoherent sum of three orthogonal point-dipole emitters (parallel to the x, y and z axis). Fourth column: Cross section through the experimental (red line) and calculated (blue line) patterns for a radius corresponding to a numerical aperture of 1.05.

As these nanoantennas aim to control the optical fields at the nanoscale, they can highly benefit from the plasmonic properties of metallic structures. After discussing the basic properties of propagating and localized surface plasmon polaritons in section 4.2, examples of their ability to redirect the radiation emission are provided in section 4.3. While emission from a quantum dot - gold dimer antenna can be modeled by point-dipole radiation, in the case of a silver nanowire a chain of correlated point-dipoles is required. This results in a very distinctive pattern from which several characteristics can be inferred, as for example the momentum of the SPP and length of the nanowire supporting it. This sets the basics of back focal plane images analysis employed in chapter 6 in order to show remote surface-enhanced Raman scattering.

Chapter 5

Observations of tip-enhanced photocurrent in graphene

Photodetectors based on graphene are being developed at a remarkable pace, with great promise for a wide variety of applications in many different fields [263]. Photodetection, as well as other optoelectronic applications, rely on the conversion of absorbed photons into an electrical signal. The simplest class of graphene-based photodetectors, and the first one being investigated, are metal-graphene-metal photodetectors [264, 265, 266].

In a metal-graphene-metal device at zero bias, the photocurrent signal is known to be generated by at least two different mechanisms: the photovoltaic effect and the photothermoelectric effect. Photocurrent generation by means of the photovoltaic effect is based on the separation of photogenerated electron-hole (e-h) pairs caused by built-in electric fields. These fields exist at the contact regions due to the formation of energy barriers, introduced by the work function difference between graphene and the contacting metal [267, 268, 269, 270]. Built-in electric fields could also occur along the nanostructure caused by sample heterogeneities, as local chemical doping [271],or external perturbations, as the external electric field generated by the use of split gates [267, 272]. Due to the photothermoelectric (or Seebeck) effect, a photovoltage can be produced by the photogenerated hot electrons at the intersection between two regions with different doping. This effect can dominate in graphene p-n junctions [272, 273] or in suspended graphene [270]. A substantial contribution can also stem from the illumination of the electrodes near the contact region [274, 275, 270]. This contribution is due to laser heating of one of the electrodes and can be thermoelectric in origin or caused by thermo-assisted tunneling of charge carriers through the energy barrier [205]. Other mechanisms resulting in the generation of photocurrent are triggered by external perturbations, as is the case of the bolometric effect [276], the photogating effect and the plasma-wave-assisted mechanism [277, 278, 279]. For more details see reference 263.

A popular tool used for the investigation of graphene devices as light detectors is scanning photocurrent microscopy (SPCM). SPCM has been applied to study the properties of nanoelectronic devices such as carbon nanotube- [280, 281, 282], graphene- [266, 269] or inorganic nanowire- [283] based field-effect transistors. This technique consists of raster

scanning a focused laser beam across a device, simultaneously recording the photocurrent generated after laser light absorption by the sample, resulting in a photocurrent map. It provides valuable information on any source of built-in electric fields including internal pn-junctions [284], local defects [280] and nanostructure-metal interfaces [266, 269, 285]. Metal interfaces are part of virtually all nanoscale devices and govern their overall performance [286, 287, 288].

There have been some fruitful efforts using infrared excitation [289] and visible light [269] with a resolution of around 100 nm. However, nearly all SPCM measurements on graphene using visible light reported so far have been restricted to a spatial resolution of few hundred nanometers due to the diffraction limited size of the laser focus, making it impossible to optically characterize a device on the nanoscale.

As introduced in chapter 4, tip-enhanced near-field optical microscopy (TENOM) overcomes this limit [9]. It has already proven successful in characterizing carbon nanotube-based devices at sub 30 nm spatial resolution [205]. This allowed for imaging of the zero-bias photocurrent caused by charge separation in local built-in electric fields at the contacts and close to charged particles that cannot be resolved using confocal microscopy.

First, the working principle and the description of the SPCM setup are presented, followed by the implementation of TENOM measurements in such setup. Then, two examples of confocal zero-bias photocurrent imaging of graphene devices are presented. The simultaneous acquisition of Raman signals allows to correlate optical and optoelectronic information. Antenna-enhancement results in $\sim$ 25 nm spatial resolution. In the case of the photocurrent signal, the near-field contribution allows to observe a steeper slope at the electrodes edges, as well as several subdiffraction modulations in both photocurrent and Raman signals. As an outlook, a technique enabling the separation of the near-field and far-field contributions via tip-sample distance modulation, and therefore promising higher contrast, is introduced.

5.1 Experimental implementation

5.1.1 Scanning photocurrent microscopy

In scanning photocurrent microscopy (SPCM) a focused laser beam is raster scanned across a contacted sample (device). The sample absorbs light resulting in electrical current (photocurrent), which is recorded for every position, resulting in a photocurrent map. SPCM is a powerful tool to investigate the electronic properties of devices such as carbon nanotube- or graphene-based field-effect transistors at the nanoscale [266, 283]. However, the photocurrent signal is typically weak when compared to the noise level, so preamplification is required. This was done with a current-to-voltage amplifier (Femto, DLPCA-200) combined with a lock-in detector (Stanford Research Systems, SR 830). A schematic is shown in figure 5.1.

Typical amplification factors of the current-to-voltage amplifier were 10^6 or 10^7 V/A [194]. The output voltage was delivered to the lock-in amplifier. The laser intensity was

modulated with a chopper (Thorlabs, MC2000, Blade MC1F10) in the excitation beam path at the focus position of the first lens pair used for beam expansion (see section 2.5). A modulation frequency of $\sim$ 900 Hz was typically used. A reference signal with the same frequency was connected to the lock-in detector acting as a very narrow band pass filter centered at the modulation frequency. The filtering consists of multiplying the reference signal with the amplified photocurrent signal (in V) resulting in a DC component for equal reference and signal frequency and in AC components for other frequencies. The DC component was filtered out by using a low pass filter (resistor-capacitor (RC) type). By adjusting the time constant, the bandwidth of this filter was set. The scan parameters of the image acquisition (scan speed, pixel size) were chosen such that the pixel dwell time is long enough [194]. A typical value of 10 ms was used for the time constant. The lock-in detector was connected to the SPM 1000 and the photocurrent signal was recorded simultaneously with the optical (Raman/elastic scattering) signal. A detailed explanation of this setup can be found in reference 194.

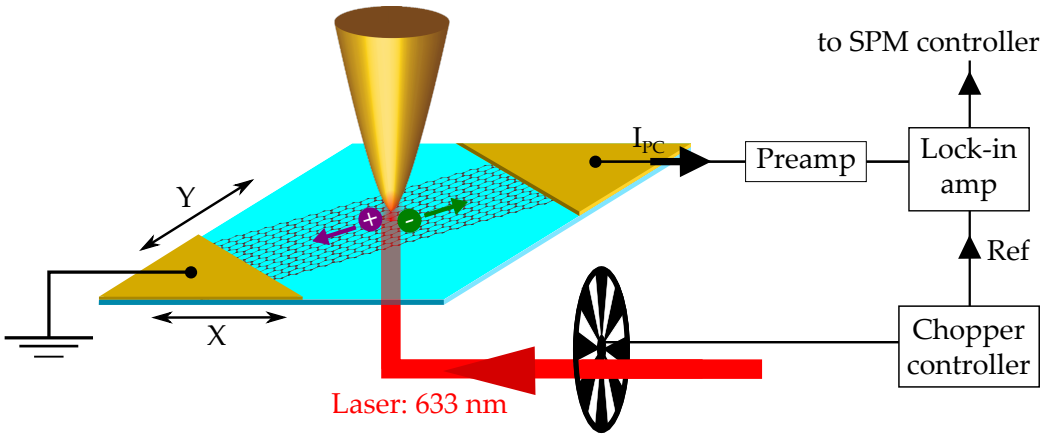

Figure 5.1: Schematic of the setup used for tip-enhanced photocurrent and Raman scattering measurements. A laser beam was focused onto the scanning sample, were antenna-enhanced (if the tip is present) or confocal (if it is not) photocurrent was generated. The photocurrent was then preamplified by a current-to-voltage amplifier and detected by a lock-in detector. A chopper in the excitation beam path modulated the laser intensity. The photocurrent was then recorded simultaneously with the the optical signal by the SPM controller.

5.1.2 Tip-enhanced near-field optical microscopy (TENOM)

The TENOM setup used during this thesis is based on a confocal microscopy setup similar to the one described in section 2.5. With the purpose of enabling TENOM with a scanning tip, several additional features, described in the following, needed to been added.

The optical antennas were fabricated by electrochemical etching of a solid gold wire resulting in sharp gold tips of down to 20 nanometers of diameter [290, 291].

In order to optimize the tip-enhanced near-fields due to the lightning-rod effect, the electric field of the incident laser should be polarized along the tip axis (z axis) [292]. Since a linearly polarized beam only provides very weak z components after being focused, a radially polarized mode is needed. A beam of light has radial polarization if at every position in the beam profile the polarization (electric field) vector points towards the center of the beam. After being focused by a high NA objective lens, the components in the x-yy plane interfere destructively, and the components of the z plane interfere constructively, resulting in a strong z component in the center of the focus. The mode conversion between a linearly polarized and a radially polarized mode is achieved by a mode convertor, consisting of 4 quadrants of $\lambda/2$ waveplates. More details about can be found in reference [293, 294].

An integral part in TENOM measurements, as well as SNOM in general, is the optical antenna-sample distance control mechanism, enabling the scanning of a tip in close proximity to the sample surface. In order to benefit from the near-field of the antenna, the distance should be only a few nm, meaning that the feedback system must be highly sensitive relying on short-ranged interactions between tip and sample surface. In scanning tunneling microscopy (STM) [295] and atomic force microscopy (AFM) [296] the interaction used for the feedback (tunneling current and force, respectively) is already the physical quantity of interest. However, using the optical near-field signal as feedback to control the tip-sample distance in near-field optical microscopy is not practicable. Using a tunneling current, as in STM, requires conductive samples, which makes the technique too restrictive, and the forces involved in contact or tapping mode AFM are too large for a ductile gold tip and result in tip damage. The distance-control mechanism employed during this work is the so-called shear-force detection. It can be realized by attaching a gold tip to a quartz tuning fork vibrating parallel to the sample surface within a distance of a few nm, therefore resulting in small interaction forces of piconewtons [293]. Upon approaching the sample, the oscillation amplitude (usually few nanometers) decreases. Simultaneously, this decrease in oscillation amplitude is connected to an increase of the resonance frequency. Since using the amplitude as feedback signal has the drawback of a large response time to perturbations of the system and therefore slow scan speeds, usually the frequency shift is used as feedback signal [4].

A homemade AFM head is used to support this approach. The piezo electric material on this head gives the possibility to move the tip in the x and y directions, enabling the alignment of the tip in the x-y plane. The AFM is standing on top of the microscope, so while the tip, and the laser focus sit at a fixed position, it is the sample, standing on a piezo stage, the element which is scanned in order to obtain the images (as described in section 2.5).

More detailed information about tip etching, laser mode conversion, and tip-sample distance control by shear-force feedback can be found in the Ph.D. theses of X. Shi [293], J. Janik [297], T. Mancabelli [298], N. Mauser [194], M. Bömler [50], C. Georgi [290], and H. Qian [291].

5.1.3 Device fabrication

Two different graphene samples were used during this work: Sample A and sample B. For sample A, graphene was fabricated using the chemical vapor deposition (CVD) method and transfered to a glass coverslip by Jürgen Kraus and Prof. Sebastian Günther at the TUM / LMU Munich. Consequently, the devices were fabricated by optical lithography, as explained in this subsection. Details on graphene fabrication and transfer can be found in the appendix A. For sample B, the devices were fully fabricated by Ugo Sassi from Prof. Andrea C. Ferrari's group at the graphene center in Cambridge, following a similar approach.

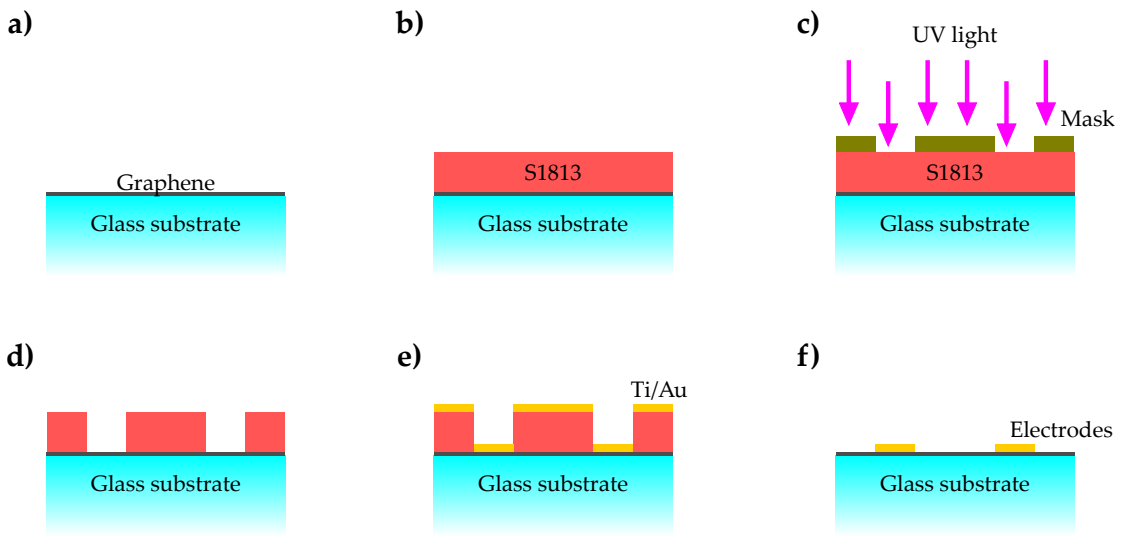

Figure 5.2: Schematic of the optical lithography recipe. (a) The starting point is graphene on top of a glass coverslip. (b) The coverslip is spincoated with a photoresist. (c) The sample is illuminated with UV light through a copper mask. (d) The illuminated areas of the photoresist are easily disolved and cleaned away. (e) Evaporation of a thin film of titanium and gold. (f) The photoresist and the metal covering it are lifted-off.

Optical lithography

For the contacting of the CVD-grown graphene on a glass coverslip, a typical optical lithography procedure was followed. The starting point was CVD-grown graphene fabricated and already transfered to a glass coverslip (see figure 5.2(a)). This sample was spin coated with a positive photoresist Microposit S1813 (figure 5.2(b)). The covered sample was soft-backed on a hot plate to dry the photoresist. The sample was then illuminated with UV light through the transparent regions of a photomask (figure 5.2(c)) using a mask aligner with a mercury lamp. The photomask was fabricated by Claudia Paulus at the Walter Schottky Institute (Garching). It typically consists of a chrome covered plate showing a transparent pattern. In this case the pattern consisted in the shape of the electrodes

designed for contacting graphene with a separation of $5\mu m$ between electrodes. After the exposure of the photoresist to UV light, it becames soluble in the developer solution (Microposit), so it can be easily removed (figure 5.2(d)). A thin film of $\sim$ 3 nm of titanium, used as adhesion layer, was evaporated on the substrate, followed by $\sim$ 25 nm of gold (figure 5.2(e)). Afterwards, the left overs of the photoresist, together with the metal on its top were lifted-off using warm acetone and a ultrasonicator, resulting in the desired metal electrodes (figure 5.2(f)).

5.2 Confocal zero-bias photocurrent imaging

Two different samples, as described in the fabrication appendix A, were investigated. The discussion of results starts with the first one. Figure 5.3 displays confocal optical and photocurrent images of two different graphene devices fabricated according to the procedure described in section A.1.

The first panel in figure 5.3(a) shows a $18\mu m^2$ confocal Raman scattering image of a contacted graphene device with a nominal electrode separation of $5\mu m$. For this, a 700 nm band pass filter with a window of 10 nm was used, since the wavelength of the G Raman band for a 632.8 nm laser excitation lies at 702 nm. Even though, as explained in the fabrication subsection 5.1.3, there should be graphene everywhere, the most intense signal is observed to be coincident with the edge of the metallic electrodes. One possible explanation is that surface plasmon polaritons (SPPs) enhanced the Raman signal at the sharp edges of the metal, given that the plasma frequency of gold lies in the visible (see chapter 4). A second possibility is that some polymer residues mixed with gold accumulated at the edges during the optical lithography process, rendering a higher Raman signal. This possibility would also explain the bright signal spots shown in the inner region of the electrode. In any case, this fact helps in the delimitation of the electrodes, which benefits the analysis of the photocurrent signal shown in the next panel (second column), where the dashed line corresponds to the edges as seem in the first panel.

Photocurrent signals of opposite sign appear at the graphene-metal contacts. It can be observed that while for the left electrode region the photocurrent signal is slightly above zero and for bare graphene is approximately zero, the most intense (negative) signal comes from the right electrode. A possible explanation is that while one of the electrodes is grounded, the other is closer to the lock-in amplifier. Even though the signal is dominated by the electrode in general, some strong modulations of the photocurrent signal can be observed in its inner region, and some minor ones surrounding it. The cross section of both Raman and photocurrent signals taken at the center of the images is shown in the third column in order to give an idea of the scale used.

A $6\mu m^2$ confocal Raman scattering and photocurrent images of a different device are shown in figure 5.3(b), together with the corresponding cross sections. While the photocurrent signal is again dominated by the electrodes some weak features can be observed that are accompanied with stronger signals in the Raman scattering image. These features can result from foldings occurred during the graphene transfer, accumulation of amorphous

carbon, or most likely, polymer residues from the optical lithography process.

In conclusion, there are different contributions to the zero-bias photocurrent signal in such graphene devices, depending on the sample region. The strongest signal is observed at the interface between graphene and the metal electrodes. On one hand, a thermoelectric contribution due to laser illumination, and therefore heating, of the electrodes is expected. On the other hand, also a photovoltaic contribution is expected which would stem from the energy barrier introduced by the work-function difference between graphene and the contacting metal, resulting in built-in electric field which causes the separation of e-h pairs. In addition to the metal contacts, zero-bias photocurrent signals are also observed along the graphene channel between the electrodes. In this case, built-in electric fields might be caused by sample heterogeneities, as local chemical doping, but also a photothermoelectric contribution steaming from the photogenerated hot electrons at the intersection between two regions with different doping.

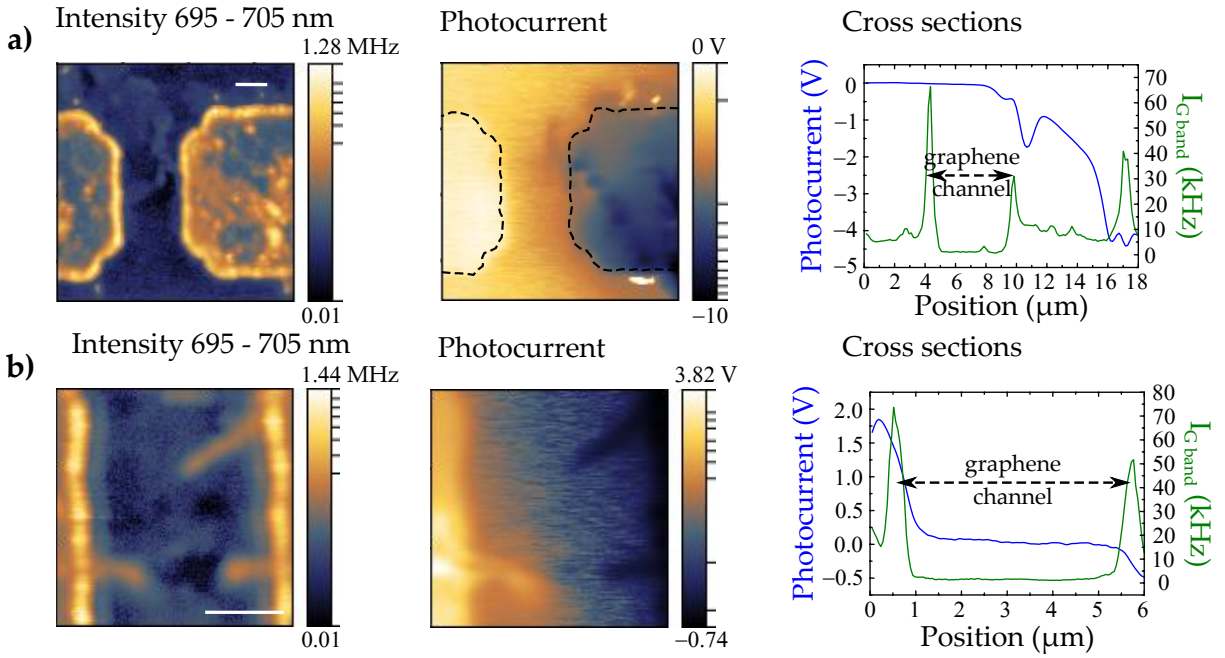

Figure 5.3: Confocal zero bias photocurrent and optical images of two devices (a) and (b). The distance between electrodes is 5 μm in both cases. Intensity collected with a 700 ± 5 band pass filter is shown in the first column, collecting emission from the G band, but also scattered light from the gold. The images reveal an inhomogeneus graphene sample and helps locating the position of the gold electrodes. The second column shows simultaneously taken zero-bias photocurrent images. Two photocurrent signals of opposite sign appear at the contacts. In addition to the signals at the contacts photocurrent fluctuations along the graphene channel exist. The intensity color scale was chosen by the program Gwydeon, in order to make visible every feature in the images. The third column show a cross section of the Raman and zero bias photocurrent images. The 5 μm graphene channel is indicated by the balck dashed line.

In short, both thermoelectric and photovoltaic effect contribute to a varying degree to the photocurrent at the metal contacts and along the channel of the studied graphene-based devices. Motivated by previous studies in which tip-enhanced near-field microscopy was able to image both contributions separately [205], tip-enhanced photocurrent microscopy experiments were performed.

5.3 Tip-enhanced zero-bias photocurrent imaging

As described in the previous section, confocal scanning photocurrent microscopy is a versatile technique to characterize carbon based optoelectronic devices. However, it reaches its limits at the nanoscale due to the diffraction limit of light, hindering a characterization of devices on nanoscale length dimensions. Tip-enhanced near-field optical microscopy (TENOM) helps overcoming this limit, by exploiting the strong electromagnetic field enhancement in the vicinity of an illuminated metallic nanoparticle to locally increase the absorption and hence charge carrier generation in nearby graphene.

This section reports on the first photocurrent measurements in the visible range along single layer graphene devices yielding a spatial resolution of about 25 nm. In the following, two different samples are investigated, in which photocurrent, topography and scattering signals taken simultaneously are compared.

Figure 5.4 presents simultaneous tip-enhanced photocurrent, optical and topography images of the (a) electrode-graphene and (b) graphene channel regions. Subdifraction modulations appear both in the the photocurrent and G Raman band images of figure 5.4(a). The cross sections show the resolution of this modulations to be below 50 nm, showing a near-field contribution. The edge of the electrode should lie along the line indicated by the highest Raman intensity, and it is also delimited by the strongest (negative) photocurrent signal (from position 0 to 0.7 μm in the horizontal axis). Despite the near-field presence, the topography image does not correspond to the expectations (clear topography showing flat graphene and the edge of the electrode) after the photocurrent and Raman images, possibly because of not proper centering the tip with the laser excitation spot or photoresist remaining after the fabrication procedure.

While it is necessary to look at the cross sections to observe subdiffraction modulation in the photocurrent image of figure 5.4(b), several subdiffraction spots can be observed in the Raman image. While some of these spots correlate with lower topography, which might indicate a shadowing effect of the tip, other spots, as the one indicated by the cross section, correlate with a protrusion in topography. Both Raman and photocurrent images present features with peak widths of about 25 nm, substantially below the diffraction limit for a laser wavelength of 632.8 nm. In case of negligible feature size, this number would correspond to the spatial resolution in the experiment.

It should be noted here that, whereas the photocurrent and Raman images resulted satisfactory in the sense of showing a clear near-field contribution resulting in subdiffraction resolution, the associated topography is not the expected, since the edge of the electrode seems to be too high, and the bare graphene region should be flatter than 1 nm. In

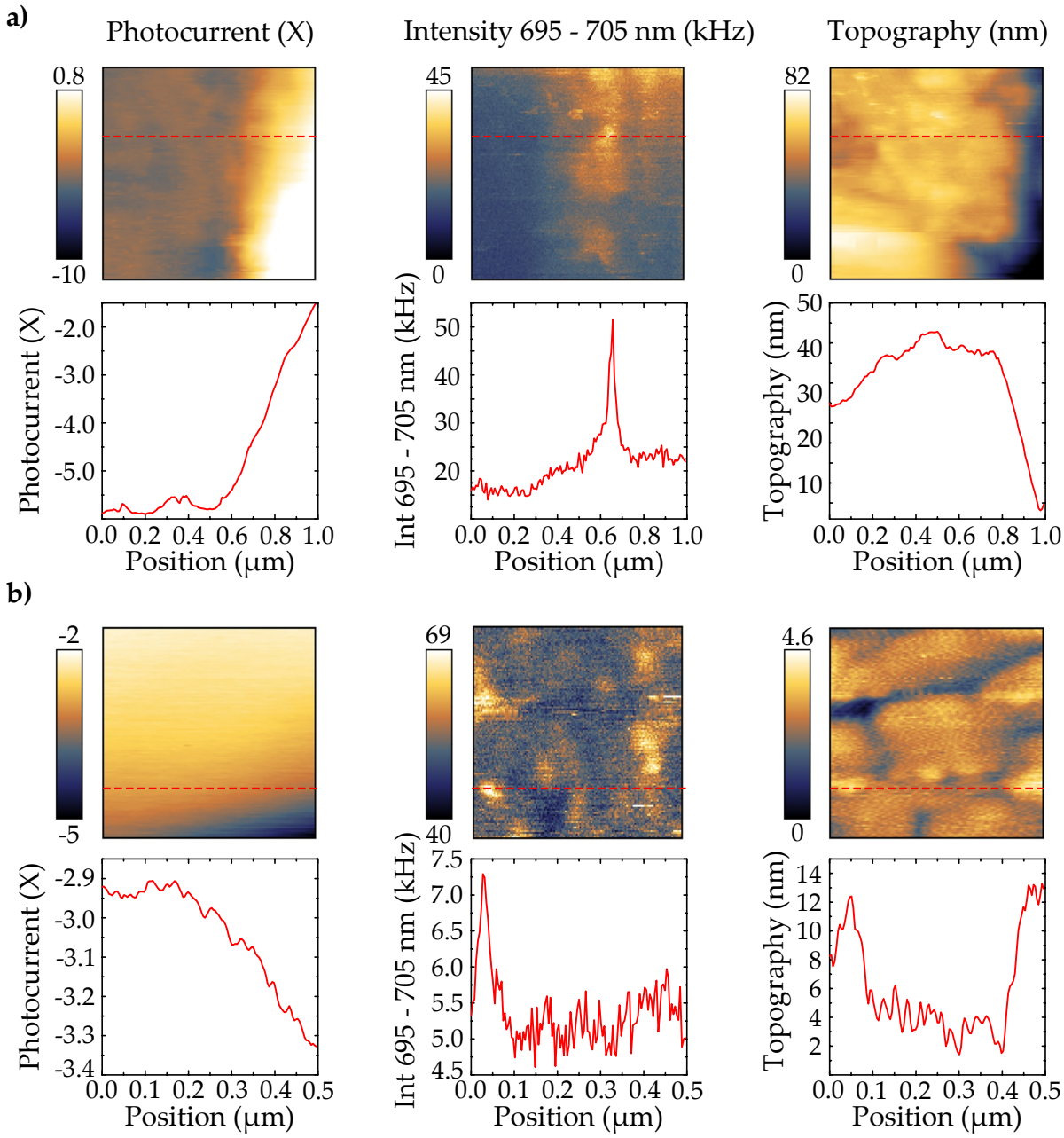

Figure 5.4: Tip-enhanced zero bias photocurrent and optical images of the electrode-graphene (a) and graphene channel (b) regions of a device, together with the cross sections marked by the red dashed lines. Subdifraction modulations in photocurrent and Raman signals can be observed in both the electrode and the channel regions. While the topography of the electrode is not clear, correlations between topography and Raman signal can be seem in the graphene channel region with a width of ~ 25 nm.

summary, the amount of residual photoresist is too large in order to obtain well-defined topography information, allowing for the correlation with the optical and photocurrent signals. Therefore a second sample, fabricated by Ugo Sassi at the graphene center (Cambridge) was investigated. Three different sets of scans over this sample are shown in figure 5.5.

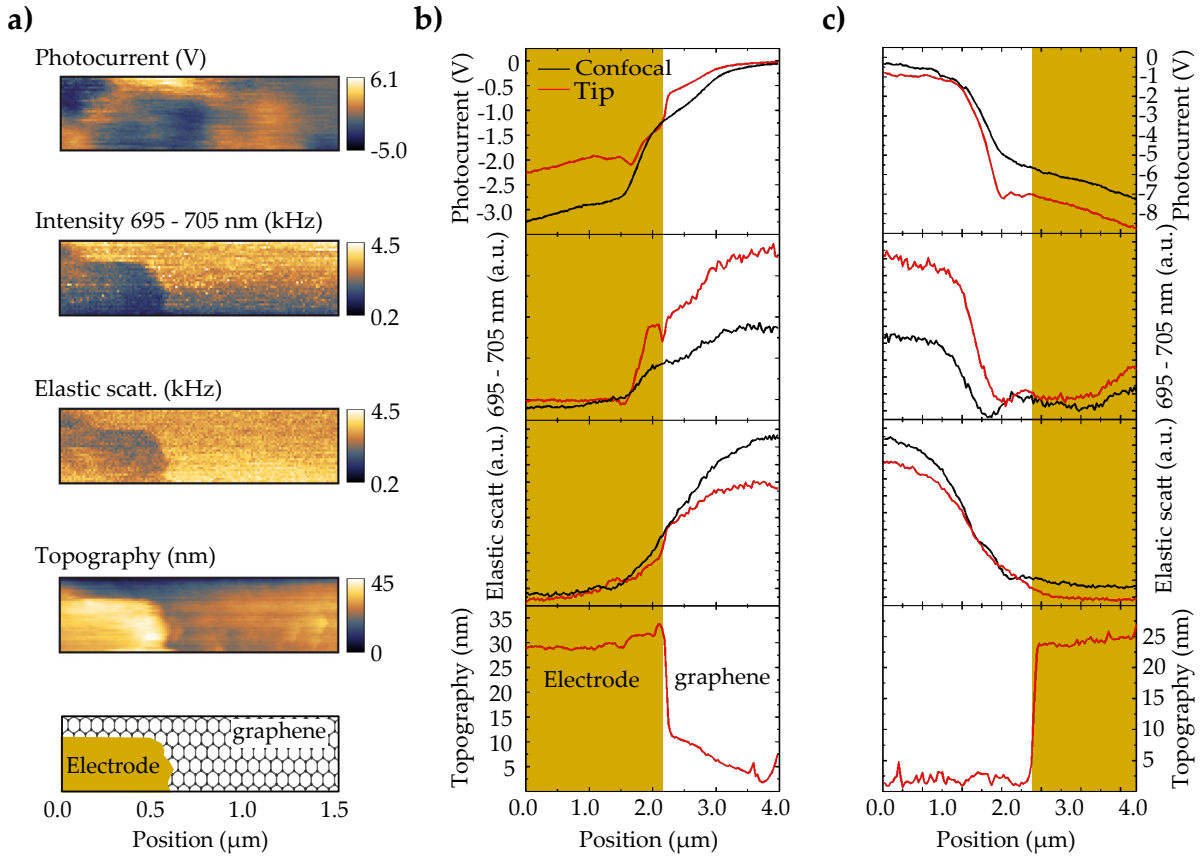

Figure 5.5: (a) Tip-enhanced zero-bias photocurrent, optical images and its simultaneously taken topography of the electrode-graphene region of a device. The scheme shows the configuration of the maps, with an electrode (yellow) on top of graphene. Subdiffraction modulations can be seem in the photocurrent signal. (b,c) Confocal (black line) and tip-enhanced (red line) photocurrent, optical and topographical signal line scans over the graphene-electrode edge region. The yellow area represents the electrode position. Subdifraction modulations and steeper slopes can be observed for photocurrent signal.

Figure 5.5(a) shows a tip-enhanced photocurrent, G band, elastic scattering and topography images of the electrode region of a graphene device. Again, the photocurrent image show signal intensity modulations with a size down to 35 nm. In this case, the sample presents a much clear topography in which the electrode position can be easily identified. Even though the G band and the elastic scattering signals do not show any clear subdiffraction modulation, the images still show a clear contrast at the electrode.

Figures 5.5(b) and (c)show two confocal (black line) and tip-enhanced (red line) line scans over two different electrodes. The same line scan was performed several times and the result was averaged. The position of the electrodes, clearly delimited by the topography line scan, is indicated by the yellow rectangles. Besides subdiffraction modulations, as previously observed, there are steeper signal variations visible at the edges of the electrodes when comparing the tip-enhanced photocurrent signal with the confocal one. Somme modulations are also observed for the G band line scan, which clearly shows some $\sim 2\times$ enhancement at the bare graphene regions. A lower background signal is observed for tip-enhanced elastic scattering at the graphene channel.

5.4 Conclusions and Outlook

In this chapter simultaneous near-field Raman, photocurrent and topography images were recorded on metal-graphene-metal devices. A clear photocurrent near-field contribution was observed from the steeper slope of the signal at the electrodes edges as well as several subdiffraction modulations in both photocurrent and Raman signals. However, no clear indication of correlation between this two signals was found so far. A possible reason for this is that the near-field contribution is too weak when compared to the far-field contribution. While the far field background is widely spread all over the laser spot area coinciding with the sample, the near field contribution is spatially confined the sample area under the antenna's influence. This makes the TENOM study of two-dimensional materials very challenging in comparison with lower-dimensional systems. Furthermore, in the case of two dimensional systems, a vertical antenna, perpendicular to the sample, is not the most appropriate configuration, since the coupling between antenna and emitter/receptor is not so strong as in an horizontal case [133]. Therefore, further investigations are needed to clarify the near-field contribution. More specifically, a new approach based on near-field / far-field separation via tip-sample distance modulation could be employed in order to improve TENOM measurements in two-dimensional systems. This approach, already developed by X. Shi [293], is described in the next subsection.

5.4.1 Near-field to far-field separation via tip-sample distance modulation

One of the biggest challenges confronting TENOM, and SNOM in general, is that even though the optical antenna provides an enhanced signal with a high spatial resolution, the far-field background from direct laser illumination on the sample is still present. This far-field (or confocal) contribution lowers the signal to background ratio and decreases detection sensitivity. Furthermore, the near-field contribution is not specially strong in some cases, as for example in two-dimensional system which required an in-plane polarization of excitation field, and emit light also with an in-plane polarization. In such cases, the near-field contribution could be covered by the far-field background, so it would not be observable at all. Several methods have been developed for increasing the near-field/far-field

signal ratio and can be found in literature [299, 300, 301, 302, 303, 304], (also including an approach using a tuning-fork based systems tip-sample distance modulation [305]).

However, all these different approaches present different disadvantages [293], so a new scheme with simple configuration, little tip perturbation and suitability to tuning fork-based systems is still on demand. A very convenient approach, compatible with the setup used during the scope of this thesis was developed by X. Shi [293]. Based on the idea that the enhanced near-field is very much confined to the tip apex within less than 10 nm range, and the field intensity decays approximately exponentially with tip-sample distance [153, 155, 306], his approach consists on orienting the tuning fork vibration perpendicular to the sample surface and drive an oscillation amplitude larger than the near-field decay length. When the tip gets closest to the sample, the near-field signal is 'on'; when the tip moves to the farthest point, the sample is out of the near-field interaction range and the near-field signal is 'off'. In the conventional configuration, as used during this thesis, the tuning fork vibrates parallel to sample surface together with the tip, so the shear-force is used to control tip-sample distance. In this new configuration, the tuning fork legs were bend by 90° and oriented parallel to the sample surface, so that the tip vibrates in z direction.

This configuration works similar to a tapping mode AFM and the normal force between tip and sample is used to determine the tip-sample distance. However, this is a very challenging experimental condition and the feedback needs to be more carefully controlled, since gold tips are very fragile and the normal force applied to the tip is magnitudes larger than in shear force configurations. This approach was succesfully employed by X. Shi in order to separate the near-field and far-field contributions on tip-enhanced photoluminescence of single-walled carbon nanotubes [293].

Chapter 6

Remote excitation and detection of SERS from graphene

This chapter is based on the publication "*Remote excitation and detection of surface-enhanced Raman scattering from graphene*" by Nicolás Coca-López, Nicolai F. Hartmann, Tobia Mancabelli, Jürgen Kraus, Sebastian Günther, Alberto Comin, and Achim Hartschuh, Nanoscale, doi:10.1039/C8NR02174K, 2018.

Surface plasmons are the coupled mode of an electromagnetic (EM) field with the charge density oscillations at a metal-dielectric interface [5, 307] (see section 4.2). Some of the most promising applications of surface plasmons are in surface-enhanced Raman scattering (SERS) [8] and near-field optical microscopy [129], for which the electromagnetic field enhancement by localized surface plasmons (LSPs) is the dominating contribution to the signal enhancement [10] (see section 4.1). Performed at noble metal surfaces or metallic nanoparticle aggregates, signal enhancements of up to 10^{11} enable the detection of Raman spectra at the single molecule level [11, 12, 13]. Particularly strong EM field enhancement is generated in a highly localized area, for instance at the interstitial sites in a nanoparticle dimer [177] or between a nanoparticle and a planar metal surface [193]. The Raman signals in most SERS experiments are obtained from these hot spots [308, 309]. In contrast to localized SPs, propagating surface plasmon polariatons (SPPs) occur at extended planar metal-dielectric interfaces [207] with propagation lengths of up to several tens of micrometers [5]. Importantly, this energy transport can be shaped in a highly directional fashion using a metallic nanowire [249] (see section 4.3).

Propagating SPPs supported by nanowires (NWs) can be used for the remote excitation of Raman scattering, as has been shown in 2009 by Hutchison et al. in reference 17 and Fang et al. in reference 18. Compared with conventional SERS, remotely excited SERS has several advantages [15]. In conventional SERS, the incident laser light is focused on the target using an objective lens leading to a diffraction-limited excitation volume. In contrast, in remotely excited SERS (see figure 6.1(a)), a Raman scatterer positioned at one end of a metallic nanowire is excited by the propagating SPPs generated by focused laser illumination at the other end of the nanowire. This results in an excited area of nanoscale dimensions formed by the evanescent waves generated by the nanowire's tip and

depending on its size. Remotely excited SERS thus provides a means to isolate heat effects and to avoid the strong background signal originally coming from a substantially larger, diffraction-limited excitation volume. Remote excitation of surface catalytic reactions [20, 21, 22] and Raman detection of biomolecules in vivo in cells [23, 24] are applications already demonstrated for such plasmonic systems.

Raman scattered light generated by local excitation in the vicinity of the nanowire's tip can be expected to be enhanced by the tips near-field generated by LSPs corresponding to local SERS. Importantly, it can also couple to propagating plasmonic modes and be detected at the remote terminal of a nanowire [19]. This remote detection is illustrated in figure 6.1(b). As a result, Raman scattered light at a position different from the laser excitation position, denoted here as "remote SERS", can, in general, consist of two contributions both supported by SPPs, namely remote excitation and remote detection. For a nanowire fully coated with Raman active molecules or for a NW with Raman scatterers present all along the NW, these two contributions cannot be distinguished directly because the position of the contributing Raman emitter is unknown (see figure 6.1(c)).

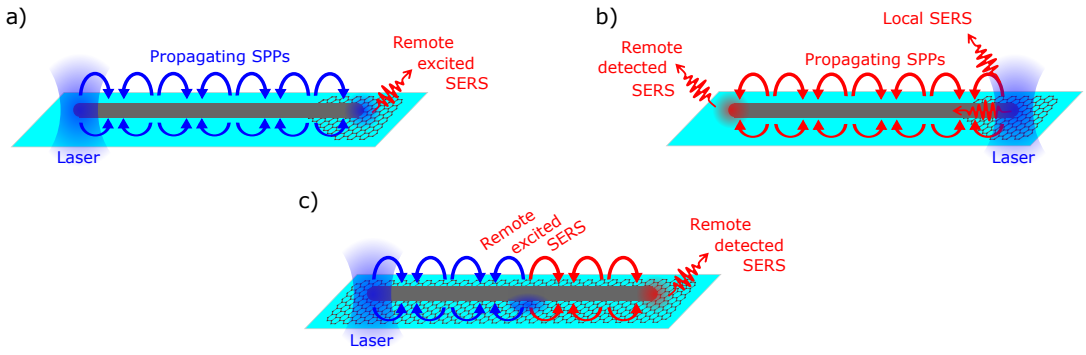

Figure 6.1: Contributions to remote surface-enhanced Raman scattering (SERS). (a) Remote excitation: Focused laser illumination at one termination of the nanowire launches surface plasmon polaritons (SPPs) which travel and scatter out at its distal end, generating a hot spot where graphene is present, therefore resulting in remote excitation of SERS. (b) Remote detection: Direct laser excitation on graphene generates locally excited SERS which can also couple to a propagating plasmonic mode, therefore traveling and scattering out at the distal end of the nanowire, allowing for remote detection of SERS. (c) A combination of both configurations occurs if the nanowire is completely positioned on graphene. Remote excitation can happen at any point along the nanowire, resulting in remoted detected SERS at its distant termination.

In this chapter, remote SERS from graphene using a silver nanowire (Ag NW) as a plasmonic waveguide [16] is demonstrated and studied. Graphene was chosen as a model system because of its strong and well understood Raman response that can readily be detected without surface enhancement [58, 310]. In addition, it is a well defined, uniform material with no variation in thickness, when compared to dye coatings for instance. First, the case of a NW touching the edge of a graphene sheet only with its tip's end is studied.

With this system, demonstrate remote excitation and remote detection of SERS by simultaneously monitoring the spectra at the local and the remote positions is demonstrated. Using this spatio-spectral imaging these two contributions to remote SERS are found to be of comparable intensities. For the general case of a NW fully situated on graphene the contributions of remote excitation and detection would thus be indistinguishable. Therefore, spectrally selective back focal plane imaging is introduced. This technique allows to distinguish the radiation patterns of the different sources. While locally and remotely excited SERS feature dipolar patterns, remotely detected SERS carried by SPPs shows a characteristic line pattern.

6.1 Spatio-spectral imaging demonstration of remote SERS

First, remote excitation and remote detection of SERS from graphene are proven separately. For this, a particular configuration is selected in which one tip of a silver nanowire touches the edge of a graphene sheet. This configuration is sketched in figure 6.1. Focused laser illumination at one terminus of the NW launches propagating SPPs that can reach the other terminus where graphene is present, therefore resulting in remote excitation of SERS [17, 18] (see figure 6.1(a)). Conversely, direct laser excitation of graphene at the nanowire's tip will generate local SERS due to LSPs that enhance both the incident and scattered fields. Surface-enhanced Raman scattered light can thus also couple to a propagating plasmonic mode, traveling and scattering out to the far field at the distal terminus of the NW, allowing for remote detection of SERS [19] (see figure 6.1(b)).

Figure 6.2 experimentally illustrates the remote excitation and detection of Raman scattering from graphene mediated by a silver nanowire. The configuration corresponds to that in Figure 6.1. While the nanowire appears bright in the elastic scattering image (figure 6.2(a)), the graphene sheet absorbs light resulting in a lower intensity of elastically scattered light [102]. The graphene sheet is also visualized by recording Raman scattering images formed by detecting its characteristic Raman bands (figures 6.2(b), (c)).

In the next step the nanowire was imaged onto the CCD camera of the spectrometer using wide-field illumination while setting the grating of the spectrometer to zero order and orienting the nanowire parallel to the entrance slit of the monochromator (figure 6.2(d)) . The laser focus is then positioned at the lower tip of the NW distant from the graphene, as indicated by the red arrow in figure 6.2(d). The polarization of the laser is set parallel to the NW (0°). Once the grating of the spectrometer is used to disperse the light, we obtain the emission spectra for different spatial positions along the nanowire. As can be seen in figure 6.2(e), two positions along the nanowire show strong signals. At the position of the laser focus, indicated by the dashed box labeled "local", a spectrally broad and nearly uniform background signal is detected. This background signal results from inelastic scattering in the glass substrate, the immersion oil, the microscope objective and potentially, fluorescence from the PVP polymer wrapping the Ag NWs (figure 6.2(g)).

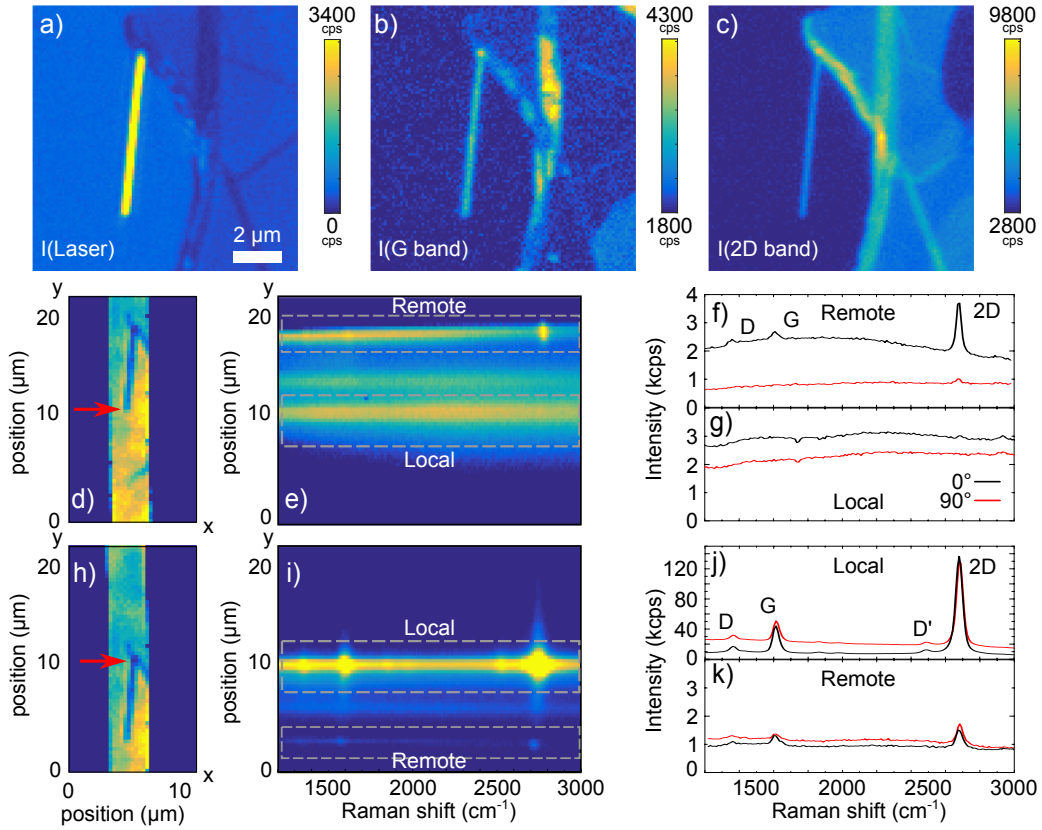

Figure 6.2: Confocal elastic scattering (a), G Raman band (b) and 2D Raman band (c) images of a Ag nanowire on glass in contact with a graphene edge (upper region of the image), recorded upon laser excitation at 633 nm. (d,h) White light transmission images of the Ag nanowire. (e,i) Spatially resolved spectra obtained when the laser is focused on the position indicated by the red arrow in panels d and h, respectively. (f,g,j,k) Spectra obtained by vertically integrating the intensity marked by the dashed box for each wavelength in figures e and i for laser polarization parallel (0°, black line) and perpendicular to the NW (90°, red line). Laser excitation at the nanowire tip without graphene indicated in panel d and detection of the graphene Raman bands at the distal tip in panel f demonstrates remote excitation. Laser excitation at the nanowire tip in the presence of graphene indicated in panel h and detection of the graphene Raman bands at the distal tip in panel f evidences remote detection.

On the other hand, the spectrum detected at the distal end of the nanowire in contact with graphene sheet, features the three distinct Raman bands of graphene (D, G, and 2D bands), as can be seen in Figure 6.2(f). The observation of Raman scattering at a distance of about 7 μm from the excitation point clearly demonstrates the remote excitation of graphene. More precisely, graphene Raman scattering is generated by propagating SPPs reaching the distal tip after being launched by the laser at the input terminus (see Figure 6.1(a)). Setting the laser polarization perpendicular to the NW (90°) (figure 6.2(f)) results in a substantially weaker Raman scattering signal indicating that propagating SPPs are most efficiently excited for laser polarization parallel to the nanowire [246].

Positioning the laser focus at the upper tip of the NW in contact with the graphene sheet generates a Raman response which can emit directly into free space (local scattering, figure 6.2(j)), or, alternatively, can launch propagating SPPs at the Raman frequencies which will scatter out at the other NW end (remote scattering, figure 6.2(k)). Because no graphene is present at the distal end at which the Raman scattering signal is observed, this serves as a clear evidence of remote detection of Raman scattering (figure 6.1(b)).

Remarkably, the strong polarization contrast observed for remote excitation (Figure 6.2(f), (g)) does not occur for remote detection (Figure 6.2(j), (k)). While a degree of polarization [247] $DoP = \frac{I_{0°} - I_{90°}}{I_{0°} + I_{90°}}$ of $> 95\%$ (considering noise) and 83% is obtained for the remote excitation of G and 2D bands, respectively, a DoP of only 17% and $\sim 0\%$ for G and 2D bands is obtained when they are remotely detected. This behaviour can be directly connected to the polarization characteristics of the graphene Raman bands. While the source of G band scattering can be described by the sum of two orthogonal point dipoles and is therefore isotropically polarized, the 2D band can be represented by three point dipoles rotated by 120° with respect to each other [29]. As a result, for both excitation polarizations Raman responses polarized along the NW will be generated which efficiently couple to propagating SPPs, thereby strongly reducing the observed DoP.

It is important to notice that both remotely excited and remotely detected Raman signals show comparable peak intensities on the order of 1000 - 2000 counts per second. Similar results are presented in figure 6.3 for a different NW. Confocal elastic scattering and 2D Raman band images of a Ag nanowire on glass touching a graphene edge are shown in figures 6.3 (a) and (c), respectively, and proof of remote excitation and remote detection of SERS are shown in figures 6.3 (c,d) and (f,g). Spectra for local and remote positions obtained following the procedure explained for figure 6.2. The ratio between remotely excited and remotely detected signal is not the same, as it is expected to depend on the specific shape of the two different NWs terminations. In general, this suggest that the remote detection signal contribution cannot be neglected in remote excitation studies for fully coated NWs, given that it provides a comparable signal intensity.

Concluding the discussion of figures 6.2 and 6.3, remote detection and remote excitation of SERS was observed using a NW connecting to a graphene sheet only with its tip, as sketched in Figure 6.1. For a NW completely positioned on graphene, the Raman signal at the distal end is expected to be composed of remotely exited SERS and remotely detected SERS, as discussed above. However, these two different contributions can not be

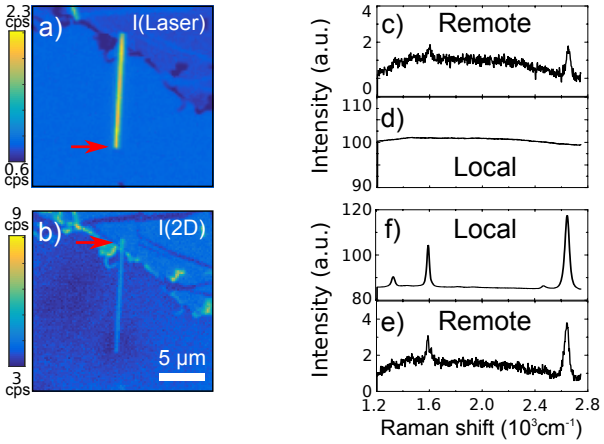

Figure 6.3: Confocal elastic scattering (a) and 2D Raman band (b) images of a Ag nanowire on glass touching a graphene edge, recorded upon laser excitation at 633 nm. Remote excitation of surface-enhanced Raman scattering from graphene is observed at the remote termination of the nanowire (c) after laser illumination of the termination laying on glass (red arrow in panel (a)), where no Raman features are observed (d). Following local excitation of surface-enhanced Raman scattering (f) at the nanowires tip laying on top of graphene (red arrow in (b)), Raman features are remotely detected at the distal termination of the nanowire (e). Spectra for local and remote positions obtained following the procedure explained in Figure 6.2.

distinguished by spectroscopic imaging in a case other than the configuration presented in figure 6.2. In the following section, a more general approach to distinguish the different contributions based on spectrally resolved back focal plane (BFP) imaging will be illustrated.

6.2 Spectrally selective BFP imaging demonstration of remote SERS

In this section, a more general approach to distinguish the different contributions based on spectrally resolved back focal plane (BFP) imaging will be illustrated. BFP imaging allows to quantify the angular distribution of light emitted or scattered by nanoscale objects. It can be used to determine the orientation of dipolar emitters [27], and therefore to investigate the angular photoluminescence [28] and Raman scattering [29] from two dimensional materials, as well as to image the change of the radiation patterns in emitters/scatterers induced by optical antennas [30, 31, 32, 33, 34]. BFP imaging is particularly useful for observing SPPs that render characteristic patterns indicating the direction of SPP propagation and the SPP momentum [35, 36].

In order to demonstrate the coupling of Raman scattering to a propagating plasmonic mode, a configuration similar to the one displayed in Figure 6.1(a,b) is first investigate. Fi-

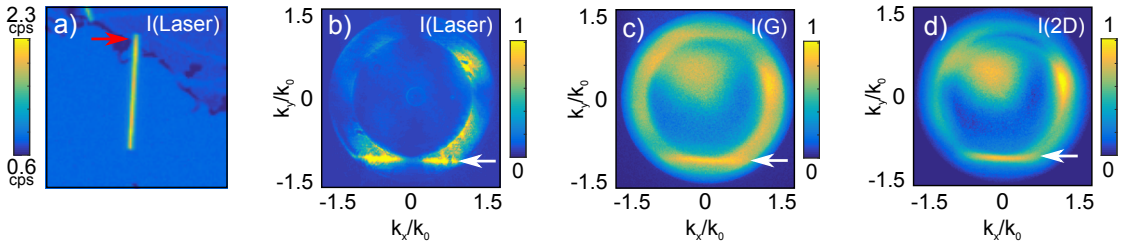

Figure 6.4: Confocal elastic scattering (a) map of a Ag nanowire touching the edge of a graphene sheet with its tip. Back focal plane images showing the wave-vector distributions for laser scattered light (b), G (c) and 2D (d) Raman bands, upon laser excitation at the position marked by the red arrow in (a). The horizontal bright line (white arrow) is recognized as the signature of the leaky mode, showing the coupling of laser (b) and Raman scattered (c,d) light to a propagating plasmonic mode.

gure 6.4(a) show the elastic scattering map of the NW in contact with a graphene sheet only with one tip, which was discussed in previous section (see figure 6.3). Figures 6.4(b,c,d) represent BFP images recorded for excitation at the upper terminus of the NW for the laser, G band and 2D band frequencies. The signature of a leaky SPP mode supported by the NW is recognized in all three patterns as a bright horizontal linear intensity contribution perpendicular to the direction of propagation [250] (see white arrow), evidence for the coupling of laser and Raman scattered light to the NW at the excitation point. For the Raman scattering frequencies, the broad ring-like contribution, distributed over the complete k-space with the majority situated at k vectors larger than k_0, can be understood as the superposition of different signals with dipolar origin (locally excited Raman scattering [29], photoluminescence and Raman scattered light from the polymer wrapping the NWs, etc).

The case of a NW completely laying on graphene is introduced in figure 6.5. Figures 6.5(a,b) show the elastic scattering and G band maps of a nanowire laying on graphene. Figure 6.5(c) show the spectra taken from bare graphene, the left and the right NW's terminals in black, blue and red lines, respectively (color coded, see circles in figure (a)). The laser light is polarized parallel to the long axis of the nanowire. Upon focused laser illumination on the nanowires left terminus, light emission at the laser, G and 2D Raman frequencies from the other extremity, as well as along the nanowire confirms the excitation of an SPP mode (figures 6.5(d,e,f)). Vertical bright lines, as signatures of leaky SPP modes, are observed at both sides of the recorded BFP patterns for frequencies corresponding to the G and 2D bands (figures 6.5(g),(h)). This indicates the presence of SPPs traveling back and forth along the nanowire [237] and can be explained as follows.

When observing the Raman scattering images (figures 6.5(e,f)) of the nanowire upon laser excitation at the left terminus, higher intensity is emitted from the right terminus of the nanowire, in contrast to the elastic scattered light image (figures 6.5(d)). This presumably results from the accumulation of material (i.e. amorphous carbon [311], smaller/broken nanowires, etc.) at the right terminus, resulting in the observed higher intensity when

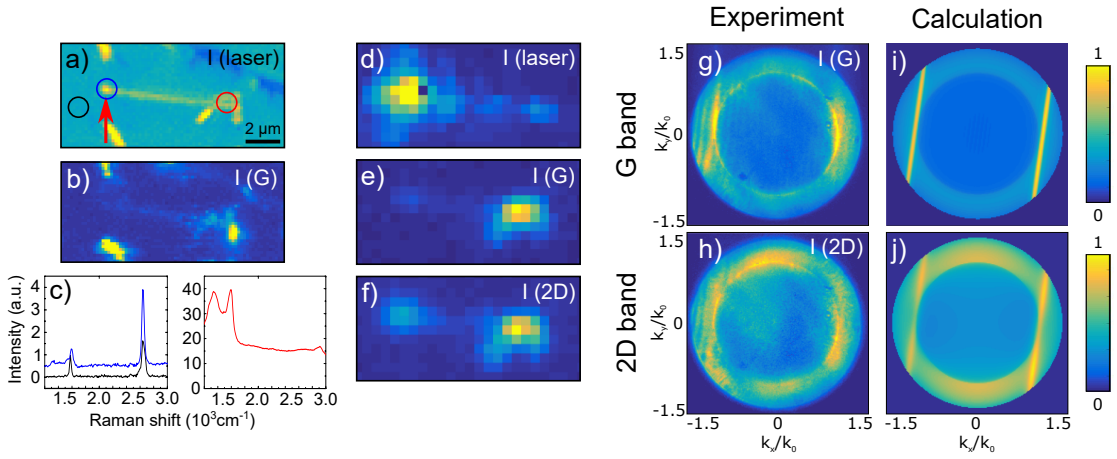

Figure 6.5: Confocal elastic scattering (a) and Raman G band (b) maps of an Ag nanowire on graphene. (c) Spectra taken from bare graphene, the left and the right terminus of the NW (black, blue and red lines, see circles in figure (a)). (c,d,e) Laser, Raman G band and 2D band images, respectively, recorded during local excitation at the left termination of the nanowire (indicated by the red arrow). Accumulation of graphitic material near the right nanowire terminal results in higher Raman scattering intensity. Back focal plane patterns for Raman scattered light at the G (g) and 2D (h) band frequencies, respectively. SPPs propagating in both directions result in vertical lines on both sides of the BFP patterns. The vertical line on the right side is generated by propagating plasmons launched at the left terminal of the nanowire. The vertical line on the left side is due SPPs launched by the strong remotely excited Raman signal from the accumulation of graphitic material at the right terminal. (i,j) Calculated BFP patterns as the sum of a local contribution considering the polarization characteristics of the G and 2D band, respectively, and a contribution from propagating leaky SPPs.

compared to the left terminus (see confocal maps figures 6.5(a,b)) and spectra in figure 6.5(c)). The remotely excited emission of the material accumulation couples to leaky SPP modes traveling back from the right to the left terminal and in this case is strong enough to be detected. In case of a spatially uniform graphene layer this signal contribution will be too weak to be seen. Both counterpropagating SPPs are revealed by the two vertical lines in the BFP images in Figures 6.5(g,h). Figures 6.5(i,j) show calculated BFP patterns consisting of a sum of a local, dipolar contribution reflecting the polarization characteristics of the G and 2D band of graphene [29] and a contribution from leaky SPPs at the respective Raman frequencies travelling in both directions along the nanowire [229]. The calculated BFP patterns reproduce the main features seen in the experimental patterns supporting our identification of propagating SPPs. Here, the amplitudes of the SPP contributions generated by laser excitation at the left terminal and by the accumulation of graphitic material at the right terminal were adjusted to match the experimental result. With these spectrally resolved BFP images we hence demonstrate the NW-mediated remote detection of remotely excited SERS from graphene which further underlines the potential of the approach in sensing applications.

6.3 Conclusions

In this chapter, remote SERS mediated by a silver nanowire was demonstrated. It was proven how its different contributions can be distinguished by applying spatio-spectral and spectrally selective BFP imaging. For this purpose, graphene was used as Raman scatterer because of its strong, uniform and highly stable Raman emission. Starting with particular configurations in which only one NW tip was touching the graphene, it is possible to spectroscopically identify remote excitation and remote detection of SERS leading to similar signal intensities. For cases in which the NW is completely laying on graphene, back focal plane imaging proves to be a powerful tool to identify emission from propagating SPP modes. With this technique the coupling of Raman scattering to plasmonic propagating modes and the remote detection of remotely excited SERS were verified. Remote excitation and remote detection of SERS is a near field effect that only occurs in the vicinity of the nanowire determined by the decay length of the evanescent fields. Remote SERS can thus be exploited for sensing of nanoscale volumes. These results on the identification and distinction of different contributions are important for the future development and applications of remote SERS.

Chapter 7

Summary and conclusions

In the course of this work, confocal and antenna-enhanced spectroscopy and microscopy were employed for the study of graphene and metal-graphene-metal photodetectors.

In chapter 2, the description of the image formation in the back focal plane (BFP) of an objective lens is introduced, and after discussing the typical patterns rendered by point-dipolar emission, the detection efficiency and the polarization contrast are then discussed in terms of the numerical aperture. BFP imaging proved to be a very useful technique because it can be used to determine the orientation of dipolar emitters, and therefore to model the photoluminescence and Raman scattering from low dimensional material systems, as well as to image the change of the radiation patterns in emitters/scatterers induced by optical antennas, providing important information about the coupling between emitter and antenna.

Chapter 3 was dedicated to the study of polarization dependent and angular radiation patterns of Raman scattering from graphene on glass. This showed that Raman scattering can be modeled as point-dipolar emission rather than coming from an extended source. More specifically, the angular distribution of the G and 2D Raman scattering from graphene on glass were experimentally obtained by detecting back focal plane patterns. Calculations showed that the G Raman emission can be described by a superposition of two incoherent orthogonal point dipoles oriented in the graphene plane. Due to double resonant Raman scattering, the 2D emission can be represented by the incoherent sum of either three dipoles oriented 120° with respect to each other or two orthogonal dipoles with emission intensity weighted 3:1. While the G scattering is confirmed to be non-polarized, in the case of the 2D band polarized scattering is observed. The phenomenological Raman tensors suggested according to this experiment are further verified by polarization dependent measurements. The polarization contrast is found to decrease substantially for increasing collection angle, due to polarization mixing caused by the air-dielectric interface. This also influences I(2D)/I(G), a crucial quantity for estimating the doping in graphene. The treatment of the depolarization and the corresponding expression derived for calculating the polarized Raman scattering intensities is expected to be applicable to a wide range of samples including other layered materials, nanotubes, or nanowires. These results are thus important for the quantitative analysis of the Raman intensities in confocal microscopy

with high numerical aperture.

Optical antennas are a powerful tool for manipulating light at the nanometer scale, while also providing efficient control of transduction to the far- field. As these nanoantennas aim to control the optical fields at the nanoscale, they can highly benefit from the plasmonic properties of metallic structures in the optical range. After discussing the main concepts in optical antennas and the basic properties of propagating and localized SPs, the antenna function of gold (Au) dimers and silver nanowires (Ag NWs) were proven by BFP imaging in chapter 4. While the emission from a quantum dot - gold dimer system can be modeled by point-dipolar emission, the scattering at a NW supporting propagating SPPs can be modeled as the emission from a chain of dipoles with appropriate relative phase retardation. This shows that BFP imaging can provide information about the coupling between emitter and metallic nanoparticle by comparing the experimental patterns with the calculated patterns, as expected for radiation emitted through the antenna or directly radiated to the far-field.

In chapter 5 simultaneous near-field Raman, photocurrent and topography images were recorded on metal-graphene-metal devices by making use of tip-enhanced near-field microscopy (TENOM). A clear photocurrent near-field contribution was observed from the steeper slope of the signal at the electrode's edges, as well as several subdiffraction modulations in both photocurrent and Raman signals. However, the near-field contribution is too weak when compared to the far-field contribution, therefore hindering the clear identification of correlation between the different recorded signals. This points out the necessity of improving this technique when two-dimensional material systems are to be investigated. A new approach, based on near-field / far-field separation via tip-sample distance modulation is then suggested. As mentioned, this approach has already proven successful in improving the signal to background ratio after removing the far-field photoluminescence signal from carbon nanotubes. This technique will be specially useful for the study of two-dimensional materials in which the far-field contribution comes from an extended area in contrast to one or zero-dimensional materials.

In chapter 6, remote SERS from graphene mediated by a silver nanowire was demonstrated. Its different contributions can be distinguished by applying spatio-spectral and spectrally selective BFP imaging. For this purpose, graphene was used as Raman scatterer because of its strong, uniform and highly stable Raman emission. Starting with particular configurations in which only one NW tip was touching the graphene, it is possible to spectroscopically identify remote excitation and remote detection of SERS leading to similar signal intensities. For cases in which the NW is completely laying on graphene, back focal plane imaging proves to be a powerful tool to identify emission from propagating SPP modes. With this technique the coupling of Raman scattering to plasmonic propagating modes and the remote detection of remotely excited SERS were verified. Remote excitation and remote detection of SERS is a near-field effect that only occurs in the vicinity of the nanowire determined by the decay length of the evanescent fields. Remote SERS can thus be exploited for sensing of nanoscale volumes. These results on the identification and distinction of different contributions are important for the future development and applications of remote SERS.

Finally, two general conclusions can be extracted from this work. On the one hand, the investigation of fundamental processes in graphene can highly benefit from antenna-enhanced approaches. While the high spatial resolution of tip-enhanced near-field microscopy allows for the characterization of materials and devices at the nanoscale, nanowire-based remote spectroscopy enables spectroscopy investigations of nanosized volumes, both techniques revealing phenomena in ranges not accessible with confocal microscopy or spectroscopy. On the other hand, basic research on optical antennas and plasmonic processes can take advantage of using graphene as a model system. Graphene was chosen because of its strong and well understood Raman and photocurrent response that can readily be detected without surface enhancement. In addition, it is a well defined, uniform material with no variation in thickness, when compared to other materials, perfect for antenna-enhanced experiments.

Appendix A

Fabrication of graphene samples

During this work, different graphene samples were used. The experiments in chapters 3, 5, and 6 were performed with graphene fabricated by Jürgen Kraus and Prof. Sebastian Günther at the TUM / LMU Munich by the chemical vapor deposition (CVD) method. The procedure is detailed in section A.1. The experiments in section 3.2 were performed with a graphene sample fabricated by Antonio Lombardo in Prof. A. C. Ferrari's group in the graphene center (Cambridge, UK) by micromechanical cleavage. The procedure is detailed in section A.2. The sample used in 3.1.1 were fabricated at Graphenea (San Sebastian, Spain).

A.1 CVD growth and transfer

For graphene growth, circa 1x1 cm^2 pieces were cut from as received Cu-foil (25 μm, Alfa Aesar 46986, 99.8%) and loaded into a quartz tube reactor. After evacuating the reactor system (to circa 10-3 mbar) the Cu-foils were heated up from room temperature to 950°C in a flow of hydrogen ($p(H_2) = 1$ mbar) within 40 min. For oxidative carbon removal the Cu foil was exposed to a highly diluted oxygen flow in an argon carrier gas ($p(O_2) \approx 10^{?5}$ mbar in $p(Ar) = 1$ mbar) [312]. After 60 min the temperature was increased to 1075°C and the gas flow was changed to graphene growth conditions ($p(H_2) = 20$ mbar, $p(CH_4) = 0.02$ mbar) followed by a 2.5 h growth period. Graphene growth was stopped by quickly pulling the Cu-foils out of the hight temperature zone of the reactor. For the transfer of the as grown graphene films the Cu-samples were spincoated with PMMA solution (6 wt. % in Anisole). After drying the PMMA-protected graphene film was released from the Cu-support by bubbling transfer [313]. The detached graphene PMMA film was washed with deionized water and then transferred onto the target glass substrates. Finally the PMMA protection layer was removed with hot acetone.

A.2 Cleavage and transfer

Graphene layers are deposited by micromechanical cleavage [52] on Si wafers covered with 300nm of SiO_2. SLGs are identified by a combination of optical microscopy [71] and Raman spectroscopy [Renishaw microRaman at 514,633nm] [77, 59]. SLGs are transferred onto glass by a polymer-based wet transfer process [314]. PMMA (molecular weight 950K) is spin coated onto the substrate where graphite flakes are exfoliated, then the sample is immersed in de-ionized water, resulting in the detachment of the polymer film due to water intercalation at the PMMA-SiO_2 interface [314, 315]. The flakes attach to the polymer and can be removed from the Si/SiO_2 substrate. The polymer+graphene film is then placed onto the glass substrate and, after complete drying of the water, PMMA is removed by acetone. Success of the transfer is confirmed both optically and by Raman spectroscopy. No significant D peak is detected after transfer, showing that the process does not result in structural defects.

Bibliography

[1] M. Allen, J. W. Allen, D. M. Wasserman, G. P. Kumar, and S. A. Maier, "Special section guest editorial: Plasmonics systems and applications," *Optical Engineering*, vol. 56, no. 12, p. 121900, 2017.

[2] E. Di Fabrizio, S. Schlücker, J. Wenger, R. Regmi, H. Rigneault, G. Calafiore, M. West, S. Cabrini, M. Fleischer, N. F. Van Hulst, *et al.*, "Roadmap on biosensing and photonics with advanced nano-optical methods," *Journal of Optics*, vol. 18, no. 6, p. 063003, 2016.

[3] H. A. Atwater, "The promise of plasmonics," *Scientific American*, vol. 296, no. 4, pp. 56–62, 2007.

[4] L. Novotny and B. Hecht, *Principles of nano-optics*. Cambridge university press, 2012.

[5] S. A. Maier, *Plasmonics: Fundamentals and applications*. Springer Science & Business Media, 2007.

[6] R. Zia, J. A. Schuller, A. Chandran, and M. L. Brongersma, "Plasmonics: the next chip-scale technology," *Materials today*, vol. 9, no. 7-8, pp. 20–27, 2006.

[7] E. Ozbay, "Plasmonics: merging photonics and electronics at nanoscale dimensions," *science*, vol. 311, no. 5758, pp. 189–193, 2006.

[8] S.-Y. Ding, E.-M. You, Z.-Q. Tian, and M. Moskovits, "Electromagnetic theories of surface-enhanced raman spectroscopy," *Chem. Soc. Rev.*, vol. 46, no. 13, pp. 4042–4076, 2017.

[9] N. Mauser and A. Hartschuh, "Tip-enhanced near-field optical microscopy," *Chemical Society Reviews*, vol. 43, no. 4, pp. 1248–1262, 2014.

[10] M. Moskovits, "Persistent misconceptions regarding sers," *Phys. Chem. Chem. Phys.*, vol. 15, no. 15, pp. 5301–5311, 2013.

[11] K. Kneipp, Y. Wang, H. Kneipp, L. Perelman, I. Itzkan, R. Dasari, and M. Feld, "Single molecule detection using surface-enhanced raman scattering (sers)," *Phys. Rev. Lett.*, vol. 78, pp. 1667–1670, 1997.

[12] H. Xu, E. J. Bjerneld, M. Käll, and L. Börjesson, "Spectroscopy of single hemoglobin molecules by surface enhanced raman scattering," *Phys. Rev. Lett.*, vol. 83, pp. 4357–4360, Nov 1999.

[13] J. A. Dieringer, R. B. Lettan II, K. A. Scheidt, and R. P. Van Duyne, "A frequency domain existence proof of single-molecule surface-enhanced Raman spectroscopy," *J. Am. Chem. Soc.*, vol. 129, pp. 16249–16256, 2008.

[14] A. Hartschuh, "Tip-enhanced near-field optical microscopy," *Angew. Chem. Int. Ed.*, vol. 47, no. 43, pp. 8178–8191, 2008.

[15] Y. Huang, Y. Fang, Z. Zhang, L. Zhu, and M. Sun, "Nanowire-supported plasmonic waveguide for remote excitation of surface-enhanced raman scattering," *Light Sci. Appl.*, vol. 3, no. 8, p. e199, 2014.

[16] H. Wei, D. Pan, S. Zhang, Z. Li, Q. Li, N. Liu, W. Wang, and H. Xu, "Plasmon waveguiding in nanowires," *Chemical reviews*, 2018.

[17] J. A. Hutchison, S. P. Centeno, H. Odaka, H. Fukumura, J. Hofkens, and H. Uji-i, "Subdiffraction limited, remote excitation of surface enhanced raman scattering," *Nano Lett.*, vol. 9, no. 3, pp. 995–1001, 2009. PMID: 19199757.

[18] Y. Fang, H. Wei, F. Hao, P. Nordlander, and H. Xu, "Remote-excitation surface-enhanced raman scattering using propagating ag nanowire plasmons," *Nano Lett.*, vol. 9, no. 5, pp. 2049–2053, 2009. PMID: 19391601.

[19] M. Sun, Y. Hou, and H. Xu, "Can information of chemical reaction propagate with plasmonic waveguide and be detected at remote terminal of nanowire?," *Nanoscale*, vol. 3, no. 10, pp. 4114–4116, 2011.

[20] M. Sun, Y. Hou, Z. Li, L. Liu, and H. Xu, "Remote excitation polarization-dependent surface photochemical reaction by plasmonic waveguide," *Plasmonics*, vol. 6, no. 4, p. 681, 2011.

[21] S. J. Lee and M. Moskovits, "Remote sensing by plasmonic transport," *J. Am. Chem. Soc.*, vol. 134, no. 28, pp. 11384–11387, 2012.

[22] Z. Zhang, Y. Fang, W. Wang, L. Chen, and M. Sun, "Propagating surface plasmon polaritons: towards applications for remote-excitation surface catalytic reactions," *Adv. Sci.*, vol. 3, no. 1, 2016.

[23] R. Yan, J.-H. Park, Y. Choi, C.-J. Heo, S.-M. Yang, L. P. Lee, and P. Yang, "Nanowire-based single-cell endoscopy," *Nat. Nanotechnol.*, vol. 7, no. 3, pp. 191–196, 2012.

[24] G. Lu, H. De Keersmaecker, L. Su, B. Kenens, S. Rocha, E. Fron, C. Chen, P. Van Dorpe, H. Mizuno, J. Hofkens, J. A. Hutchison, and H. Uji-i, "Live-cell sers endoscopy using plasmonic nanowire waveguides," *Adv. Mater.*, vol. 26, no. 30, pp. 5124–5128, 2014.

[25] E. Descrovi, E. Barakat, A. Angelini, P. Munzert, N. De Leo, L. Boarino, F. Giorgis, and H. P. Herzig, "Leakage radiation interference microscopy," *Optics letters*, vol. 38, no. 17, pp. 3374–3376, 2013.

[26] C. Huang, A. Bouhelier, G. C. des Francs, A. Bruyant, A. Guenot, E. Finot, J.-C. Weeber, and A. Dereux, "Gain, detuning, and radiation patterns of nanoparticle optical antennas," *Physical Review B*, vol. 78, no. 15, p. 155407, 2008.

[27] M. A. Lieb, J. M. Zavislan, and L. Novotny, "Single-molecule orientations determined by direct emission pattern imaging," *JOSA B*, vol. 21, no. 6, pp. 1210–1215, 2004.

[28] J. A. Schuller, S. Karaveli, T. Schiros, K. He, S. Yang, I. Kymissis, J. Shan, and R. Zia, "Orientation of luminescent excitons in layered nanomaterials," *Nat. nanotechnol.*, vol. 8, no. 4, pp. 271–276, 2013.

[29] H. Budde, N. Coca-López, X. Shi, R. Ciesielski, A. Lombardo, D. Yoon, A. C. Ferrari, and A. Hartschuh, "Raman radiation patterns of graphene," *ACS Nano*, vol. 10, no. 2, pp. 1756–1763, 2016. PMID: 26651030.

[30] S. Kühn, G. Mori, M. Agio, and V. Sandoghdar, "Modification of single molecule fluorescence close to a nanostructure: radiation pattern, spontaneous emission and quenching," *Mol. Phys.*, vol. 106, no. 7, pp. 893–908, 2008.

[31] T. Taminiau, F. Stefani, F. B. Segerink, and N. Van Hulst, "Optical antennas direct single-molecule emission," *Nat. Photonics*, vol. 2, no. 4, pp. 234–237, 2008.

[32] T. H. Taminiau, F. Stefani, and N. F. van Hulst, "Single emitters coupled to plasmonic nano-antennas: angular emission and collection efficiency," *New J. Phys.*, vol. 10, no. 10, p. 105005, 2008.

[33] M. Böhmler, N. Hartmann, C. Georgi, F. Hennrich, A. A. Green, M. C. Hersam, and A. Hartschuh, "Enhancing and redirecting carbon nanotube photoluminescence by an optical antenna," *Opt. express*, vol. 18, no. 16, pp. 16443–16451, 2010.

[34] A. G. Curto, G. Volpe, T. H. Taminiau, M. P. Kreuzer, R. Quidant, and N. F. van Hulst, "Unidirectional emission of a quantum dot coupled to a nanoantenna," *Science*, vol. 329, no. 5994, pp. 930–933, 2010.

[35] A. Drezet, A. Hohenau, D. Koller, A. Stepanov, H. Ditlbacher, B. Steinberger, F. Aussenegg, A. Leitner, and J. Krenn, "Leakage radiation microscopy of surface plasmon polaritons," *Mater. sci. eng. B*, vol. 149, no. 3, pp. 220–229, 2008.

[36] M. Song, A. Bouhelier, P. Bramant, J. Sharma, E. Dujardin, D. Zhang, and G. Colas-des Francs, "Imaging symmetry-selected corner plasmon modes in penta-twinned crystalline ag nanowires," *ACS Nano*, vol. 5, no. 7, pp. 5874–5880, 2011. PMID: 21682318.

[37] S. Otsuki, N. Murase, and H. Kano, "Back focal plane microscopic ellipsometer with internal reflection geometry," *Optics Communications*, vol. 294, pp. 24–28, 2013.

[38] M. Neugebauer, P. Woźniak, A. Bag, G. Leuchs, and P. Banzer, "Polarization-controlled directional scattering for nanoscopic position sensing," *Nature communications*, vol. 7, p. 11286, 2016.

[39] J. D. Jackson, *Electrodynamics*. Wiley Online Library, 1975.

[40] L. Novotny and B. Hecht, *Principles of nano-optics*. Cambridge university press, 2012.

[41] N. Hartmann, *Coupling of emitters to surface plasmons investigated by back focal plane microscopy*. PhD thesis, lmu, 2013.

[42] L. Novotny, "Allowed and forbidden light in near-field optics. i. a single dipolar light source," *JOSA A*, vol. 14, no. 1, pp. 91–104, 1997.

[43] H. Weyl, "Ausbreitung elektromagnetischer wellen über einem ebenen leiter," *Annalen der Physik*, vol. 365, no. 21, pp. 481–500, 1919.

[44] N. Hartmann, G. Piredda, J. Berthelot, G. Colas des Francs, A. Bouhelier, and A. Hartschuh, "Launching propagating surface plasmon polaritons by a single carbon nanotube dipolar emitter," *Nano letters*, vol. 12, no. 1, pp. 177–181, 2011.

[45] A. Sommerfeld, "Über die ausbreitung der wellen in der drahtlosen telegraphie," *Annalen der Physik*, vol. 333, no. 4, pp. 665–736, 1909.

[46] H. von Hoerschelmann, *Uber die Wirkungsweise des geknickten Marconischen Senders in der drahtlosen Telegraphie*. Konigl. Bayr. Ludwig-Maximilians-Universitat zu Munchen., 1911.

[47] A. Sommerfeld, "Über die ausbreitung der wellen in der drahtlosen telegraphie," *Annalen der Physik*, vol. 386, no. 25, pp. 1135–1153, 1926.

[48] C. Fattinger and W. Lukosz, "Optical-environment-dependent lifetimes and radiation patterns of luminescent centers in very thin films," *Journal of Luminescence*, vol. 31, pp. 933–935, 1984.

[49] B. Hecht, D. W. Pohl, H. Heinzelmann, and L. Novotny, ""tunnel" near-field optical microscopy: Tnom-2," *Ultramicroscopy*, vol. 61, no. 1-4, pp. 99–104, 1995.

[50] M. Böhmler, *Tip-enhanced near-field optical microscopy on the quasi 1D semiconductors carbon nanotubes and CdSe nanowires*. PhD thesis, lmu, 2012.

[51] H. Budde, *Raman radiation studies of nanocarbon materials*. PhD thesis, lmu, 2016.

[52] K. S. Novoselov, A. K. Geim, S. V. Morozov, D. Jiang, Y. Zhang, S. V. Dubonos, I. V. Grigorieva, and A. A. Firsov, "Electric field effect in atomically thin carbon films," *science*, vol. 306, no. 5696, pp. 666–669, 2004.

[53] M. S. Dresselhaus, G. Dresselhaus, R. Saito, and A. Jorio, "Raman spectroscopy of carbon nanotubes," *Physics reports*, vol. 409, no. 2, pp. 47–99, 2005.

[54] R. Saito, G. Dresselhaus, and M. S. Dresselhaus, *Physical properties of carbon nanotubes*. World Scientific, 1998.

[55] F. Tuinstra and J. L. Koenig, "Raman spectrum of graphite," *The Journal of Chemical Physics*, vol. 53, no. 3, pp. 1126–1130, 1970.

[56] F. Tuinstra and J. Koenig, "Characterization of graphite fiber surfaces with raman spectroscopy," *Journal of Composite Materials*, vol. 4, no. 4, pp. 492–499, 1970.

[57] R. J. Nemanich and S. Solin, "First-and second-order raman scattering from finite-size crystals of graphite," *Physical Review B*, vol. 20, no. 2, p. 392, 1979.

[58] L. Malard, M. Pimenta, G. Dresselhaus, and M. Dresselhaus, "Raman spectroscopy in graphene," *Physics Reports*, vol. 473, no. 5, pp. 51–87, 2009.

[59] A. C. Ferrari and D. M. Basko, "Raman spectroscopy as a versatile tool for studying the properties of graphene," *Nature nanotechnology*, vol. 8, no. 4, pp. 235–246, 2013.

[60] D. Yoon, H. Moon, Y.-W. Son, G. Samsonidze, B. H. Park, J. B. Kim, Y. Lee, and H. Cheong, "Strong polarization dependence of double-resonant raman intensities in graphene," *Nano letters*, vol. 8, no. 12, pp. 4270–4274, 2008.

[61] C. V. Raman and K. S. Krishnan, "A new type of secondary radiation," *Nature*, vol. 121, pp. 501–502, 1928.

[62] G. S. Landsberg and L. I. Mandelshtam, "Eine neue erscheinung bei der lichtzerstreuung in krystallen," *Naturwissenschaften*, vol. 16, no. 557, 1928.

[63] J. R. Ferraro, *Introductory raman spectroscopy*. Academic press, 2003.

[64] F. Tuinstra and J. L. Koenig, "Raman spectrum of graphite," *J. Chem. Phys.*, vol. 53, pp. 1126–1130, 1970.

[65] A. C. Ferrari and J. Robertson, *Raman spectroscopy in carbons: from nanotubes to diamond*. JSTOR, 2004.

[66] A. C. Ferrari, F. Bonaccorso, V. Fal'Ko, K. S. Novoselov, S. Roche, P. Bøggild, S. Borini, F. H. Koppens, V. Palermo, N. Pugno, *et al.*, "Science and technology roadmap for graphene, related two-dimensional crystals, and hybrid systems," *Nanoscale*, vol. 7, no. 11, pp. 4598–4810, 2015.

[67] A. Ferrari and J. Robertson, "Resonant raman spectroscopy of disordered, amorphous, and diamondlike carbon," *Physical Review B*, vol. 64, no. 7, p. 075414, 2001.

[68] A. C. Ferrari and J. Robertson, "Interpretation of raman spectra of disordered and amorphous carbon," *Physical review B*, vol. 61, no. 20, p. 14095, 2000.

[69] A. C. Ferrari, "Raman spectroscopy of graphene and graphite: disorder, electron–phonon coupling, doping and nonadiabatic effects," *Solid state communications*, vol. 143, no. 1, pp. 47–57, 2007.

[70] M. Y. Sfeir, T. Beetz, F. Wang, L. Huang, X. H. Huang, M. Huang, J. Hone, S. O'brien, J. Misewich, T. F. Heinz, *et al.*, "Optical spectroscopy of individual single-walled carbon nanotubes of defined chiral structure," *Science*, vol. 312, no. 5773, pp. 554–556, 2006.

[71] C. Casiraghi, A. Hartschuh, E. Lidorikis, H. Qian, H. Harutyunyan, T. Gokus, K. Novoselov, and A. Ferrari, "Rayleigh imaging of graphene and graphene layers," *Nano letters*, vol. 7, no. 9, pp. 2711–2717, 2007.

[72] P. Blake, E. Hill, A. Castro Neto, K. Novoselov, D. Jiang, R. Yang, T. Booth, and A. Geim, "Making graphene visible," *Applied Physics Letters*, vol. 91, no. 6, p. 063124, 2007.

[73] K. Novoselov, D. Jiang, F. Schedin, T. Booth, V. Khotkevich, S. Morozov, and A. Geim, "Two-dimensional atomic crystals," *Proceedings of the National Academy of Sciences of the United States of America*, vol. 102, no. 30, pp. 10451–10453, 2005.

[74] P. Y. Yu and M. Cardona, *Fundamentals of semiconductors: physics and materials properties*. Springer, 2010.

[75] D. Basko, S. Piscanec, and A. Ferrari, "Electron-electron interactions and doping dependence of the two-phonon raman intensity in graphene," *Physical Review B*, vol. 80, no. 16, p. 165413, 2009.

[76] K.-i. Sasaki, K. Kato, Y. Tokura, S. Suzuki, and T. Sogawa, "Decay and frequency shift of both intervalley and intravalley phonons in graphene: Dirac-cone migration," *Physical Review B*, vol. 86, no. 20, p. 201403, 2012.

[77] A. C. Ferrari, J. Meyer, V. Scardaci, C. Casiraghi, M. Lazzeri, F. Mauri, S. Piscanec, D. Jiang, K. Novoselov, S. Roth, *et al.*, "Raman spectrum of graphene and graphene layers," *Physical review letters*, vol. 97, no. 18, p. 187401, 2006.

[78] R. Beams, L. G. Cançado, and L. Novotny, "Raman characterization of defects and dopants in graphene," *Journal of Physics: Condensed Matter*, vol. 27, no. 8, p. 083002, 2015.

[79] T. Mohiuddin, A. Lombardo, R. Nair, A. Bonetti, G. Savini, R. Jalil, N. Bonini, D. Basko, C. Galiotis, N. Marzari, *et al.*, "Uniaxial strain in graphene by raman spectroscopy: G peak splitting, grüneisen parameters, and sample orientation," *Physical Review B*, vol. 79, no. 20, p. 205433, 2009.

[80] Z. H. Ni, T. Yu, Y. H. Lu, Y. Y. Wang, Y. P. Feng, and Z. X. Shen, "Uniaxial strain on graphene: Raman spectroscopy study and band-gap opening," *ACS nano*, vol. 2, no. 11, pp. 2301–2305, 2008.

[81] O. Frank, M. Mohr, J. Maultzsch, C. Thomsen, I. Riaz, R. Jalil, K. S. Novoselov, G. Tsoukleri, J. Parthenios, K. Papagelis, *et al.*, "Raman 2d-band splitting in graphene: theory and experiment," *Acs Nano*, vol. 5, no. 3, pp. 2231–2239, 2011.

[82] T. Yu, Z. Ni, C. Du, Y. You, Y. Wang, and Z. Shen, "Raman mapping investigation of graphene on transparent flexible substrate: the strain effect," *The Journal of Physical Chemistry C*, vol. 112, no. 33, pp. 12602–12605, 2008.

[83] A. Das, S. Pisana, B. Chakraborty, S. Piscanec, S. K. Saha, U. V. Waghmare, K. S. Novoselov, H. R. Krishnamurthy, A. K. Geim, A. C. Ferrari, and A. K. Sood, "Monitoring dopants by raman scattering in an electrochemically top-gated graphene transistor," *Nature Nanotechnology*, vol. 3, pp. 210–215, 2008.

[84] A. Jorio, A. Souza Filho, G. Dresselhaus, M. Dresselhaus, A. Swan, M. Ünlü, B. Goldberg, M. Pimenta, J. Hafner, C. Lieber, *et al.*, "G-band resonant raman study of 62 isolated single-wall carbon nanotubes," *Physical Review B*, vol. 65, no. 15, p. 155412, 2002.

[85] L. Cançado, A. Reina, J. Kong, and M. Dresselhaus, "Geometrical approach for the study of g' band in the raman spectrum of monolayer graphene, bilayer graphene, and bulk graphite," *Physical Review B*, vol. 77, no. 24, p. 245408, 2008.

[86] C. Thomsen and S. Reich, "Double resonant raman scattering in graphite," *Physical review letters*, vol. 85, no. 24, p. 5214, 2000.

[87] R. Saito, A. Jorio, A. Souza Filho, G. Dresselhaus, M. Dresselhaus, and M. Pimenta, "Probing phonon dispersion relations of graphite by double resonance raman scattering," *Physical review letters*, vol. 88, no. 2, p. 027401, 2001.

[88] M. Pimenta, G. Dresselhaus, M. S. Dresselhaus, L. Cancado, A. Jorio, and R. Saito, "Studying disorder in graphite-based systems by raman spectroscopy," *Physical chemistry chemical physics*, vol. 9, no. 11, pp. 1276–1290, 2007.

[89] A. Eckmann, A. Felten, A. Mishchenko, L. Britnell, R. Krupke, K. S. Novoselov, and C. Casiraghi, "Probing the nature of defects in graphene by raman spectroscopy," *Nano letters*, vol. 12, no. 8, pp. 3925–3930, 2012.

[90] M. M. Lucchese, F. Stavale, E. M. Ferreira, C. Vilani, M. Moutinho, R. B. Capaz, C. Achete, and A. Jorio, "Quantifying ion-induced defects and raman relaxation length in graphene," *Carbon*, vol. 48, no. 5, pp. 1592–1597, 2010.

[91] L. G. Cançado, A. Jorio, E. Martins Ferreira, F. Stavale, C. Achete, R. Capaz, M. Moutinho, A. Lombardo, T. Kulmala, and A. Ferrari, "Quantifying defects in graphene via raman spectroscopy at different excitation energies," *Nano letters*, vol. 11, no. 8, pp. 3190–3196, 2011.

[92] P. Lespade, A. Marchand, M. Couzi, and F. Cruege, "Caracterisation de materiaux carbones par microspectrometrie raman," *Carbon*, vol. 22, no. 4-5, pp. 375–385, 1984.

[93] L. Cancado, M. Pimenta, B. Neves, M. Dantas, and A. Jorio, "Influence of the atomic structure on the raman spectra of graphites," *Physical review letters*, vol. 93, no. 24, p. 247401, 2004.

[94] C. Casiraghi, A. Hartschuh, H. Qian, S. Piscanec, C. Georgi, A. Fasoli, K. S. Novoselov, D. M. Basko, and A. C. Ferrari, "Raman spectroscopy of graphene edges," *Nano Letters*, vol. 9, pp. 1433–1441, 2009.

[95] R. Beams, L. G. Cançado, and L. Novotny, "Low temperature raman study of the electron coherence length near graphene edges," *Nano letters*, vol. 11, no. 3, pp. 1177–1181, 2011.

[96] P. Tan, W. Han, W. Zhao, Z. Wu, K. Chang, H. Wang, Y. Wang, N. Bonini, N. Marzari, N. Pugno, *et al.*, "The shear mode of multilayer graphene," *Nature materials*, vol. 11, no. 4, pp. 294–300, 2012.

[97] K. Sato, J. S. Park, R. Saito, C. Cong, T. Yu, C. H. Lui, T. F. Heinz, G. Dresselhaus, and M. S. Dresselhaus, "Raman spectra of out-of-plane phonons in bilayer graphene," *Physical Review B*, vol. 84, no. 3, p. 035419, 2011.

[98] C. H. Lui, L. M. Malard, S. Kim, G. Lantz, F. E. Laverge, R. Saito, and T. F. Heinz, "Observation of layer-breathing mode vibrations in few-layer graphene through combination raman scattering," *Nano letters*, vol. 12, no. 11, pp. 5539–5544, 2012.

[99] H. Jang, Y. J. Park, X. Chen, T. Das, M.-S. Kim, and J.-H. Ahn, "Graphene-based flexible and stretchable electronics," *Advanced Materials*, vol. 28, pp. 4184–4202, 2016.

[100] R. Sahin, E. Simsek, and S. Akturk, "Nanoscale patterning of graphene through femtosecond laser ablation," *Applied Physics Letters*, vol. 104, p. 053118, 2014.

[101] Z. Lin, X. Ye, J. Han, Q. Chen, P. Fan, H. Zhang, D. Xie, H. Zhu, and M. Zhong, "Precise control of the number of layers of graphene by picosecond laser thinning," *Scientific Reports*, vol. 5, 2015.

[102] K. F. Mak, M. Y. Sfeir, Y. Wu, C. H. Lui, J. A. Misewich, and T. F. Heinz, "Measurement of the optical conductivity of graphene," *Phys. Rev. Lett.*, vol. 101, pp. 196405–4, 2008.

[103] A. G. Curto, T. H. Taminiau, G. Volpe, M. P. Kreuzer, R. Quidant, and N. F. Van Hulst, "Multipolar radiation of quantum emitters with nanowire optical antennas," *Nature communications*, vol. 4, p. 1750, 2013.

[104] B. Hecht, H. Bielefeldt, L. Novotny, Y. Inouye, and D. Pohl, "Local excitation, scattering, and interference of surface plasmons," *Physical review letters*, vol. 77, no. 9, p. 1889, 1996.

[105] H. Budde, N. Coca-López, X. Shi, R. Ciesielski, A. Lombardo, D. Yoon, A. C. Ferrari, and A. Hartschuh, "Raman radiation patterns of graphene," *ACS nano*, vol. 10, no. 2, pp. 1756–1763, 2015.

[106] S. Sahoo, R. Palai, and R. Katiyar, "Polarized raman scattering in monolayer, bilayer, and suspended bilayer graphene," *Journal of Applied Physics*, vol. 110, no. 4, p. 044320, 2011.

[107] V. N. Popov and P. Lambin, "Theoretical polarization dependence of the two-phonon double-resonant raman spectra of graphene," *arXiv preprint arXiv:1206.3827*, 2012.

[108] R. V. Maximiano, R. Beams, L. Novotny, A. Jorio, and L. G. Cançado, "Mechanism of near-field raman enhancement in two-dimensional systems," *Phys. Rev. B*, vol. 85, p. 235434, Jun 2012.

[109] L. G. Cançado, R. Beams, A. Jorio, and L. Novotny, "Theory of spatial coherence in near-field raman scattering," *Physical Review X*, vol. 4, no. 3, p. 031054, 2014.

[110] P. Tan, C. Hu, J. Dong, W. Shen, and B. Zhang, "Polarization properties, high-order raman spectra, and frequency asymmetry between stokes and anti-stokes scattering of raman modes in a graphite whisker," *Phys. Rev. B*, vol. 64, p. 214301, Nov 2001.

[111] R. Loudon, "The raman effect in crystals," *Advances in Physics*, vol. 13, no. 52, pp. 423–482, 1964.

[112] A. Baranov, A. Bekhterev, Y. S. Bobovich, and V. Petrov, "Interpretation of certain characteristics in raman spectra of graphite and glassy carbon," *Opt. Spektrosk*, vol. 62, p. 1036, 1987.

[113] L. G. Cançado, R. Beams, A. Jorio, and L. Novotny, "Theory of spatial coherence in near-field raman scattering," *Phys. Rev. X*, vol. 4, p. 031054, Sep 2014.

[114] R. Beams, L. G. Cançado, S.-H. Oh, A. Jorio, and L. Novotny, "Spatial coherence in near-field raman scattering," *Phys. Rev. Lett.*, vol. 113, p. 186101, Oct 2014.

[115] T. Wilson and R. Juskaitis, "The axial response of confocal microscopes with high numerical aperture objective lenses," *Bioimaging*, vol. 3, no. 1, pp. 35–38, 1995.

[116] W. T. Tang, E. Chung, Y.-H. Kim, P. T. So, and C. J. Sheppard, "Investigation of the point spread function of surface plasmon-coupled emission microscopy," *Optics express*, vol. 15, no. 8, pp. 4634–4646, 2007.

[117] S. Pisana, M. Lazzeri, C. Casiraghi, K. S. Novoselov, A. K. Geim, A. C. Ferrari, and F. Mauri, "Breakdown of the adiabatic born–oppenheimer approximation in graphene," *Nature materials*, vol. 6, no. 3, pp. 198–201, 2007.

[118] A. Grüneis, R. Saito, G. G. Samsonidze, T. Kimura, M. A. Pimenta, A. Jorio, A. G. S. Filho, G. Dresselhaus, and M. S. Dresselhaus, "Inhomogeneous optical absorption around the k point in graphite and carbon nanotubes," *Phys. Rev. B*, vol. 67, p. 165402, Apr 2003.

[119] D. L. Mafra, G. Samsonidze, L. M. Malard, D. C. Elias, J. C. Brant, F. Plentz, E. S. Alves, and M. A. Pimenta, "Determination of la and to phonon dispersion relations of graphene near the dirac point by double resonance raman scattering," *Phys. Rev. B*, vol. 76, p. 233407, Dec 2007.

[120] L. G. Cançado and L. Novotny, "Observing the angular distribution of raman scattered fields," *ACS nano*, vol. 10, no. 2, pp. 1722–1723, 2016.

[121] L. Novotny and N. Van Hulst, "Antennas for light," *Nature photonics*, vol. 5, no. 2, p. 83, 2011.

[122] L. Tang, S. E. Kocabas, S. Latif, A. K. Okyay, D.-S. Ly-Gagnon, K. C. Saraswat, and D. A. Miller, "Nanometre-scale germanium photodetector enhanced by a near-infrared dipole antenna," *Nature Photonics*, vol. 2, no. 4, p. 226, 2008.

[123] L. Cao, J.-S. Park, P. Fan, B. Clemens, and M. L. Brongersma, "Resonant germanium nanoantenna photodetectors," *Nano letters*, vol. 10, no. 4, pp. 1229–1233, 2010.

[124] E. Cubukcu, E. A. Kort, K. B. Crozier, and F. Capasso, "Plasmonic laser antenna," *Applied Physics Letters*, vol. 89, no. 9, p. 093120, 2006.

[125] S. Pillai, K. Catchpole, T. Trupke, and M. Green, "Surface plasmon enhanced silicon solar cells," *Journal of applied physics*, vol. 101, no. 9, p. 093105, 2007.

[126] E. Di Fabrizio, S. Schlücker, J. Wenger, R. Regmi, H. Rigneault, G. Calafiore, M. West, S. Cabrini, M. Fleischer, N. F. Van Hulst, *et al.*, "Roadmap on biosensing and photonics with advanced nano-optical methods," *Journal of Optics*, vol. 18, no. 6, p. 063003, 2016.

[127] R. Regmi, *Nanophotonic antennas for enhanced single-molecule fluorescence detection and nanospectroscopy in living cell membranes.* PhD thesis, Aix Marseille Université, 2017.

[128] R. Regmi, P. M. Winkler, V. Flauraud, K. J. Borgman, C. Manzo, J. Brugger, H. Rigneault, J. Wenger, and M. F. García-Parajo, "Planar optical nanoantennas resolve cholesterol-dependent nanoscale heterogeneities in the plasma membrane of living cells," *Nano letters*, vol. 17, no. 10, pp. 6295–6302, 2017.

[129] X. Shi, N. Coca-López, J. Janik, and A. Hartschuh, "Advances in tip-enhanced near-field raman microscopy using nanoantennas," *Chemical Reviews*, vol. 117, no. 7, pp. 4945–4960, 2017.

[130] A. Hartschuh, E. J. Sánchez, X. S. Xie, and L. Novotny, "High-resolution near-field raman microscopy of single-walled carbon nanotubes," *Phys. Rev. Lett.*, vol. 90, p. 095503, Mar 2003.

[131] A. Hartschuh, H. N. Pedrosa, L. Novotny, and T. D. Krauss, "Simultaneous fluorescence and raman scattering from single carbon nanotubes," *Science*, vol. 301, no. 5638, pp. 1354–1356, 2003.

[132] S. Lal, S. Link, and N. J. Halas, "Nano-optics from sensing to waveguiding," *Nature photonics*, vol. 1, no. 11, p. 641, 2007.

[133] P. J. Schuck, W. Bao, and N. J. Borys, "A polarizing situation: Taking an in-plane perspective for next-generation near-field studies," *Frontiers of Physics*, vol. 11, no. 2, p. 117804, 2016.

[134] L. Novotny, *Progress in Optics*, vol. 50. Amsterdam: Elsevier, 2007.

[135] T. Schmid, L. Opilik, C. Blum, and R. Zenobi, "Nanoscale chemical imaging using tip-enhanced raman spectroscopy: A critical review," *Angew. Chem. Int. Ed.*, vol. 52, no. 23, pp. 5940–5954, 2013.

[136] B. Pettinger, P. Schambach, C. J. Villagómez, and N. Scott, "Tip-enhanced raman spectroscopy: Near-fields acting on a few molecules," *Annu. Rev. Phys. Chem.*, vol. 63, no. 1, pp. 379–399, 2012.

[137] J. M. Atkin, S. Berweger, A. C. Jones, and M. B. Raschke, "Nano-optical imaging and spectroscopy of order, phases, and domains in complex solids," *Adv. Phys.*, vol. 61, pp. 745–842, 2012.

[138] N. Mauser, N. Hartmann, M. S. Hofmann, J. Janik, A. Hoögele, and A. Hartschuh, "Antenna-enhanced optoelectronic probing of carbon nanotubes," *Nano letters*, vol. 14, no. 7, pp. 3773–3778, 2014.

[139] M. D. Sonntag, E. A. Pozzi, N. Jiang, M. C. Hersam, and R. P. V. Duyne, "Recent advances in tip-enhanced raman spectroscopy," *J. Phys. Chem. Lett.*, vol. 5, no. 18, pp. 3125–3130, 2014.

[140] N. Kumar, S. Mignuzzi, W. Su, and D. Roy, "Tip-enhanced raman spectroscopy: Principles and applications," *EPJ. Technol. Instrum*, vol. 2, pp. 1–23, 2015.

[141] L. Langelüddecke, P. Singh, and V. Deckert, "Exploring the nanoscale: Fifteen years of tip-enhanced raman spectroscopy," *Appl. Spectrosc.*, vol. 69, no. 12, pp. 1357–1371, 2015.

[142] N. Jiang, D. Kurouski, E. A. Pozzi, N. Chiang, M. C. Hersam, and R. P. V. Duyne, "Tip-enhanced raman spectroscopy: from concepts to practical applications," *Chem. Phys. Lett.*, vol. 659, pp. 16–24, 2016.

[143] P. Bharadwaj, B. Deutsch, and L. Novotny, "Optical antennas," *Advances in Optics and Photonics*, vol. 1, no. 3, pp. 438–483, 2009.

[144] M. Agio and A. Alù, eds., *Optical Antennas*. Cambridge: Cambridge University Press, 2013.

[145] L. Novotny and N. van Hulst, "Antennas for light," *Nat. Photonics*, vol. 5, pp. 83–90, 2011.

[146] R. L. Olmon and M. B. Raschke, "Antenna-load interactions at optical frequencies: Impedance matching to quantum systems," *Nanotechnology*, vol. 23, no. 44, p. 444001, 2012.

[147] P. Anger, P. Bharadwaj, and L. Novotny, "Enhancement and quenching of single-molecule fluorescence," *Phys. Rev. Lett.*, vol. 96, p. 113002, 2006.

[148] K. B. Crozier, A. Sundaramurthy, G. S. Kino, and C. F. Quate, "Optical antennas: Resonators for local field enhancement," *J. Appl. Phys.*, vol. 94, no. 7, pp. 4632–4642, 2003.

[149] A. Kinkhabwala, Z. Yu, S. Fan, Y. Avlasevich, K. Müllen, and W. E. Moerner, "Large single-molecule fluorescence enhancements produced by a bowtie nanoantenna," *Nat. Photonics*, vol. 3, pp. 654–657, 2009.

[150] P. Chen, J. Liu, L. Wang, K. Jin, Y. Yin, and Z. Li, "Optimization and maximum potential of optical antennae in near-field enhancement," *Appl. Opt.*, vol. 54, no. 18, pp. 5822–5828, 2015.

[151] J. T. Krug, E. J. Sánchez, and X. S. Xie, "Design of near-field optical probes with optimal field enhancement by finite difference time domain electromagnetic simulation," *J. Chem. Phys.*, vol. 116, no. 24, pp. 10895–10901, 2002.

[152] L. Novotny, "Effective wavelength scaling for optical antennas," *Phys. Rev. Lett.*, vol. 98, p. 266802, 2007.

[153] L. Novotny, E. Sanches, and X. Xie, "Near-field optical imaging using metal tips illuminated by higher-order Hermite-Gaussian beams," *Ultramicroscopy*, vol. 71, pp. 21–29, 1998.

[154] A. L. Demming, F. Festy, and D. Richards, "Plasmon resonances on metal tips: Understanding tip-enhanced raman scattering," *J. Chem. Phys*, vol. 122, no. 18, p. 184716, 2005.

[155] N. Kazemi-Zanjani, S. Vedraine, and F. Lagugné-Labarthet, "Localized enhancement of electric field in tip-enhanced raman spectroscopy using radially and linearly polarized light," *Opt. Express*, vol. 21, pp. 25271–25276, Oct 2013.

[156] Z. Yang, J. Aizpurua, and H. Xu, "Electromagnetic field enhancement in ters configurations," *J. Raman Spectrosc.*, vol. 40, no. 10, pp. 1343–1348, 2009.

[157] I. Notingher, , and A. Elfick, "Effect of sample and substrate electric properties on the electric field enhancement at the apex of spm nanotips," *J. Phys. Chem. B*, vol. 109, no. 33, pp. 15699–15706, 2005.

[158] L. Aigouy, A. Lahrech, S. Grésillon, H. Cory, A. C. Boccara, and J. C. Rivoal, "Polarization effects in apertureless scanning near-field optical microscopy: an experimental study," *Opt. Lett.*, vol. 24, pp. 187–189, Feb 1999.

[159] N. Anderson, P. Anger, A. Hartschuh, and L. Novotny, "Sub-surface raman imaging with nanoscale resolution," *Nano Lett.*, vol. 6, pp. 744–749, 2006.

[160] W. Barnes, "Fluorescence near interfaces: the role of photonic mode density," *journal of modern optics*, vol. 45, no. 4, pp. 661–699, 1998.

[161] R. Chance, A. Prock, and R. Silbey, "Lifetime of an emitting molecule near a partially reflecting surface," *The Journal of Chemical Physics*, vol. 60, no. 7, pp. 2744–2748, 1974.

[162] J. N. Farahani, D. W. Pohl, H.-J. Eisler, and B. Hecht, "Single quantum dot coupled to a scanning optical antenna: A tunable superemitter," *Phys. Rev. Lett.*, vol. 95, p. 017402, June 2005.

[163] S. Kühn, U. Håkanson, L. Rogobete, and V. Sandoghdar, "Enhancement of single-molecule fluorescence using a gold nanoparticle as an optical nanoantenna," *Physical review letters*, vol. 97, no. 1, p. 017402, 2006.

[164] R. Eckel, V. Walhorn, C. Pelargus, J. Martini, J. Enderlein, T. Nann, D. Anselmetti, and R. Ros, "Fluorescence-emission control of single cdse nanocrystals using gold-modified afm tips," *Small*, vol. 3, no. 1, pp. 44–49, 2007.

[165] A. Bek, R. Jansen, M. Ringler, S. Mayilo, T. A. Klar, and J. Feldmann, "Fluorescence enhancement in hot spots of afm-designed gold nanoparticle sandwiches," *Nano Letters*, vol. 8, no. 2, pp. 485–490, 2008.

[166] E. Yoskovitz, I. Hadar, A. Sitt, I. Lieberman, and U. Banin, "Interplay of quenching and enhancement effects in aperture less near-field fluorescence imaging of single nanoparticles," *J. Phys. Chem. C*, vol. 115, no. 32, pp. 15834–15844, 2011.

[167] N. Anderson, A. Hartschuh, S. Cronin, and L. Novotny, "Nanoscale vibrational analysis of single-walled carbon nanotubes," *J. Am. Chem. Soc*, vol. 127, no. 8, pp. 2533–2537, 2005.

[168] J. Steidtner and B. Pettinger, "Tip-enhanced raman spectroscopy and microscopy on single dye molecules with 15 nm resolution," *Phys. Rev. Lett.*, vol. 100, p. 236101, Jun 2008.

[169] K. L. A. Chan and S. G. Kazarian, "Finding a needle in a chemical haystack: Tip-enhanced raman scattering for studying carbon nanotubes mixtures," *Nanotechnology*, vol. 21, no. 44, p. 445704, 2010.

[170] B. Pettinger, K. F. Domke, D. Zhang, R. Schuster, and G. Ertl, "Direct monitoring of plasmon resonances in a tip-surface gap of varying width," *Phys. Rev. B*, vol. 76, p. 113409, Sep 2007.

[171] T. Deckert-Gaudig, E. Bailo, and V. Deckert, "Tip-enhanced raman scattering (ters) of oxidised glutathione on an ultraflat gold nanoplate," *Phys. Chem. Chem. Phys.*, vol. 11, pp. 7360–7362, 2009.

[172] J. Stadler, B. Oswald, T. Schmid, and R. Zenobi, "Characterizing unusual metal substrates for gap-mode tip-enhanced raman spectroscopy," *J. Raman Spectrosc.*, vol. 44, no. 2, pp. 227–233, 2013.

[173] S. Zhang, H. Wei, K. Bao, U. Håkanson, N. J. Halas, P. Nordlander, and H. Xu, "Chiral surface plasmon polaritons on metallic nanowires," *Phys. Rev. Lett.*, vol. 107, p. 096801, Aug 2011.

[174] S. F. Becker, M. Esmann, K. Yoo, P. Gross, R. Vogelgesang, N. Park, and C. Lienau, "Gap-plasmon-enhanced nanofocusing near-field microscopy," *ACS Photonics*, vol. 3, no. 2, pp. 223–232, 2016.

[175] P. Nordlander and E. Prodan, "Plasmon hybridization in nanoparticles near metallic surfaces," *Nano Lett.*, vol. 4, no. 11, pp. 2209–2213, 2004.

[176] J. Steidtner and B. Pettinger, "Tip-enhanced raman spectroscopy and microscopy on single dye molecules with 15 nm resolution," *Phys. Rev. Lett.*, vol. 100, p. 236101, 2008.

[177] H. Xu, J. Aizpurua, M. Käll, and P. Apell, "Electromagnetic contributions to single-molecule sensitivity in surface-enhanced raman scattering," *Phys. Rev. E*, vol. 62, p. 4318, 2000.

[178] M. Futamata, Y. Maruyama, and M. Ishikawa, "Local electric field and scattering cross section of ag nanoparticles under surface plasmon resonance by finite difference time domain method," *J. Phys. Chem. B*, vol. 107, no. 31, pp. 7607–7617, 2003.

[179] E. Hao and G. C. Schatz, "Electromagnetic fields around silver nanoparticles and dimers," *J. Chem. Phys.*, vol. 120, no. 1, pp. 357–366, 2004.

[180] R. W. Rendell and D. J. Scalapino, "Surface plasmons confined by microstructures on tunnel junctions," *Phys. Rev. B*, vol. 24, p. 3276, Sep 1981.

[181] K. J. Savage, M. M. Hawkeye, R. Esteban, A. G. Borisov, J. Aizpurua, and J. J. Baumberg, "Revealing the quantum regime in tunnelling plasmonics," *Nature*, vol. 491, pp. 574–577, Nov. 2012.

[182] W. Zhu, R. Esteban, A. G. Borisov, J. J. Baumberg, P. Nordlander, H. J. Lezec, J. Aizpurua, and K. B. Crozier, "Quantum mechanical effects in plasmonic structures with subnanometre gaps," *Nature communications*, vol. 7, p. 11495, 2016.

[183] M. Brack, "The physics of simple metal clusters: self-consistent jellium model and semiclassical approach," *Rev. Mod. Phys.*, vol. 65, pp. 677–732, 1993.

[184] N. W. Ascroft and N. Mermin, *Solid State Physics*. New York: Holt, Rinehart and Winston, 1976.

[185] R. Fuchs and F. Claro, "Multipolar response of small metallic spheres: Nonlocal theory," *Phys. Rev. B*, vol. 35, pp. 3722–3727, Mar 1987.

[186] A. Liebsch and W. L. Schaich, "Influence of a polarizable medium on the nonlocal optical response of a metal surface," *Phys. Rev. B*, vol. 52, pp. 14219–14234, Nov 1995.

[187] F. J. García de Abajo, "Nonlocal effects in the plasmons of strongly interacting nanoparticles, dimers, and waveguides," *J. Phys. Chem. C*, vol. 112, no. 46, pp. 17983–17987, 2008.

[188] J. Zuloaga, E. Prodan, and P. Nordlander, "Quantum Plasmonics: Optical Properties and Tunability of Metallic Nanorods," *ACS Nano*, vol. 4, pp. 5269–5276, 2010.

[189] R. Esteban, A. G. Borisov, P. Nordlander, and J. Aizpurua, " Bridging Quantum and Classical Plasmonics with a Quantum-Corrected Model," *Nat. Commun.*, vol. 3, p. 825, 2012.

[190] W. Zhu and K. B. Crozier, "Quantum mechanical limit to plasmonic enhancement as observed by surface-enhanced raman scattering," *Nat. Commun.*, vol. 5, p. 5228, 2014.

[191] M. Barbry, P. Koval, F. Marchesin, R. Esteban, A. G. Borisov, J. Aizpurua, and D. Sánchez-Portal, "Atomistic Near-Field Nanoplasmonics: Reaching Atomic-Scale Resolution in Nanooptics," *ACS Nano*, vol. 15, pp. 3410–3419, 2015.

[192] S. Trautmann, J. Aizpurua, I. Götz, A. Undisz, J. Dellith, H. Schneidewind, M. Rettenmayr, and V. Deckert, "A classical description of subnanometer resolution by atomic features in metallic structures," *Nanoscale*, vol. 9, pp. 391–401, 2017.

[193] F. Benz, M. K. Schmidt, A. Dreismann, R. Chikkaraddy, Y. Zhang, A. Demetriadou, C. Carnegie, H. Ohadi, B. de Nijs, R. Esteban, A. J., and J. J. Baumberg, "Single-molecule optomechanics in picocavities," *Science*, vol. 354, pp. 726–729, 2016.

[194] N. Mauser, *Antenna-enhanced optoelectronic probing of carbon nanotube devices*. PhD thesis, lmu, 2014.

[195] S. Berweger and M. B. Raschke, "Signal Limitations in Tip-Enhanced Raman Scattering: the Challenge to Become a Routine Analytical Technique," *Anal. Bioanal. Chem.*, vol. 396, pp. 115–123, 2010.

[196] P. Roelli, C. Galland, N. Piro, and T. J. Kippenberg, "Molecular cavity optomechanics as a theory of plasmon-enhanced raman scattering," *Nat. Nanotechnol.*, vol. 11, pp. 164–169, 2015.

[197] M. K. Schmidt, R. Esteban, A. González-Tudela, G. Giedke, and J. Aizpurua, "Quantum mechanical description of raman scattering from molecules in plasmonic cavities," *ACS Nano*, vol. 10, pp. 6291–6298, 2016.

[198] E. J. Ayars, H. D. Hallen, and C. L. Jahncke, "Electric field gradient effects in raman spectroscopy," *Phys. Rev. Lett.*, vol. 85, p. 4180, 2000.

[199] L. Meng, Z. Yang, J. Chen, and M. Sun, "Effect of Electric Field Gradient on Sub-nanometer Spatial Resolution of Tip-enhanced Raman Spectroscopy," *Sci. Rep.*, vol. 5, p. 9240, 2015.

[200] S. Duan, G. Tian, Y. Ji, J. Shao, Z. Dong, and Y. Luo, "Theoretical modeling of plasmon-enhanced raman images of a single molecule with subnanometer resolution," *J. Am. Chem. Soc*, vol. 137, no. 30, pp. 9515–9518, 2015.

[201] C. Zhang, B.-Q. Chen, and Z.-Y. Li, "Optical origin of subnanometer resolution in tip-enhanced raman mapping," *The Journal of Physical Chemistry C*, vol. 119, no. 21, pp. 11858–11871, 2015.

[202] C. Zhang, B.-Q. Chen, and Z. Y. Li, "Influence of tip geometry on the spatial resolution of tip enhanced raman mapping," *Chin. Phys. B*, vol. 25, p. 095203, 2016.

[203] A. Hartschuh, H. Qian, A. J. Meixner, N. Anderson, and L. Novotny, "Nanoscale optical imaging of excitons in single-walled carbon nanotubes," *Nano letters*, vol. 5, no. 11, pp. 2310–2313, 2005.

[204] K. Aslan, I. Gryczynski, J. Malicka, E. Matveeva, J. R. Lakowicz, and C. D. Geddes, "Metal-enhanced fluorescence: an emerging tool in biotechnology," *Current opinion in biotechnology*, vol. 16, no. 1, pp. 55–62, 2005.

[205] N. Rauhut, M. Engel, M. Steiner, R. Krupke, P. Avouris, and A. Hartschuh, "Antenna-enhanced photocurrent microscopy on single-walled carbon nanotubes at 30 nm resolution," *ACS nano*, vol. 6, no. 7, pp. 6416–6421, 2012.

[206] N. Coca-López, *Master Thesis: Towards on-chip quantum optics: Studies on InGaAs quantum dot based plasmonic hybrid systems*. Technische Universiät München, 2013.

[207] H. Raether, *Surface plasmons on smooth and rough surfaces and on gratings*. Springer-Verlag Berlin An, 2013.

[208] A. D. Rakić, A. B. Djurišić, J. M. Elazar, and M. L. Majewski, "Optical properties of metallic films for vertical-cavity optoelectronic devices," *Applied optics*, vol. 37, no. 22, pp. 5271–5283, 1998.

[209] G. N. Bracher, *Lithographically Defined Plasmonic Waveguides and Their Coupling to Proximal Quantum Dots*. Verein zur Förderung des Walter Schottky Instituts der Technischen Universität München eV, 2016.

[210] E. Arakawa, M. Williams, R. Hamm, and R. Ritchie, "Effect of damping on surface plasmon dispersion," *Physical Review Letters*, vol. 31, no. 18, p. 1127, 1973.

[211] W. L. Barnes, A. Dereux, and T. W. Ebbesen, "Surface plasmon subwavelength optics," *nature*, vol. 424, no. 6950, p. 824, 2003.

[212] A. Otto, "Excitation of nonradiative surface plasma waves in silver by the method of frustrated total reflection," *Zeitschrift für Physik A Hadrons and nuclei*, vol. 216, no. 4, pp. 398–410, 1968.

[213] J. Burke, G. Stegeman, and T. Tamir, "Surface-polariton-like waves guided by thin, lossy metal films," *Physical Review B*, vol. 33, no. 8, p. 5186, 1986.

[214] E. Kretschmann, "Die bestimmung optischer konstanten von metallen durch anregung von oberflächenplasmaschwingungen," *Zeitschrift für Physik A Hadrons and nuclei*, vol. 241, no. 4, pp. 313–324, 1971.

[215] K. Welford, J. Sambles, and M. Clark, "Guided modes and surface plasmon-polaritons observed with a nematic liquid crystal using attenuated total reflection," *Liquid Crystals*, vol. 2, no. 1, pp. 91–105, 1987.

[216] H. Kano, S. Mizuguchi, and S. Kawata, "Excitation of surface-plasmon polaritons by a focused laser beam," *JOSA B*, vol. 15, no. 4, pp. 1381–1386, 1998.

[217] A. Bouhelier and G. Wiederrecht, "Excitation of broadband surface plasmon polaritons: Plasmonic continuum spectroscopy," *Physical Review B*, vol. 71, no. 19, p. 195406, 2005.

[218] A. Bouhelier, F. Ignatovich, A. Bruyant, C. Huang, G. C. Des Francs, J.-C. Weeber, A. Dereux, G. P. Wiederrecht, and L. Novotny, "Surface plasmon interference excited by tightly focused laser beams," *Optics letters*, vol. 32, no. 17, pp. 2535–2537, 2007.

[219] F. Stefani, K. Vasilev, N. Bocchio, N. Stoyanova, and M. Kreiter, "Surface-plasmon-mediated single-molecule fluorescence through a thin metallic film," *Physical review letters*, vol. 94, no. 2, p. 023005, 2005.

[220] R. W. Wood, "Xlii. on a remarkable case of uneven distribution of light in a diffraction grating spectrum," *The London, Edinburgh, and Dublin Philosophical Magazine and Journal of Science*, vol. 4, no. 21, pp. 396–402, 1902.

[221] G. Bracher, K. Schraml, C. Jakubeit, M. Kaniber, and J. Finley, "Direct measurement of plasmon propagation lengths on lithographically defined metallic waveguides on gaas," *Journal of Applied Physics*, vol. 110, no. 12, p. 123106, 2011.

[222] C. Ropers, C. Neacsu, T. Elsaesser, M. Albrecht, M. Raschke, and C. Lienau, "Grating-coupling of surface plasmons onto metallic tips: a nanoconfined light source," *Nano letters*, vol. 7, no. 9, pp. 2784–2788, 2007.

[223] S. Berweger, J. M. Atkin, R. L. Olmon, and M. B. Raschke, "Adiabatic tip-plasmon focusing for nano-raman spectroscopy," *The Journal of Physical Chemistry Letters*, vol. 1, no. 24, pp. 3427–3432, 2010.

[224] H. J. Lezec, A. Degiron, E. Devaux, R. Linke, L. Martin-Moreno, F. Garcia-Vidal, and T. Ebbesen, "Beaming light from a subwavelength aperture," *Science*, vol. 297, no. 5582, pp. 820–822, 2002.

[225] K. L. Kelly, E. Coronado, L. L. Zhao, and G. C. Schatz, "The optical properties of metal nanoparticles: the influence of size, shape, and dielectric environment," 2003.

[226] C. F. Bohren and D. R. Huffman, *Absorption and scattering of light by small particles*. John Wiley & Sons, 2008.

[227] U. Kreibig and M. Vollmer, *Optical properties of metal clusters*, vol. 25. Springer Science & Business Media, 2013.

[228] J. Luis-Hita, M. I. Marques, R. Delgado-Buscalioni, N. de Sousa, L. S. Froufe-Perez, F. Scheffold, and J. J. Saenz, "Light induced" mock gravity" at the nanoscale," *arXiv preprint arXiv:1802.05648*, 2018.

[229] N. Hartmann, D. Piatkowski, R. Ciesielski, S. Mackowski, and A. Hartschuh, "Radiation channels close to a plasmonic nanowire visualized by back focal plane imaging," *ACS Nano*, vol. 7, no. 11, pp. 10257–10262, 2013.

[230] T. Shegai, V. D. Miljkovic, K. Bao, H. Xu, P. Nordlander, P. Johansson, and M. Kall, "Unidirectional broadband light emission from supported plasmonic nanowires," *Nano letters*, vol. 11, no. 2, pp. 706–711, 2011.

[231] Z. Han and S. I. Bozhevolnyi, "Radiation guiding with surface plasmon polaritons," *Reports on Progress in Physics*, vol. 76, no. 1, p. 016402, 2012.

[232] X. Guo, Y. Ma, Y. Wang, and L. Tong, "Nanowire plasmonic waveguides, circuits and devices," *Laser & Photonics Reviews*, vol. 7, no. 6, pp. 855–881, 2013.

[233] H. Wei and H. Xu, "Nanowire-based plasmonic waveguides and devices for integrated nanophotonic circuits," *Nanophotonics*, vol. 1, no. 2, pp. 155–169, 2012.

[234] P. Deng, W. Hong, and X. Hong-Xing, "Metallic nanowires for subwavelength waveguiding and nanophotonic devices," *Chinese Physics B*, vol. 22, no. 9, p. 097305, 2013.

[235] T. Laroche, A. Vial, and M. Roussey, "Crystalline structure's influence on the near-field optical properties of single plasmonic nanowires," *Applied Physics Letters*, vol. 91, no. 12, p. 123101, 2007.

[236] P. Kusar, C. Gruber, A. Hohenau, and J. R. Krenn, "Measurement and reduction of damping in plasmonic nanowires," *Nano letters*, vol. 12, no. 2, pp. 661–665, 2012.

[237] D. Singh, A. Dasgupta, V. Aswathy, R. P. Tripathi, and G. V. P. Kumar, "Directional out-coupling of light from a plasmonic nanowire-nanoparticle junction," *Opt. lett.*, vol. 40, no. 6, pp. 1006–1009, 2015.

[238] S. Dai, Q. Li, G. Liu, H. Yang, Y. Yang, D. Zhao, W. Wang, and M. Qiu, "Laser-induced single point nanowelding of silver nanowires," *Applied Physics Letters*, vol. 108, no. 12, p. 121103, 2016.

[239] Q. Li, G. Liu, H. Yang, W. Wang, S. Luo, S. Dai, and M. Qiu, "Optically controlled local nanosoldering of metal nanowires," *Applied Physics Letters*, vol. 108, no. 19, p. 193101, 2016.

[240] L. Zhou, J. Lu, H. Yang, S. Luo, W. Wang, J. Lv, M. Qiu, and Q. Li, "Optically controllable nanobreaking of metallic nanowires," *Applied Physics Letters*, vol. 110, no. 8, p. 081101, 2017.

[241] M. Song, A. Thete, J. Berthelot, Q. Fu, D. Zhang, G. C. des Francs, E. Dujardin, and A. Bouhelier, "Electron-induced limitation of surface plasmon propagation in silver nanowires," *Nanotechnology*, vol. 24, no. 9, p. 095201, 2013.

[242] L. Novotny and C. Hafner, "Light propagation in a cylindrical waveguide with a complex, metallic, dielectric function," *Physical review E*, vol. 50, no. 5, p. 4094, 1994.

[243] H. Yang, M. Qiu, and Q. Li, "Identification and control of multiple leaky plasmon modes in silver nanowires," *Laser & Photonics Reviews*, vol. 10, no. 2, pp. 278–286, 2016.

[244] Q. Li and M. Qiu, "Plasmonic wave propagation in silver nanowires: guiding modes or not?," *Optics express*, vol. 21, no. 7, pp. 8587–8595, 2013.

[245] D. E. Chang, A. S. Sørensen, P. Hemmer, and M. Lukin, "Strong coupling of single emitters to surface plasmons," *Physical Review B*, vol. 76, no. 3, p. 035420, 2007.

[246] S. Zhang, H. Wei, K. Bao, U. Håkanson, N. J. Halas, P. Nordlander, and H. Xu, "Chiral surface plasmon polaritons on metallic nanowires," *Phys. Rev. Lett.*, vol. 107, no. 9, p. 096801, 2011.

[247] G. Bracher, K. Schraml, M. Blauth, J. Wierzbowski, N. Coca López, M. Bichler, K. Müller, J. J. Finley, and M. Kaniber, "Imaging surface plasmon polaritons using proximal self-assembled ingaas quantum dots," *J. Appl. Phys.*, vol. 116, no. 3, p. 033101, 2014.

[248] J.-C. Weeber, A. Dereux, C. Girard, J. R. Krenn, and J.-P. Goudonnet, "Plasmon polaritons of metallic nanowires for controlling submicron propagation of light," *Physical Review B*, vol. 60, no. 12, p. 9061, 1999.

[249] R. M. Dickson and L. A. Lyon, "Unidirectional plasmon propagation in metallic nanowires," *J. Phys. Chem. B*, vol. 104, no. 26, pp. 6095–6098, 2000.

[250] M. Song, J. Dellinger, O. Demichel, M. Buret, G. C. Des Francs, D. Zhang, E. Dujardin, and A. Bouhelier, "Selective excitation of surface plasmon modes propagating in ag nanowires," *Opt. Express*, vol. 25, no. 8, pp. 9138–9149, 2017.

[251] R. A. Flynn, K. Bussmann, B. Simpkins, I. Vurgaftman, C. S. Kim, and J. P. Long, "Propagation length of surface plasmon polaritons determined by emission from introduced surface discontinuities," *Journal of Applied Physics*, vol. 107, no. 1, p. 013109, 2010.

[252] Z. Li, K. Bao, Y. Fang, Y. Huang, P. Nordlander, and H. Xu, "Correlation between incident and emission polarization in nanowire surface plasmon waveguides," *Nano letters*, vol. 10, no. 5, pp. 1831–1835, 2010.

[253] G.-P. Guo, R. Yang, X.-F. Ren, L.-L. Wang, H.-Y. Shi, B. Hu, S.-H. Yu, and G.-C. Guo, "Excitation of surface plasmons in a single silver nanowire using higher-order-mode light," *Physica E: Low-dimensional Systems and Nanostructures*, vol. 42, no. 5, pp. 1751–1754, 2010.

[254] N. Liu, Z. Li, and H. Xu, "Polarization-dependent study on propagating surface plasmons in silver nanowires launched by a near-field scanning optical fiber tip," *Small*, vol. 8, no. 17, pp. 2641–2646, 2012.

[255] P. Venugopalan, Q. Zhang, X. Li, and M. Gu, "Polarization-sensitive characterization of the propagating plasmonic modes in silver nanowire waveguide on a glass substrate with a scanning near-field optical microscope," *Optics Express*, vol. 21, no. 13, pp. 15247–15252, 2013.

[256] A. Normatov, B. Spektor, Y. Leviatan, and J. Shamir, "Absorption enhancement by matching the cross-section of plasmonic nanowires to the field structure of tightly focused beams," *Optics Express*, vol. 19, no. 9, pp. 8506–8513, 2011.

[257] S. Viarbitskaya, O. Demichel, B. Cluzel, G. C. des Francs, and A. Bouhelier, "Delocalization of nonlinear optical responses in plasmonic nanoantennas," *Physical review letters*, vol. 115, no. 19, p. 197401, 2015.

[258] K. Hassan, A. Bouhelier, T. Bernardin, G. Colas-des Francs, J.-C. Weeber, A. Dereux, and R. Espiau de Lamaestre, "Momentum-space spectroscopy for advanced analysis of dielectric-loaded surface plasmon polariton coupled and bent waveguides," *Phys. Rev. B*, vol. 87, p. 195428, May 2013.

[259] N. Coca Lopez, N. Hartmann, T. Mancabelli, J. Kraus, S. Guenther, A. Comin, and A. Hartschuh, "Remote excitation and detection of surface-enhanced raman scattering from graphene," *Nanoscale*, pp. –, 2018.

[260] N. Liu and T. Liedl, "Dna-assembled advanced plasmonic architectures," *Chemical reviews*, 2018.

[261] M. Pilo-Pais, A. Watson, S. Demers, T. LaBean, and G. Finkelstein, "Surface-enhanced raman scattering plasmonic enhancement using dna origami-based complex metallic nanostructures," *Nano letters*, vol. 14, no. 4, pp. 2099–2104, 2014.

[262] E.-M. Roller, C. Argyropoulos, A. Högele, T. Liedl, and M. Pilo-Pais, "Plasmon–exciton coupling using dna templates," *Nano letters*, vol. 16, no. 9, pp. 5962–5966, 2016.

[263] F. Koppens, T. Mueller, P. Avouris, A. Ferrari, M. Vitiello, and M. Polini, "Photodetectors based on graphene, other two-dimensional materials and hybrid systems," *Nature nanotechnology*, vol. 9, no. 10, pp. 780–793, 2014.

[264] J. Park, Y. Ahn, and C. Ruiz-Vargas, "Imaging of photocurrent generation and collection in single-layer graphene," *Nano letters*, vol. 9, no. 5, pp. 1742–1746, 2009.

[265] E. J. Lee, K. Balasubramanian, R. T. Weitz, M. Burghard, and K. Kern, "Contact and edge effects in graphene devices," *Nature nanotechnology*, vol. 3, no. 8, p. 486, 2008.

[266] F. Xia, T. Mueller, R. Golizadeh-Mojarad, M. Freitag, Y.-m. Lin, J. Tsang, V. Perebeinos, and P. Avouris, "Photocurrent imaging and efficient photon detection in a graphene transistor," *Nano letters*, vol. 9, no. 3, pp. 1039–1044, 2009.

[267] E. C. Peters, E. J. Lee, M. Burghard, and K. Kern, "Gate dependent photocurrents at a graphene pn junction," *Applied Physics Letters*, vol. 97, no. 19, p. 193102, 2010.

[268] G. Rao, M. Freitag, H.-Y. Chiu, R. S. Sundaram, and P. Avouris, "Raman and photocurrent imaging of electrical stress-induced p–n junctions in graphene," *ACS nano*, vol. 5, no. 7, pp. 5848–5854, 2011.

[269] T. Mueller, F. Xia, M. Freitag, J. Tsang, P. Avouris, *et al.*, "Role of contacts in graphene transistors: A scanning photocurrent study," *Physical Review B*, vol. 79, no. 24, p. 245430, 2009.

[270] M. Freitag, T. Low, F. Xia, and P. Avouris, "Photoconductivity of biased graphene," *Nature Photonics*, vol. 7, no. 1, p. 53, 2013.

[271] D. B. Farmer, R. Golizadeh-Mojarad, V. Perebeinos, Y.-M. Lin, G. S. Tulevski, J. C. Tsang, and P. Avouris, "Chemical doping and electron- hole conduction asymmetry in graphene devices," *Nano letters*, vol. 9, no. 1, pp. 388–392, 2008.

[272] M. C. Lemme, F. H. Koppens, A. L. Falk, M. S. Rudner, H. Park, L. S. Levitov, and C. M. Marcus, "Gate-activated photoresponse in a graphene p–n junction," *Nano letters*, vol. 11, no. 10, pp. 4134–4137, 2011.

[273] N. M. Gabor, J. C. Song, Q. Ma, N. L. Nair, T. Taychatanapat, K. Watanabe, T. Taniguchi, L. S. Levitov, and P. Jarillo-Herrero, "Hot carrier–assisted intrinsic photoresponse in graphene," *Science*, vol. 334, no. 6056, pp. 648–652, 2011.

[274] X. Xu, N. M. Gabor, J. S. Alden, A. M. van der Zande, and P. L. McEuen, "Photothermoelectric effect at a graphene interface junction," *Nano letters*, vol. 10, no. 2, pp. 562–566, 2009.

[275] B. C. St-Antoine, D. Ménard, and R. Martel, "Position sensitive photothermoelectric effect in suspended single-walled carbon nanotube films," *Nano letters*, vol. 9, no. 10, pp. 3503–3508, 2009.

[276] U. Sassi, R. Parret, S. Nanot, M. Bruna, S. Borini, D. De Fazio, Z. Zhao, E. Lidorikis, F. Koppens, A. C. Ferrari, *et al.*, "Graphene-based mid-infrared room-temperature pyroelectric bolometers with ultrahigh temperature coefficient of resistance," *Nature communications*, vol. 8, p. 14311, 2017.

[277] A. Tomadin and M. Polini, "Theory of the plasma-wave photoresponse of a gated graphene sheet," *Physical Review B*, vol. 88, no. 20, p. 205426, 2013.

[278] L. Vicarelli, M. Vitiello, D. Coquillat, A. Lombardo, A. Ferrari, W. Knap, M. Polini, V. Pellegrini, and A. Tredicucci, "Graphene field-effect transistors as room-temperature terahertz detectors," *Nature materials*, vol. 11, no. 10, p. 865, 2012.

[279] D. Spirito, D. Coquillat, S. L. De Bonis, A. Lombardo, M. Bruna, A. C. Ferrari, V. Pellegrini, A. Tredicucci, W. Knap, and M. S. Vitiello, "High performance bilayer-graphene terahertz detectors," *Applied Physics Letters*, vol. 104, no. 6, p. 061111, 2014.

[280] M. Freitag, J. C. Tsang, A. Bol, D. Yuan, J. Liu, and P. Avouris, "Imaging of the schottky barriers and charge depletion in carbon nanotube transistors," *Nano letters*, vol. 7, no. 7, pp. 2037–2042, 2007.

[281] K. Balasubramanian, Y. Fan, M. Burghard, K. Kern, M. Friedrich, U. Wannek, and A. Mews, "Photoelectronic transport imaging of individual semiconducting carbon nanotubes," *Applied Physics Letters*, vol. 84, no. 13, pp. 2400–2402, 2004.

[282] E. J. Lee, K. Balasubramanian, J. Dorfmüller, R. Vogelgesang, N. Fu, A. Mews, M. Burghard, and K. Kern, "Electronic-band-structure mapping of nanotube transistors by scanning photocurrent microscopy," *Small*, vol. 3, no. 12, pp. 2038–2042, 2007.

[283] Y. Ahn, J. Dunning, and J. Park, "Scanning photocurrent imaging and electronic band studies in silicon nanowire field effect transistors," *Nano Letters*, vol. 5, no. 7, pp. 1367–1370, 2005.

[284] Y. Ahn, A. Tsen, B. Kim, Y. W. Park, and J. Park, "Photocurrent imaging of p-n junctions in ambipolar carbon nanotube transistors," *Nano letters*, vol. 7, no. 11, pp. 3320–3323, 2007.

[285] S. Drieschner, A. Guimerà, R. G. Cortadella, D. Viana, E. Makrygiannis, B. M. Blaschke, J. Vieten, and J. A. Garrido, "Frequency response of electrolyte-gated graphene electrodes and transistors," *Journal of Physics D: Applied Physics*, vol. 50, no. 9, p. 095304, 2017.

[286] Z. Chen, J. Appenzeller, J. Knoch, Y.-m. Lin, and P. Avouris, "The role of metal-nanotube contact in the performance of carbon nanotube field-effect transistors," *Nano letters*, vol. 5, no. 7, pp. 1497–1502, 2005.

[287] A. W. Cummings and F. Léonard, "Enhanced performance of short-channel carbon nanotube field-effect transistors due to gate-modulated electrical contacts," *ACS nano*, vol. 6, no. 5, pp. 4494–4499, 2012.

[288] P. Avouris, Z. Chen, and V. Perebeinos, "Carbon-based electronics," *Nature nanotechnology*, vol. 2, no. 10, p. 605, 2007.

[289] A. Woessner, P. Alonso-González, M. B. Lundeberg, Y. Gao, J. E. Barrios-Vargas, G. Navickaite, Q. Ma, D. Janner, K. Watanabe, A. W. Cummings, *et al.*, "Near-field photocurrent nanoscopy on bare and encapsulated graphene," *Nature communications*, vol. 7, p. 10783, 2016.

[290] C. Georgi, *Exciton Mobility and Localized Defects in Single Carbon Nanotubes Studied with Tip-Enhanced Near-Field Optical Microscopy.* PhD thesis, lmu, 2011.

[291] H. Qian, *Tip-enhanced Near-Field Optical Spectroscopy on Single-Walled Carbon Nanotubes.* PhD thesis, lmu, 2008.

[292] L. Novotny, R. X. Bian, and X. S. Xie, "Theory of nanometric optical tweezers," *Physical Review Letters*, vol. 79, no. 4, p. 645, 1997.

[293] X. Shi, *Tip-enhanced near-field optical microscopy of single-walled carbon nanotube/polymer conjugates and improvements of the image contrast.* PhD thesis, lmu, 2017.

[294] R. Dorn, S. Quabis, and G. Leuchs, "Sharper focus for a radially polarized light beam," *Phys. Rev. Lett.*, vol. 91, p. 233904, 2003.

[295] G. Binnig, H. Rohrer, C. Gerber, and E. Weibel, "Surface studies by scanning tunneling microscopy," *Physical review letters*, vol. 49, no. 1, p. 57, 1982.

[296] G. Binnig, C. F. Quate, and C. Gerber, "Atomic force microscope," *Phys. Rev. Lett.*, vol. 56, pp. 930–933, Mar 1986.

[297] J. Janik, *Implementation and characterization of a new low temperature tip-enhanced near-field optical microscope.* PhD thesis, lmu, 2017.

[298] T. Mancabelli, *Raman measurements on plasmon-phonon coupled systems.* PhD thesis, lmu, 2016.

[299] C. Xie, C. Mu, J. R. Cox, and J. M. Gerton, "Tip-enhanced fluorescence microscopy of high-density samples," *Applied physics letters*, vol. 89, no. 14, p. 143117, 2006.

[300] P. G. Gucciardi, G. Bachelier, and M. Allegrini, "Far-field background suppression in tip-modulated apertureless near-field optical microscopy," *Journal of applied physics*, vol. 99, no. 12, p. 124309, 2006.

[301] B. D. Mangum, C. Mu, and J. M. Gerton, "Resolving single fluorophores within dense ensembles: contrast limits of tip-enhanced fluorescence microscopy," *Optics Express*, vol. 16, no. 9, pp. 6183–6193, 2008.

[302] J. M. Gerton, L. A. Wade, G. A. Lessard, Z. Ma, and S. R. Quake, "Tip-enhanced fluorescence microscopy at 10 nanometer resolution," *Physical Review Letters*, vol. 93, no. 18, p. 180801, 2004.

[303] T.-a. Yano, T. Ichimura, A. Taguchi, N. Hayazawa, P. Verma, Y. Inouye, and S. Kawata, "Confinement of enhanced field investigated by tip-sample gap regulation in tapping-mode tip-enhanced raman microscopy," *Applied Physics Letters*, vol. 91, no. 12, p. 121101, 2007.

[304] B. D. Mangum, E. Shafran, C. Mu, and J. M. Gerton, "Three-dimensional mapping of near-field interactions via single-photon tomography," *Nano letters*, vol. 9, no. 10, pp. 3440–3446, 2009.

[305] C. Höppener, R. Beams, and L. Novotny, "Background suppression in near-field optical imaging," *Nano letters*, vol. 9, no. 2, pp. 903–908, 2009.

[306] Z. Yang, J. Aizpurua, and H. Xu, "Electromagnetic field enhancement in ters configurations," *J. Raman Spectrosc.*, vol. 40, no. 10, pp. 1343–1348, 2009.

[307] R. Ritchie, "Plasma losses by fast electrons in thin films," *Phys. Rev.*, vol. 106, no. 5, p. 874, 1957.

[308] H. Wei and H. Xu, "Hot spots in different metal nanostructures for plasmon-enhanced raman spectroscopy," *Nanoscale*, vol. 5, no. 22, pp. 10794–10805, 2013.

[309] G. V. P. Kumar, "Plasmonic nano-architectures for surface enhanced raman scattering: a review," *J. Nanophotonics*, vol. 6, pp. 6 – 6 – 20, 2012.

[310] A. C. Ferrari and D. M. Basko, "Raman spectroscopy as a versatile tool for studying the properties of graphene," *Nat. nanotechnol.*, vol. 8, no. 4, pp. 235–246, 2013.

[311] J. Schwan, S. Ulrich, V. Batori, H. Ehrhardt, and S. Silva, "Raman spectroscopy on amorphous carbon films," *J. Appl. Phys.*, vol. 80, no. 1, pp. 440–447, 1996.

[312] J. Kraus, M. Böbel, and S. Günther, "Supressing graphene nucleation during cvd on polycrystalline cu by controlling the carbon content of the support foils," *Carbon*, vol. 96, pp. 153–165, 2017.

[313] Y. Wang, Y. Zheng, X. Xu, E. Dubuisson, Q. Bao, J. Lu, and K. P. Loh, "Electrochemical delamination of cvd-grown graphene film: Toward the recyclable use of copper catalyst," *ACS Nano*, vol. 5, pp. 9927–9933, 2011.

[314] F. Bonaccorso, Z. Sun, T. Hasan, and A. Ferrari, "Graphene photonics and optoelectronics," *Nature photonics*, vol. 4, no. 9, p. 611, 2010.

[315] F. Bonaccorso, A. Lombardo, T. Hasan, Z. Sun, L. Colombo, and A. C. Ferrari, "Production and processing of graphene and 2d crystals," *Materials today*, vol. 15, no. 12, pp. 564–589, 2012.

Acronyms

AC	alternating current
AFM	atomic force microscopy
Ag	silver
APD	avalanche photodiode
Au	gold
ATR	attenuated total reflection
BFP	back focal plane
CCD	chage-coupled device
CTPs	charge transfer plasmons
CVD	chemical vapour deposition
DC	direct current
DoP	degree of polarization
EL	electroluminescence
HeNe	Helium Neon
iTO	in-plane transverse optical
LSP	localized surface plasmon
LSPR	localized surface plasmon resonance
NA	numerical aperture
NWs	nanowires
PC	photocurrent
PL	photoluminescence
PVP	Polyvinylpyrrolidone
RC	resistor capacitor
SERS	surface-enhanced Raman scattering
SNOM	scanning near field optical microscopy
SPCM	scanning photocurrent microscopy
SPs	surface plasmons
SPPs	surface plasmon polaritons
STM	scanning tunneling microscopy
SWCNT	single walled carbon nanotube
TDDFT	time-dependent density functional theory
TENOM	tip-enhanced near-field microscopy
TERS	tip-enhanced Raman scattering

List of Publications

- N. Coca-López, N. F. Hartmann, T. Mancabelli, J. Krauss, S. Günther, A. Comin, and A. Hartschuh, "Remote excitation and detection of surface-enhanced Raman scattering from graphene," *Nanoscale*, DOI:10.1039/C8NR02174K, **2018**.

- X. Shi*, N. Coca-López*, J. Janick, and A. Hartschuh, "Advances in Tip-Enhanced Near-Field Raman Microscopy Using Nanoantennas," *Chemical Reviews*, vol. 117, no. 7., pp. 4945–4960, **2017**. * Equally contributed.

- A. Comin, R. Ciesielski, N. Coca-López, and A. Hartschuh, "Phase retrieval of ultrashort laser pulses using a MIIPS algorithm," *Optics Express*, vol. 24, no. 3, p. 2505, **2016**.

- H. Budde, N. Coca-López, X. Shi, R. Ciesielski, A. Lombardo, D. Yoon, A. C. Ferrari, and A. Hartschuh, "Raman Radiation Patterns of Graphene," *ACS Nano*, vol. 10, no. 2, pp. 1756–1763, **2015**.

- G. Bracher, K. Schraml, M. Blauth, J. Wierzbowski, N. Coca-López, M. Bichler, K. Müller, J. J. Finley, and M. Kaniber, "Imaging surface plasmon polaritons using proximal self-assembled InGaAs quantum dots ," *Journal of Applied Physics*, vol. 116, no. 3, p. 033101, **2014**.

List of Conference Contributions

- 2nd Munich 2D Materials (M2M) meeting.
  Munich (Germany), April 9, 2018.
  Oral Presentation: *"Nanoscale optical spectroscopy of 2D materials"*.

- International Conference on Enhanced Spectroscopies (ICES).
  Munich (Germany), September 4 – 7, 2017.
  Poster Presentation: *"Remote Excitation and Detection of Surface-Enhanced Raman Scattering from Graphene"*.

- 7th Early Stage Researchers Workshop (ESRW).
  IMDEA Nanoscience, Madrid (Spain), June 21 – 22, 2017.
  Oral Presentation: *"Remote Excitation and Detection of Surface-Enhanced Raman Scattering from Graphene"*.

- 3rd Doubs Workshop.
  Goumois (Switzerland), May 30 – June 1, 2017.
  Oral Presentation: *"Remote excitation/detection of surface-enhanced Raman scattering from graphene"*.

- Deutsche Physikalische Gesellschaft (DPG) Frühjahrstagung 2017.
  Dresden (Germany), March 19 – 24, 2017.
  Oral Presentation: *"Remote excitation and detection of surface-enhanced Raman scattering from graphene"*.

- Workshop on nanomaterials optics (WNMO) 2016.
  Niederstetten (Germany), October 4 - 6, 2016.
  Oral Presentation: *"Antenna-enahnced microscopy of graphene"*.
  Poster Presentation: *"Tip-enhanced scanning photocurrent microscopy on Graphene"*.

- Nanoinitiative Munich (NIM) Winterschool 2016.
  Kirchberg (Austria), March 13 – 18, 2016.
  Poster Presentation: *"Radiation patterns of semiconductor nanocrystals coupled to optical dimer antennas"*.

- Deutsche Physikalische Gesellschaft (DPG) Frühjahrstagung 2016.
  Regensburg (Germany), March 6 – 11, 2016.

Poster Presentation: *"Radiation patterns of semiconductor nanocrystals coupled to optical dimer atennas"*.

- A NATO advanced study institute on Nano-Optics. International school of atomic and molecular spectroscopy.
  Erice (Italy), July 4 – 19, 2015.
  Poster Presentation: *"New Directions in Tip-Enhanced Near-Field Optical Microscopy"*.

- Deutsche Physikalische Gesellschaft (DPG) Frühjahrstagung 2015.
  Berlin (Germany), March 15 - 20, 2015.
  Poster Presentation: *"Tip-enhanced scanning photocurrent microscopy on Graphene"*.

- Center for Nanoscience (CeNS) Workshop 2014.
  Venice (Italy), September 22–26, 2014.
  Poster Presentation: *"Fourier Space Imaging of Raman Scattering Intensities in Graphene"*.

Acknowledgments

The work resulting in this PhD thesis lasted for almost four and a half years. During this time, many people got involved in my work, in a direct, and an indirect way. To all of them, I would like to express my deepest and most sincere gratitude, for both scientific and personal support. In particular, I would like to mention some of them.

First of all, I would like to thank Prof. Achim Hartschuh for giving me the opportunity to work in his group, for being so encouraging and supportive, and for, literally, always keeping his door open for discussion.

I would like to thank Prof. Tim Liedl for being my second reviewer, and Prof. Sebastian Günther for the discussions about the remote SERS project.

My warm thanks to Rita Römling for being always so helpful and taking care of all of us.

I should mention all former and current members of the Hartschuh group for their help and support. I really appreciate the knowledge they shared, the fun we had, and specially, the friendly atmosphere. Many thanks to Alberto Comin, Richard Ciesielski, Harald Budde, Tobia Mancabelli, Xian Shi, Julia Janik, Irene Grill, Veit Giegold, Kathrin Handloser, Alex Biewald, Frank Schäfer, Lucas Lange, Nicolai Hartmann, and Nina Mauser. Many thanks also to all the bachelor and master students who put so much effort and enthusiasm in the lab, in special: Patricia, Sonja, Qaiser, Nina, Annick, Thomas and Marvin.

Experiments are not possible without a sample. I was so lucky to obtain many good samples from different groups. Therefore, I would like to thank Jürgen Kraus, Paul Leidinger and Prof. Sebastian Günther from the Technical University Munich, Eva Maria Roller, Francesca Nicoli and Mauricio Pilo Pais from the physics department of the LMU, Giovanni Piredda from the Vorarlberg University of Applied Sciences, Ugo Sassi, Antonio Lombardo and Prof. Andrea C. Ferrari from the Cambridge Graphene Centre, and Mäx Blauth and Michael Kaniber from the Walter Schottky Institute. I am also very thankful to Philipp Altpeter for his patience and help in the clean room, Steffen Schmidt for helping with the SEM, and Claudia Paulus for fabricating an optical litography mask.

I am very grateful to Susanne Hennig, Ines Truebenbach and Isabella Krämer for my time as CeNS student representative.

I am very much indebted to my family and friends: the ones in Madrid who always welcomed me back and were the reason for which I always look forward to visit home. The ones here in Munich, whose friendship and support saw me through this work. And the ones who went abroad but always found the time for me, no matter how far they had gone.